November 2017

Dissecting Molecular Pathways that ensure Proper Chromosome Segregation and Cell Division

Anna Ye

DISSECTING MOLECULAR PATHWAYS THAT ENSURE PROPER CHROMOSOME SEGREGATION AND CELL DIVISION

A Dissertation Presented

By

ANNA A. YE

Submitted to the Graduate School of
University of Massachusetts Amherst in partial fulfillment of the
requirements for the degree of

DOCTOR OF PHILOSOPHY

September 2017

Molecular and Cellular Biology

DISSECTING MOLECULAR PATHWAYS THAT ENSURE PROPER CHROMOSOME SEGREGATION AND CELL DIVISION

A Dissertation Presented

By

ANNA A. YE

Approved as to style and contents by:

_____
Thomas J. Maresca, Chair

_____
Peter Chien, member

_____
Jennifer L. Ross, member

_____
Patricia Wadsworth, member

_____
Dominique R. Alfandari, Director
Molecular and Cellular Biology Program

DEDICATION

To my family and friends.

ACKNOWLEDGEMENTS

I would like to thank my advisor Dr. Thomas Maresca first for giving me the great opportunity to work in his lab and complete my PhD. I am very grateful for all his guidance through the last five years, especially during the hard times of failed experiments. Tom's contagious excitement and enthusiasm further encouraged me to always achieve higher, and bring my research to the next level. I feel very lucky to have learned from the best. I will forever take everything I learned and further elevate science.

I would like to thank my family, especially my parents for their continued support. From undergraduate to graduate school, my family has not ceased to encourage me to always pursue my passion. Although they lack English knowledge to understand my research, they are often trying to sort through my kindergarten-level Chinese explanation of my work. I would have never made this far without their encouragement and support.

I especially want to thank Evan Nguyen for his encouragement. He has definitely talked me through many difficult times in graduate school. His love and support is one of the biggest reasons I am still in this. I also owe it a lot to Evan for always pushing me to always do the best work possible, always being supportive of all my decisions. Thank you so much for embarking in this crazy journey with me.

Lastly, I don't think I would have ever done this without the input of my awesome committee. First and foremost, I would like to thank Dr. Patricia Wadsworth for always answering my unexpected drop-in questions and sharing

reagents. I am grateful for Dr. Jennifer Ross's helpful input and suggestions throughout my research, especially in my single molecule TIRF experiments. And last, but not least, I want to Thank Dr. Peter Chien for being such a good sport. I know that my committee meetings are filled with many in-depth details that may sound like jumbles more often than not. Thank you Peter for always having helpful biochemistry suggestions.

Last, but not the least, I want to thank all the new friends I made during my time in Amherst. Payal and Eugene, thanks for keeping me sane! I would have not made through graduate school without having this amazing family away from home.

ABSTRACT

DISSECTING MOLECULAR PATHWAYS THAT ENSURE PROPER CHROMOSOME SEGREGATION AND CELL DIVISION

SEPTEMBER 2017

ANNA A. YE, B.S., UNIVERSITY OF CALIFORNIA DAVIS

Ph.D., UNIVERSITY OF MASSACHUSETTS AMHERST

Directed By: Professor Thomas J. Maresca

Equal segregation of the genome is a prerequisite for cell survival. During cell division the duplicated DNA is compacted into chromosomes and a multi-protein macrostructure, known as the kinetochore (Kt), is assembled on each copy of compacted DNA. Simultaneously, the mitotic spindle, which is made up of microtubules (MTs), is built to facilitate the equal distribution of the chromosomes between the resulting daughter cells. Kinetochores mediate the interaction between the MTs and the chromosomes, properly positioning them for segregation. To ensure that the DNA is equally divided in every cell division, cells have built a surveillance system to detect any errors that may occur. An important checkpoint during mitosis is the spindle assembly checkpoint (SAC), which ensures that all chromosomes are forming the appropriate attachments with MTs.

In cases of erroneous attachment, mitotic progression is halted and an error correction pathway is activated to give chromosomes a second change to establish proper attachment. When all the chromosomes have achieved biorientation, cells progress into anaphase, where each copy of the DNA is pulled

toward opposite axis of the cell. It is critical that chromosome are properly attached and aligned to ensure equal segregation, as misegragation is the leading cause of cell death or cancer. Finally, a cleavage furrow is formed at the cell equator that constricts and severs the cell, giving rise to two daughters.

It is remarkable how cells are able to go through many rounds of division without any errors. Although a lot of work has been done to further understand the mechanisms in which cells detect and correct potential catastrophic error, many more mystery remains to be uncovered. In the last six years, I tried to make my contribution to field by exploring how a previously classified as a non-motile kinesin generates force to move chromosomes, how much force is being exerted on a bioriented kinetochore, the roles aurora kinases play to ensure proper kinetochore-microtubule attachment and proper cytokinesis.

TABLE OF CONTENTS

Page

LIST OF TABLES

Table Page

LIST OF FIGURES

Figure Page

CHAPTER 1

INTRODUCTION

1.1 Cell Division

Shortly after the genomic material is duplicated, cells enter mitosis. Although very short in duration relative to the other stages of cell cycle, mitosis is highly regulated to ensure that the duplicated DNA is equally segregated among the two daughter cells to optimize cell survival. Each copy of the duplicated DNA is compacted into sausage-like structures to facilitate segregation. The two identical copies of the DNA, also known as sister chromatids, are held together to form the chromosome. A macromolecular structure made up of hundreds of proteins, also known as the kinetochore (Kt), is assembled at the centromeric region of each of the sister chromatids. Additionally, the microtubule (MT) cytoskeleton is rearranged in the mitotic spindle, which mediates the positioning and segregation of the chromosomes.

As cells get ready to divide, the duplicated DNA starts to condense and the nuclear envelope breaks down in a stage called prometaphase. The chromosomes align at the cell equator during metaphase, and further get pulled towards each pole during anaphase. Finally a cleavage furrow forms at the cell equator during telophase, followed by scission to give rise to two identical daughter cells (Fig 1.1). Although it may sound like a simple process, but to achieve perfection at every division is a hefty accomplishment. Thus all components need to be finely tuned and coordinated at every step of cell division.

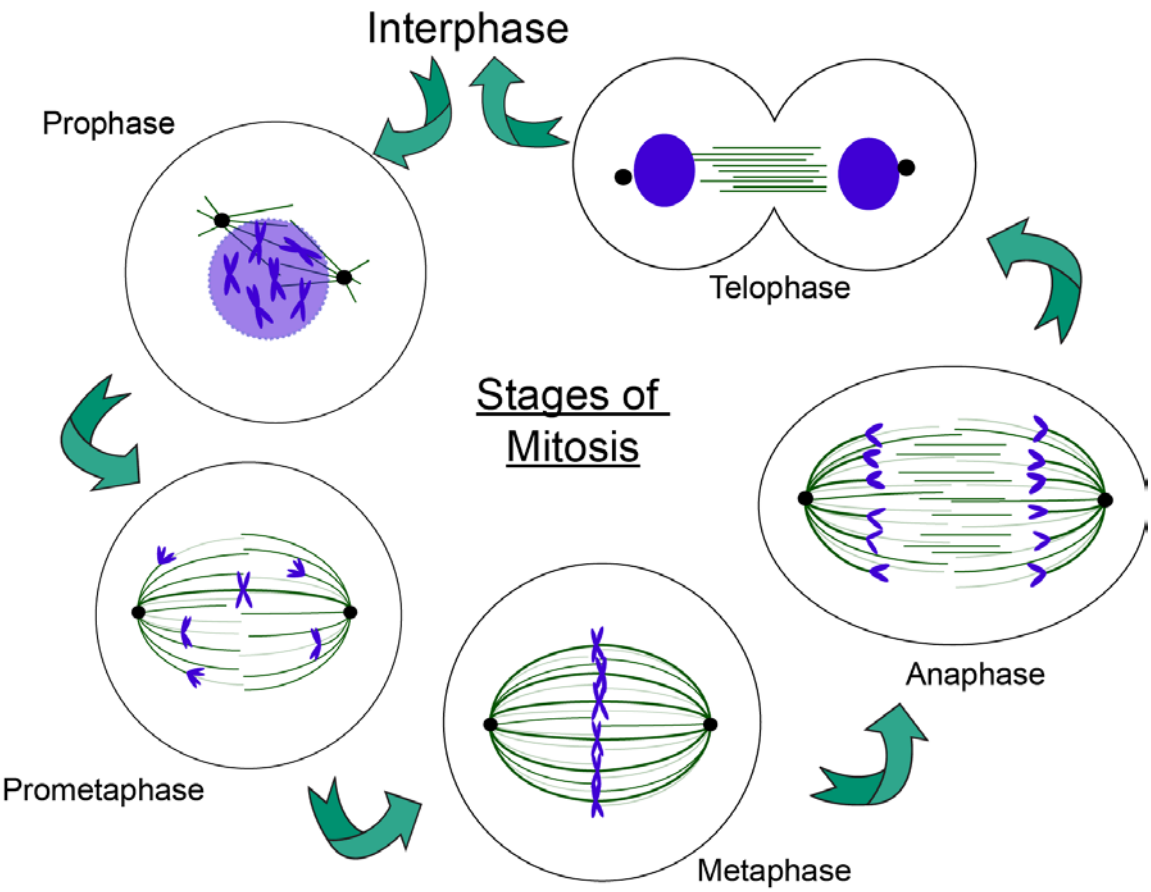

Figure 1.1. Stages of cell division.
An illustration of the difference stages of the mitosis, highlighting the organization of the MTs and chromosomes. The centrosomes and DNA is duplicated during interphase. The first stage of mitosis is prophase, when the duplicated DNA condenses into chromosomes, the nuclear envelops breaks down, and the mitotic spindle starts to form. The bipole spindle is fully established during prometaphase, and kinetochores start to attach to MT, and they fully align at the cell equator at metaphase. When all chromosomes are bioriented, the sister chromatids gets pulled toward opposite poles of the cell during anaphase. Finally, a nuclear envelope forms around the chromosomes during telophase and a cleavage furrow forms at the cell equator for cytokinesis.

1.2 The Mitotic Spindle

As cells enter mitosis, a football-like structure is formed, known as the mitotic spindle to provide a structure to organize and segregate the genetic material. The main components of the spindle are microtubules, which are hollow tubes built from α- and β-tubulin subunits that interact in a head-to-trail manner, thus giving this filament an orientation. MTs have a defined directionality, known as minus- and plus-ends, determined by α- and β- tubulin termini, respectively, that have different dynamic and physical properties. A filament can switch from growing to shrinking and vice-versa, events known as catastrophy and rescue, respectively, a phenomenon described as dynamic instability (Fig 1.2). MT polymerization is the process of adding GTP bound tubulin subunits to a filament, giving MTs a distinct GTP cap. MT shrinkage happens when the addition of tubulin is slower than the rate of tubulin GTPase activity, which results in disappearance of the GTP cap. The dynamicity of the MTs is critical for organization and function of the mitotic spindle.

The mitotic spindle is made up of three categories of MTs: (1) the spindle MTs, (2) the bundle of MTs that interacts with the kts, also known as K-fibers, and (3) astral MTs that grow towards the cell cortex, where it interacts with cortical proteins for spindle positioning. The mitotic spindle has a pair of centrosomes residing at the spindle poles, which contain components of the γ-tubulin ring complex (γ-TURC) (Conduit et al., 2015), where MT nucleation events take place. Additionally, chromosomes are also able to mediate MT nucleation through a RanGTP gradient dependent pathway (Kalab et al., 2006; Kalab et al.,

2002). Given the complexity of the mitotic spindle, how do chromosomes manage to form correct attachments with the microtubules? Rather than directly binding to the DNA, MTs binds to a protein structure assembled only during mitosis, the kinetochore. Kinetochore-microtubule (kt-MT) attachment can be achieved through ‘search-and-capture’ (Wollman et al., 2005), where MTs nucleating from the centrosomes are constantly growing and shrinking searching for a kinetochore to form attachments. Alternatively, MTs nucleated through the chromatin-mediated pathway is incorporated into the spindle.

Once the kt-MT attachment is established, the mitotic spindle is also necessary for segregation of the chromosomes. During anaphase, the spindle elongates while the k-fibers shortens, resulting in movement of the sister chromatids to opposite spindle poles. Although the microtubules intrinsically dynamic polymers, the organization and assembly of the mitotic spindle requires the correct localization, amount, and function of many microtubule associated proteins (MAPs) and motor proteins.

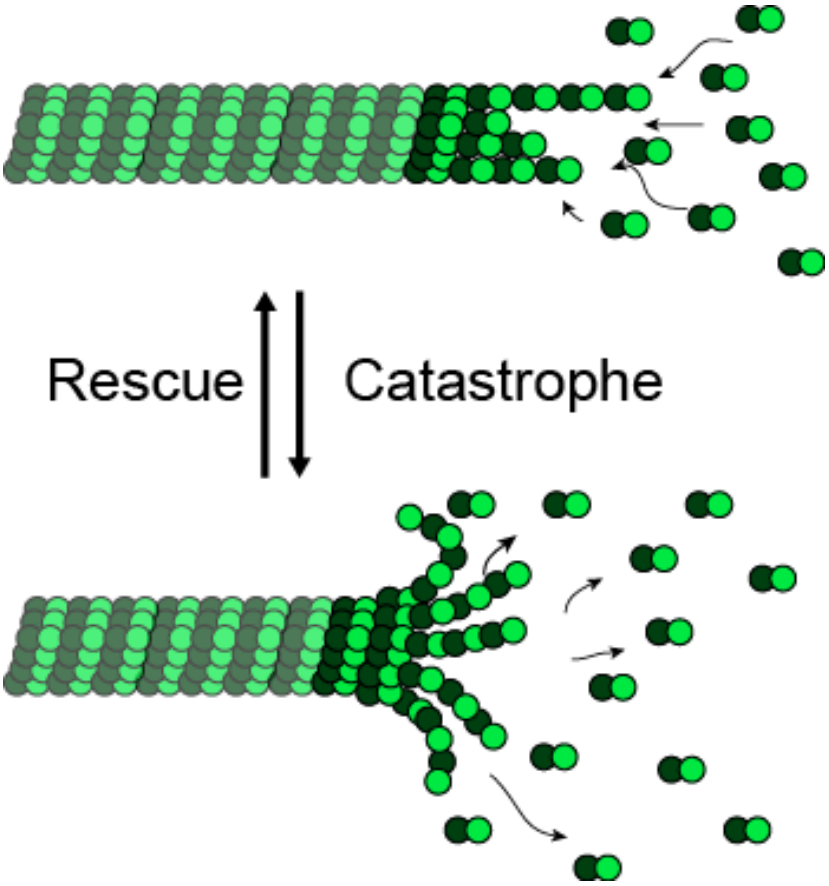

Figure 1.2 Microtubule dynamic instability.
Microtubules are dynamic tubules that are constant growing and shrinking, a phenomenon known as dynamic instability. The intrinsic properties of MTs allow cells to rearrange the cytoskeleton during mitosis to make the mitotic apparatus to aid with the segregation of the genetic material.

1.3 Kinetochore-Microtubule Attachment

Instead of directly binding to the chromatin, spindle microtubules interact with a macromolecular protein structure that is assembled at the centromeres of the chromosomes, also known as the kinetochore (kt). To achieve proper chromosome segregation, where each copy of the DNA is divided among the two daughter cells, kinetochores-microtubule attachments need to be in the bioriented configuration (Fig 1.3), when each sister kt are attached to MTs emanating from opposite spindle poles. However, biorientation is not the default nature of this interaction. Other attachment configurations, such as syntelic, both kts are attached to the same pole, and merotelic, one kt is attached to both spindle poles, are often found in cells and corrected. Syntelic and merotylic attachments are destabilized by phosphorylation of kinetochore proteins that mediates interactions with MTs, through a process known as error correction, to give rise to unattached or monotelic kt, where only one kt is attached to MTs from one pole. When syntelic attachments are left incorrected, both sister chromatids are pulled to the same daughter cell, leading to aneuploidy. Merotelic attachments lead to lagging chromosomes during anaphase, a delay in segregation of that chromosome because one kt is going through tug-o-war, which can result in formation of micronuclei.

How are cells able to accurately detect the attachment state of each and every kinetochore at every cell division? In cases of erroneous attachments, cells generate a wait-anaphase signal, also known as the spindle assembly checkpoint (SAC), which delays cell progression until all kts are properly

attached and aligned at the metaphase plate. This signal allows for error correction to take place. Although a lot of work has been done to understand how the SAC is assemble and satisfied, the exact signal being detects by the molecules remains an unknown. Upon biorientation, the opposing mechanical force exerted on each of the sister kinetochore from the dynamic MTs causes a structural change to kinetochore proteins. Proper attachment results in kinetochore proteins being placed farther away from a centromere based kinase gradient, further reinforcing the kt-MT attachment.

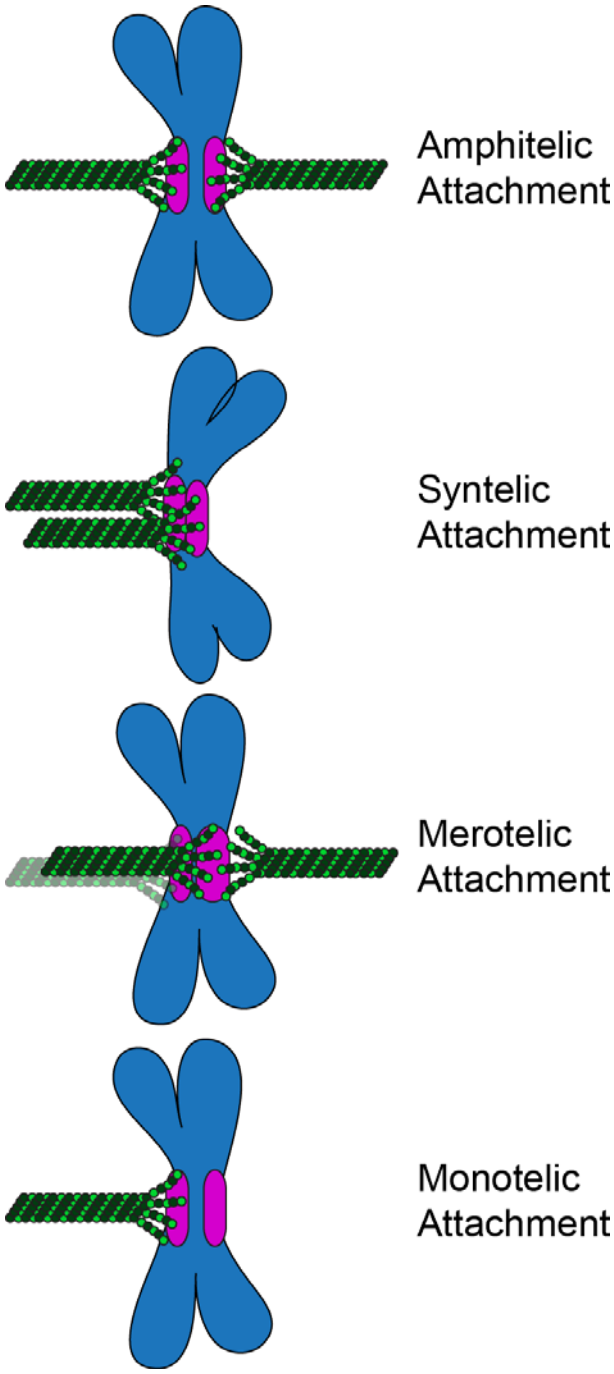

Figure 1.3. Kinetochore-Microtubule attachment states.
Microtubules can interact with kts in many different configurations with amphitelic attachment, where each sister kinetochore is attached to MTs emanating from opposite spindle poles, as the final goal. Erroneous attachments, such as syntelic and merotelic attachments, both kts are attached to the same pole and a single kt is attached to both poles, respectively, can lead to chromosome misegregation. Erroneous attachments are often destabilized to form unattached or monotelic attachment, when only one kt is attached to MT, to reestablished proper kt-MT attachment.

1.3.1 The kinetochore

The kinetochore is a macro-structure that is assembled onto the centromeric region of each sister chromatid in an ordered manner. A specialized population of modified histone H3, also known as CENP-A, determines the location of the centromere and also serves as a platform for Kt assembly. CENP-C, a constitutive Kt associated protein, interacts with CENP-A via the C-terminal centromere targeting region. In *Drosophila,* CENP-C is the sole molecule connecting the chromosome to the outer kinetochore, the main components responsible for interaction with MTs. The outer plate of the Kt is mainly composed of the Mis12 complex, KLN1, and NDC80 complex, together forming the KMN network (Fig 1.4).

CENP-C is a large, mostly unstructured protein, with structured C- and N-termini domains that interacts with CENP-A and Mis12, respectively, that is constituently localized at centromeres throughout all cell cycles. The unstructured, flexible middle section allows CENP-C to stretch in response to force similar to a rubber band. Centroid mapping of two color imaging of CENP-C where the N- and C-termini are tagged with different colored fluorophore has revealed that CENP-C stretches from upon kinetochore biorientation, extending a length of 25nm (Stu's dissertation). In contrary of CENP-C, the Mis12 complex has been shown to have a long and rigid structure, spanning about 20nm in length. Mis12 acts as the main binding hub of the KNL1 and NDC80 complexes to the inner kinetochore. Mis12 assembly at the kinetochore is enriched during mitosis, a step that is believed to be regulated by aurora B kinase (Petrovic et al.). KNL1

complex is the largest kinetochore protein that is believed to be a platform for the spindle assembly checkpoint signaling. Finally, the NDC80 complex is believed to be the main MT binding protein and mediate force bearing attachments. The complex is a long coiled-coil protein with two globular regions at either ends, extending approximately 55nm. NDC80-MT interaction is phospho-regulated by centromeric aurora B and polar aurora A gradients. The kinetochore is organized in such a way that when proper attachment is achieved, outer kinetochore proteins are positioned away from kinase gradients to reinforce kinetochore-microtubule attachments.

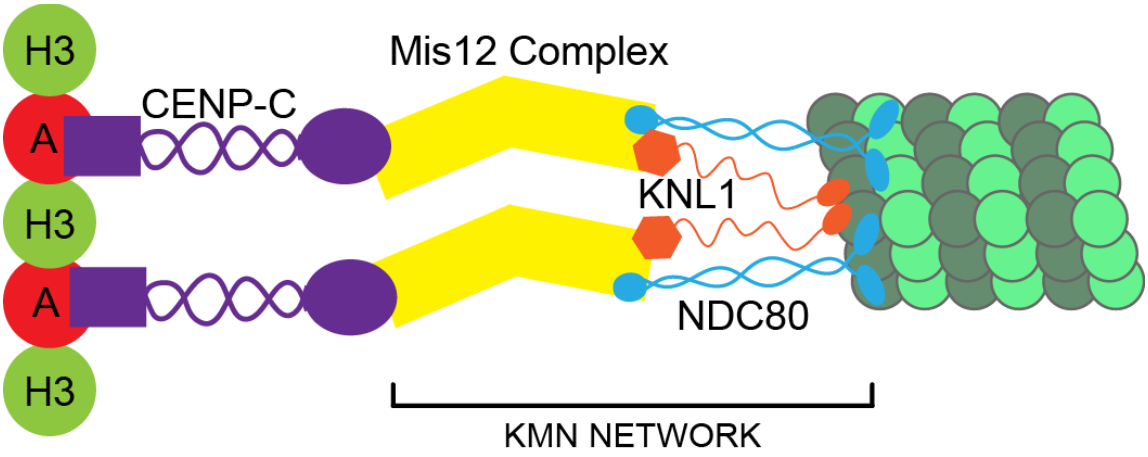

Figure 1.4. Arrangement of the kinetochore proteins.
Illustration of a simplified *Drosophila* kinetochore. CENP-A is a specialized, modified histone H3 that defines the centromere of the chromosome. CENP-A recruits CENP-C, which is a large, mostly unstructured protein that recruits the Mis12 complex through its C-terminus. Mis12 further recruits the other members of the KMN network, NDC80, which is the main MT binding protein, and KNL1, which is the platform for the spindle assembly checkpoint.

1.3.2 Aurora Kinase Gradients

The Auroras are serine/threonine kinases with important roles essential for cell proliferation. *Drosophila melanogaster* have two highly conserved Aurora kinases: Aurora A (AAK) and Aurora B (ABK). *Drosophila* AAK and ABK have conserved C-terminal catalytic domain that have similar phosphorylation consensus sites and share many of the same substrates (Kettenbach et al., 2011). However, it is known that AAK and ABK have very different cellular functions. Their distinct localizations and roles during mitosis are defined by their divergent N-terminal domain that determines their interacting proteins (Hochegger et al., 2013). Aurora A is enriched on the spindle poles/centrosomes, and required for mitotic entry and centrosomes duplication and maturation (Fig 1.6). Aurora B, a member of chromosome passenger complex (CPC), is required for spindle assembly, chromosomes biorientation, and cytokinesis.

Aurora B kinase, a well-studied kinase, is a member of the CPC, forming the complex with Borialin, Survivin, and INCENP. Their localization in the centromere during early cell division is crucial for error correction (Fig 1.6). The roles of ABK in error correction and phosphorylation of NDC80 to destabilize kt-MT attachment is very well understood (Akiyoshi et al., 2009; Alushin et al., 2012; Caldas et al., 2013; Chan et al., 2012; DeLuca et al., 2011; Kalantzaki et al., 2015; Sarangapani et al., 2013; Welburn et al., 2010). On the other hand, Aurora A kinase is highly enriched at the centrosomes. A major phenotype of AAK deficient cells is the increase frequency of monopolar spindles, thus leading to the notion that it is required for centrosome replication and function. Another

obvious phenotype seen in vertebrae cells lacking AAK is the presence of misaligned chromosomes, leading to misegregation and aneuploidy. These defected have been mostly attributed to immature centrosomes and the inability to properly polymerize and stabilize microtubules. On the contrary, the misalignment defects may be due to compromised error correction because AAK have the highly conserved C-terminal kinase domain. However, the role of AAK in error correction is not well established.

After chromosome segregation, bundled antiparallel microtubules assemble between the segregated chromosomes, forming the spindle midzone, to create a binding platform for proteins required for proper cytokinesis. ABK relocalizes to the spindle midzone during anaphase, where it has critical functions to ensure proper furrow formation and cytokinesis, and delay of plasma membrane scission in cases of lagging chromosomes. The exact activity of ABK in late mitosis has been hard to assess because cells lacking ABK have catastrophic consequences: cells exit mitosis and nuclear envelope is formed around all the chromosomes. It has also been reported that AAK is required for proper midzone formation (Giet et al., 2002; Reboutier et al., 2013), through regulation of microtubule stabilizing components.

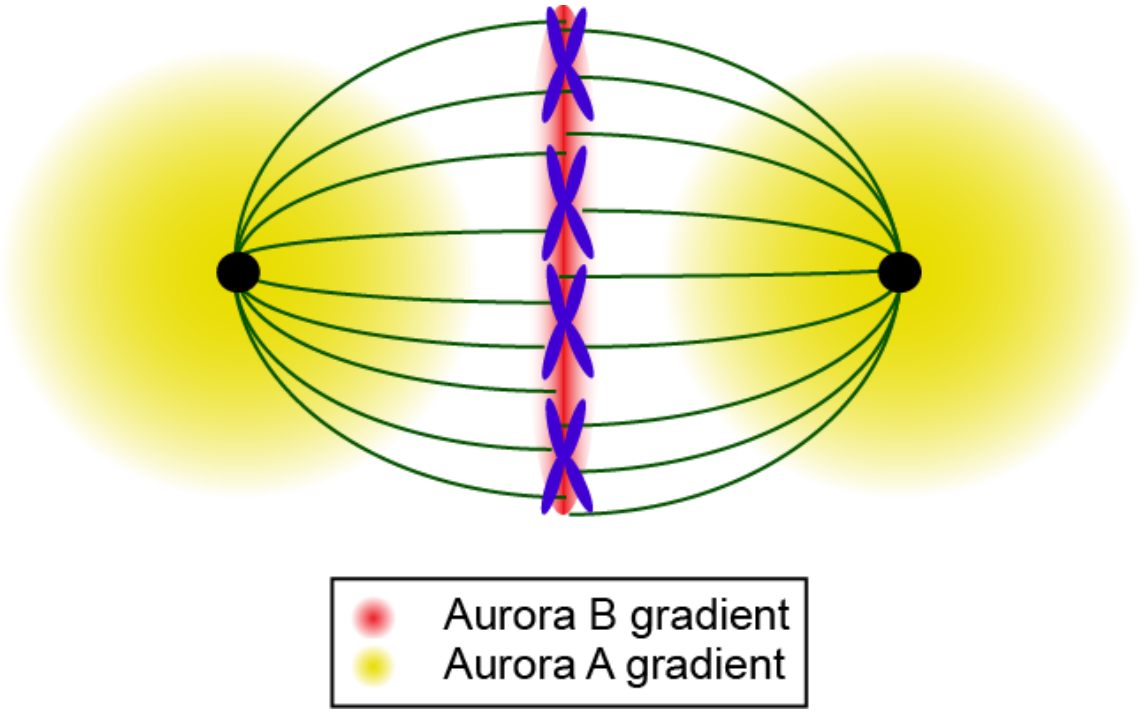

Figure 1.5. Aurora Kinase gradients during mitosis.
Aurora A (AAK) and Aurora B (ABK) kinases are highly conserved, with a divergent N-terminal domain that determines their localization. AAK is enriched at the spindle poles, where it is required for centrosome duplication and separation. ABK is localized at the centromeres, in the CPC, where it is required for error correction and phosphorylation of kinetochore proteins. Due to the similarity in the phosphorylation consensus site, AAK and ABK has many of the same substrate, thus it is postulated that AAK is also involved in error correction near the spindle poles.

1.4 Microtubule Based Motor Proteins

Organelles and cellular materials have to be properly placed in the cell to be able to perform their functions. Motor proteins are the main transportation agents to move cellular components on microtubule tracks. Motors bind to MTs through their “head” motor domain, which walks along MTs through a conformation change that uses energy derived from ATP hydrolysis, and binds to cargos through the “tail” domain. There are two types of microtubule based motors: kinesins and dynein. The first kinesin was first discovered in giant squid neurons transporting small membrane bound organelles in a unidirectional manner (Vale and Goldstein). It soon became obvious that kinesins are highly conserved among most organisms and many additional kinesin-like proteins were discovered. The functional diversity of the different kinesins is determined by the divergent region between the motor head and the cargo binding tail domains, in addition to other post-translational modifications (reviewed in (Welburn, 2013). To the contrary to the multiple families of kinesins, there is only one cytoplasmic dynein, which is responsible for the majority of the minus-end directed transport of cellular materials. Unlike kinesins, dynein is often found within a large 1.4 mDa complex with dynactin, the main regulator of dynein function, and different cargo adaptor proteins that determine the diversity in vesicle transport (reviewed in (Liu, 2017)) .

The microtubule cytoskeleton goes through a major rearrangement during cell division to form the mitotic spindle. Although it is thought to be a self-organizing macromolecular structure, the dynamics and polarity of MTs is not sufficient to

assemble a spindle; but rather motors proteins play crucial roles in regulating the size, positioning, and the organization of the mitotic apparatus. Additionally, motor proteins are responsible for regulating MT bundling and dynamics, and chromosome movements within the spindle. Altogether, motor proteins come together with microtubules to create a robust mitotic apparatus to ensure proper chromosome segregation at every cell division.

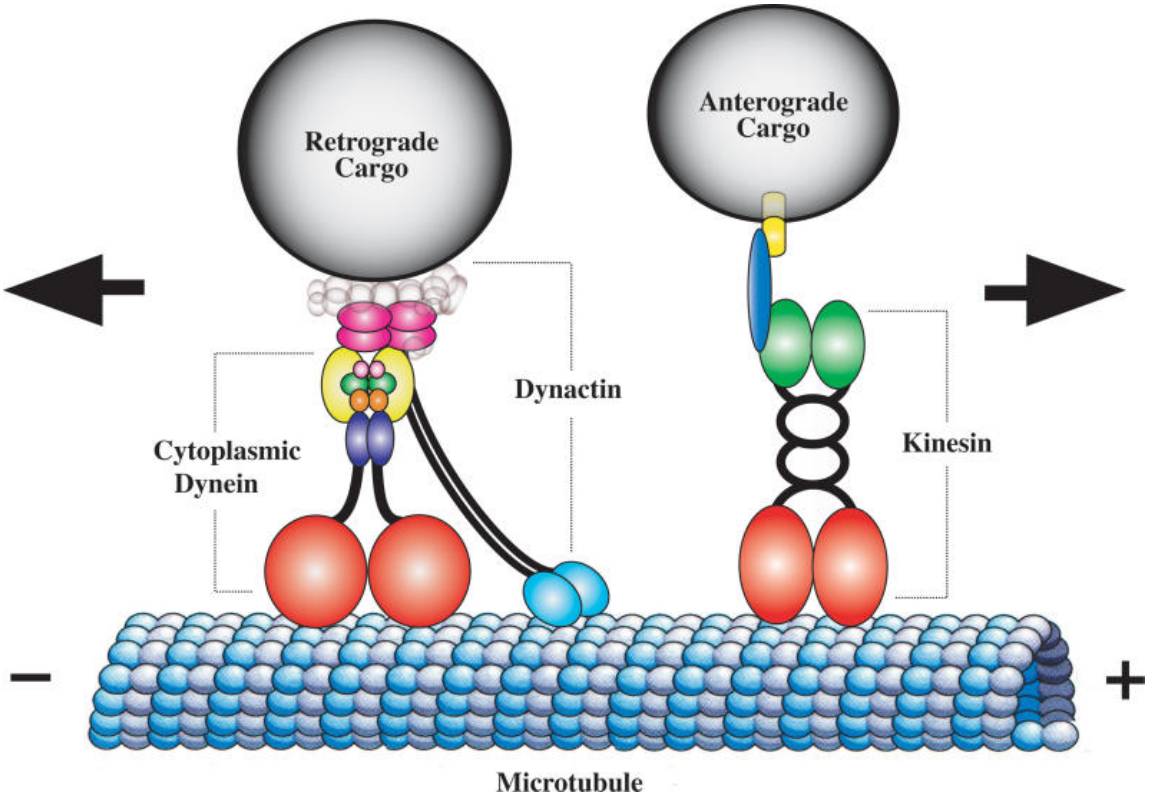

Figure 1.6. Microtubule based motor proteins.
Microtubule based motors used the energy from ATP hydrolysis to move along MTs, carrying along cargos. The two main types of motors are kinesins and dynein. The first discovered kinesin was a plus-end directed motor, but later discovery found a family of minus-end directed kinesins. In contrary to kinesins, dynein is mostly a minus-end directed motor, always found in a large complex with motor regulatory and cargo adaptor proteins.
This image was adapted from (Duncan and Goldstein, 2006).

1.4.1 Tip-tracking Motors

Many motors and microtubule associated proteins (MAPs) bind to the entire length of the MT except for groups of special proteins known as the End-binding (EB) (Schuyler and Pellman, 2001) and proteins containing the cytoskeleton-associated protein glycine rich (CAP-Gly) domain (Steinmetz and Akhmanova, 2008) that only interacts with the ends of polymerizing MTs. The ability to bind solely to the growing tip of MTs is known as tip-tracking. EB family of proteins are able to recognize and bind to the interface between the β- and α-tubulin of two dimers in a nucleotide specific state, thus it only interacts with the GTP cap of a growing MT (Maurer et al., 2012). On the other hand, CAP-Gly domains are highly acidic, which interacts with the basic C-terminal tail of α-tubulin, also termed the E-hook. Microtubules can go through detyrosination, in which the tyrosine residue on the E-hook is severed on stable MTs. Interestingly, CAP-Gly domains bind to detyrosinated E-hooks at a much less affinity (Wang et al., 2014). Therefore, the mechanism in which CAP-Gly domains tip-track is defined by the intrinsic properties of the MT itself, where the tubulin dimers added to the MT are tyrosinated.

All motor proteins use MTs as tracks to walk, but a handful of them also bind to MT plus-end, either directly or by hitchhiking with a tip-tracker. For instance, CENP-E is a kinetochore associated motor that has plus-end directed motility and directly binds to both polymerizing and depolymering MT-plus ends using a second MT binding domain (Gudimchuk et al., 2013b). Some motors tip-track using the CAP-Gly domain, such as dynein/dynactin and kif13b. In addition to tip-

tracking by direct interaction with MT plus-ends, CAP-Gly domains also binds to the very C-terminus EEY/F sequence motif of EB1. Lastly, motors can also tip-track by catching a ride with EB1. A well-established EB1 interacting domain is the SxIP motif and the surrounding nine amino acids (Jiang et al., 2012a), which binds to the EBH domain in EB1. Recent work done in fungi have revealed a new unconventional EB1 binding PT sequence motif . Similar to the traditional SxIP, the surrounding amino acids play important roles at providing the proper pocket environment to reinforce the interaction (Kumar et al., 2017a).

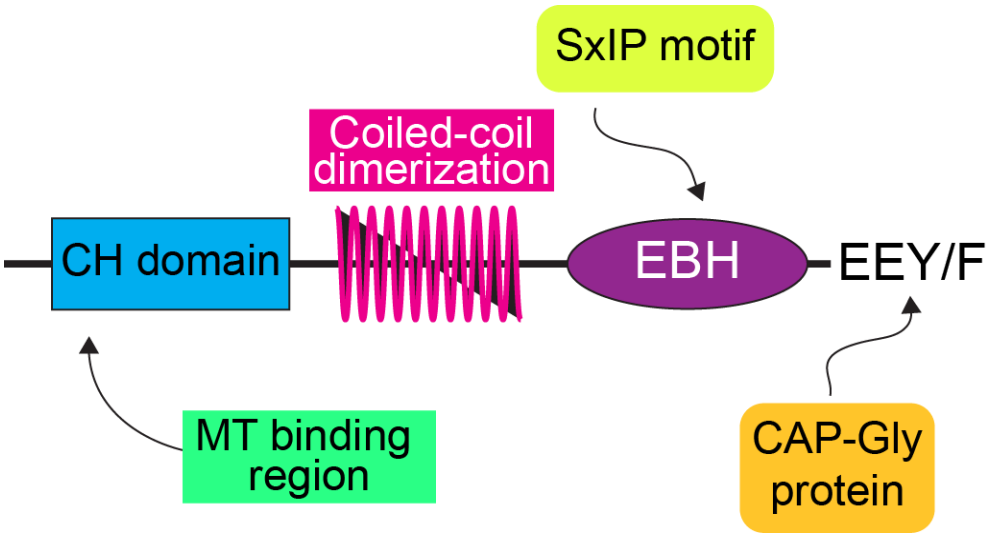

Figure 1.7. Illustration of the different structural domains of EB1.
EB1 is a microtubule associated protein with the size of 32kD that exclusively binds to the plus-ends of polymerizing MTs. It has an N-terminal CH domain that interacts with MTs, a coiled-coil region for dimerization, an EBH domain that mediates interactions with other proteins through their SxIP motif, and a C-terminal EEY/F sequence motif that interacts with CAP-Gly domains.

1.5 Cleavage Furrow

After the chromosomes are segregated to the poles of the cell, an extensive actin-myosin network is formed at the equatorial cortex, also known as the cleavage furrow, to help pinch off the membrane to give rise to two daughter cells, a process known as cytokinesis. The timing and the placing of furrow formation must be coordinated timely following the segregation of the chromosomes and at the halfway point of the spindle, respectively, to ensure the proper cytoplasmic distribution among the two cells. There is no doubt that the mitotic apparatus is absolutely required for proper cleavage furrow formation. It is currently understood that three redundant signals determines the location of the cleavage furrow formation: (1) astral relaxation, (2) astral stimulation, and (3) midzone stimulation (Fig 1.9) (Glotzer, 2004; Mishima, 2016). While the astral relaxation signals inhibits the formation of a cleavage furrow near the spindle poles, the stimulation signals induce the accumulations of proteins required for cytokinesis in the equatorial cortex of the cell.

It has been known that the mitotic spindle, in particular the microtubules, are generating the signals for cleavage furrow positioning. Many groups have shown the relationship between the formation of the actomyosin network and the stability of microtubules (Foe and von Dassow, 2008; Murthy and Wadsworth, 2008; Odell and Foe, 2008). However, the key players required for pinching off the cell membrane are members of the acto-myosin network, leading to the question as to how signals generated from microtubules are translated to actin-myosin function. *Drosophila* Pavarotti, also known as MKLP1 in mammalians, is

a plus end directed kinesin-6 motor that forms the centralspindlin complex with RacGAP50C. RacGAP recruits ECT2, a major activator of RhoA that required for actomyosin network formation and function during cytokinesis.

The role of ABK during cytokinesis has always been hard to discern due to the catastrophic results from inhibiting the kinase. It has been proposed that ABK activity is required for activation of MKLP1 but not localization. Other studies suggest that RacGAP is a ABK substrate, but the idea remains controversial (D'Avino et al., 2005). All the results feed into the idea that ABK is generating a kinase gradient during anaphase that is important to translate a signal that initiates at the microtubules that forms the spindle midzone to the actomyosin network at the cortex. This gradient, which needs to extend from the spindle midzone to the cortex, may be regulating a range of pathways such as stabilizing astral microtubules, activating MLKP1 and regulating RacGAP function. However, we believe that ABK has a very short working distance, in the scale of nanometers. On the contrary, AAK has a much larger working distance, in the scale of micrometers. We hypothesize that AAK is functioning during cytokinesis by generating an aurora kinase gradient at the equator of the cell to ensure timely furrow formation.

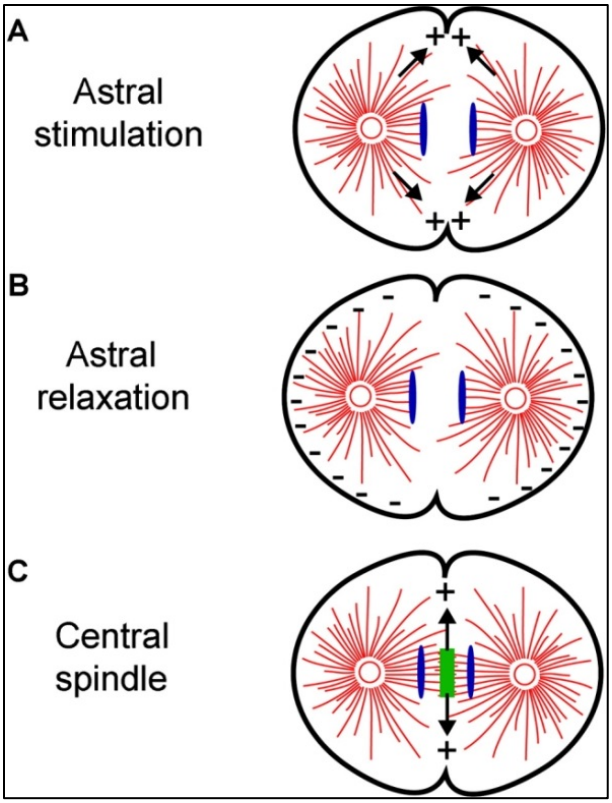

Figure 1.8. Models for establishing the location of the cleavage furrow.
The positioning of the cleavage furrow is believed to be influenced by three redundantly pathways. The central spindle and astral stimulation sends a signal to the cortex to promote cortical contraction, while the astral relaxation signals the polar cortex to reduce cortical contractility.
Figure adapted from (Glotzer, 2004)

1.6 Broad Relevance

Cell division is a very important aspect of cell cycle as it is required for development and tissue growth. However, it is critical that every cell division happens perfectly to have the best chances of cell survival. Errors in chromosome segregation early in can have catastrophic effects. Misegregation of individual chromosomes leads to aneuploidy, where cells have abnormal numbers of chromosomes, which causes genetic diseases such as trisomy 21, also known as Down syndrome. Timing of cytokinesis is also tightly regulated to ensure that all the chromosome have already been segregated to the equivalent daughter cell. Chromosomes remaining in the cell equator during cytokinesis are often severed or unincorporated from the main nucleus, risking the formation of micronucleus. Micronuclei are more susceptible to DNA damage and often remain unduplicated. Although it is possible for them to be reincorporated into the main nucleus, micronuclei often cause of gain or loss of genetic material of the daughter cells. On another extreme, cells can also fail cytokinesis altogether and the two copies of the genome remains in the same cell, resulting in multiploidy, Abnormal amount of genetic material, either in the forms of aneuploidy or multiploidy, is the leading cause of cancer and malignancy, thus understanding the pathways that ensure proper chromosome segregation and cell division can shed light into understanding the uprising of cancer and possible prevention and/or cures.

CHAPTER 2

CHROMOSOME BIORIENTATION PRODUCES HUNDREDS OF PICONEWTONS AT A METAZOAN KINETOCHORE

This chapter was done in collaboration with Stuart Cane. With the guidance of Prof. Thomas Maresca, I did all the acceptor photobleaching (FRET) experimetns and all the protein knockdown validations. This chapter is published in *Nature Communications* in 2016 (Ye et al., 2016a).

2.1 Introduction

The forces that act on the kinetochore and how they are transduced depend on the nature of kt-MT interactions and the identity and number of force-producers. Early in mitosis, kinetochores predominantly associate with the sides of MTs. The forces produced by kinetochore-associated motors laterally interacting with MTs are transmitted into sliding chromosomes directionally within the spindle. The major kinetochore-associated force producers at this stage are the plus-end directed CENP-E and the minus-end directed dynein each of which are capable of producing forces in the low pN range (~1-8 pNs) (Gennerich et al., 2007; Mallik et al., 2004; Toba et al., 2006; Yardimci et al., 2008). While motor-mediated forces produced during lateral kt-MT interactions facilitate proper chromosome congression (Barisic and Maiato, 2015; Kapoor et al., 2006), they are neither sufficient to satisfy the spindle assembly checkpoint (SAC) nor to support accurate chromosome segregation during mitosis(Cai et al., 2009). Rather, these outcomes require the formation of stable end-on kt-MT attachments that are mediated by a conserved MT-binding complex in the outer kinetochore called the

KMN (KNL1, Mis12 Complex, Ndc80 complex) network(Cheeseman et al., 2006). End-on attached kinetochores must be able to harness the forces produced by MT dynamics to move chromosomes. MT polymerization exerts forces (~3 - 4pN) similar to those produced by kinetochore motors (Dogterom and Yurke, 1997), while depolymerization of a single MT has been estimated to produce forces up to 65 pN (Grishchuk et al., 2005), an order of magnitude higher than individual motors. Poleward pulling forces applied to end-on attached kinetochores contribute to prometaphase congression, metaphase oscillations, and anaphase A movements (Coue et al., 1991; Grishchuk and McIntosh, 2006; Khodjakov and Rieder, 1996; Koshland et al., 1988; Tanaka et al., 2007). When biorientation is established, opposing poleward forces produce tension across sister kinetochores that stabilizes kt-MT attachments and contributes to SAC satisfaction (Akiyoshi et al., 2010; Li and Nicklas, 1995; Nicklas and Koch, 1969). There is a surprising lack of consensus about the magnitude of force that is applied to the kinetochore despite the fact that it is one of the most important force-transducing structures in the cell.

In principle, very low forces are sufficient to move non-bioriented chromosomes if the only opposing force is the viscous drag of the cytoplasm(Nicklas, 1965). Indeed, analyses of anaphase chromosome movements in insect meiotic and mitotic cells yielded force estimates below 1 pN (Marshall et al., 2001; Nicklas, 1965). However, the forces required for poleward moving mono-oriented chromosomes in prometaphase amphibian cells were estimated to be considerably higher than in anaphase and ranged between ~10 -

75 pN (Alexander and Rieder, 1991), which is likely a result of polar ejection forces and steric hindrance from astral MTs opposing prometaphase but not anaphase chromosome movements. Prometaphase poleward movements are mainly driven by lateral sliding along MTs by kinetochore-associated dynein (Yang et al., 2007), but differences in prometaphase (10 - 75 pN) and anaphase (<1 pN) forces cannot be attributed to dynein producing higher forces than the depolymerizing kt-MTs driving anaphase movement. To the contrary, an important study using calibrated microneedles concluded that anaphase k-fibers in insect cells produced up to 700 pN (~50 pN / MT) of poleward directed force (Nicklas, 1983). These direct physical measurements suggest that comparable forces could be applied to metaphase kinetochores since the application of opposing force with a microneedle resembled the bioriented configuration more so than the typical anaphase scenario.

Measuring the magnitude of force applied to bioriented kinetochores has presented a significant challenge. Researchers recently estimated that the mean pericentromeric tension at bioriented yeast kinetochores is 4 - 6 pN / MT (and per kinetochore since the budding yeast kinetochore binds one MT) (Chacon et al., 2014). This value fits reasonably well with in vitro optical trapping studies using purified budding yeast kinetochore proteins and isolated kinetochore particles that have reconstituted associations with single MT plus-ends over forces ranging from ~2 - 9 pN (reviewed in (Yusko and Asbury, 2014)). Although forces above 20 pN have been theoretically inferred (Grishchuk et al., 2008) and directly measured for kinetochore proteins attached to beads via extended linkers

(Volkov et al., 2013). While a general consensus (within an order of magnitude) may be emerging for the forces that are applied to budding yeast kinetochores, experimental measurements in metazoans have diverged dramatically. In contrast to earlier measurements of 700 pN / kinetochore (50 pN / MT) (Nicklas, 1983), a more recent optical trapping study in meiotic insect cells and mitotic mammalian cells measured stall forces of end-on attached kinetochores at ~2 – 10 pN / kinetochore (below 1 pN / MT) (Ferraro-Gideon et al., 2013). Thus, existing estimates of end-on attached kinetochore forces in animals span two orders of magnitude.

In this study we aimed to address the substantial inconsistencies in kinetochore force estimates by inserting calibrated force sensors into the *Drosophila* kinetochore. *Drosophila* S2 cells are an excellent model system to study kinetochore forces because bioriented chromosomes do not oscillate and; therefore, sister kinetochores are generally under equal opposing forces. Furthermore, most other well-studied kinetochores possess multiple linkages between the DNA and the outer kinetochore, but the *Drosophila* kinetochore appears to possess a single linker molecule - CENP-C (Przewloka et al., 2011a). CENP-C, which constitutively localizes to the centromere throughout the cell cycle, associates with centromeric DNA through its C-terminus (Carroll et al., 2010; Milks et al., 2009; Yang et al., 1996) and its N-terminus binds directly to the outer kinetochore (Przewloka et al., 2011b; Screpanti et al., 2011) while the rest of the protein, especially in *Drosophila*, is highly disordered (Fig. 2.1A, B). Therefore, force sensors were engineered into CENP-C (Fig. 2.1A) and the

behavior of reporters inserted into the middle of the unstructured region of the molecule were compared to negative controls in which the sensors were placed at the C-terminus so that they would not be subjected to force (Fig. 2.1C). Stable cell lines expressing each of the force reporters were used in all the experiments and there were no evident dominant negative effects to engineering CENP-C in the manners described.

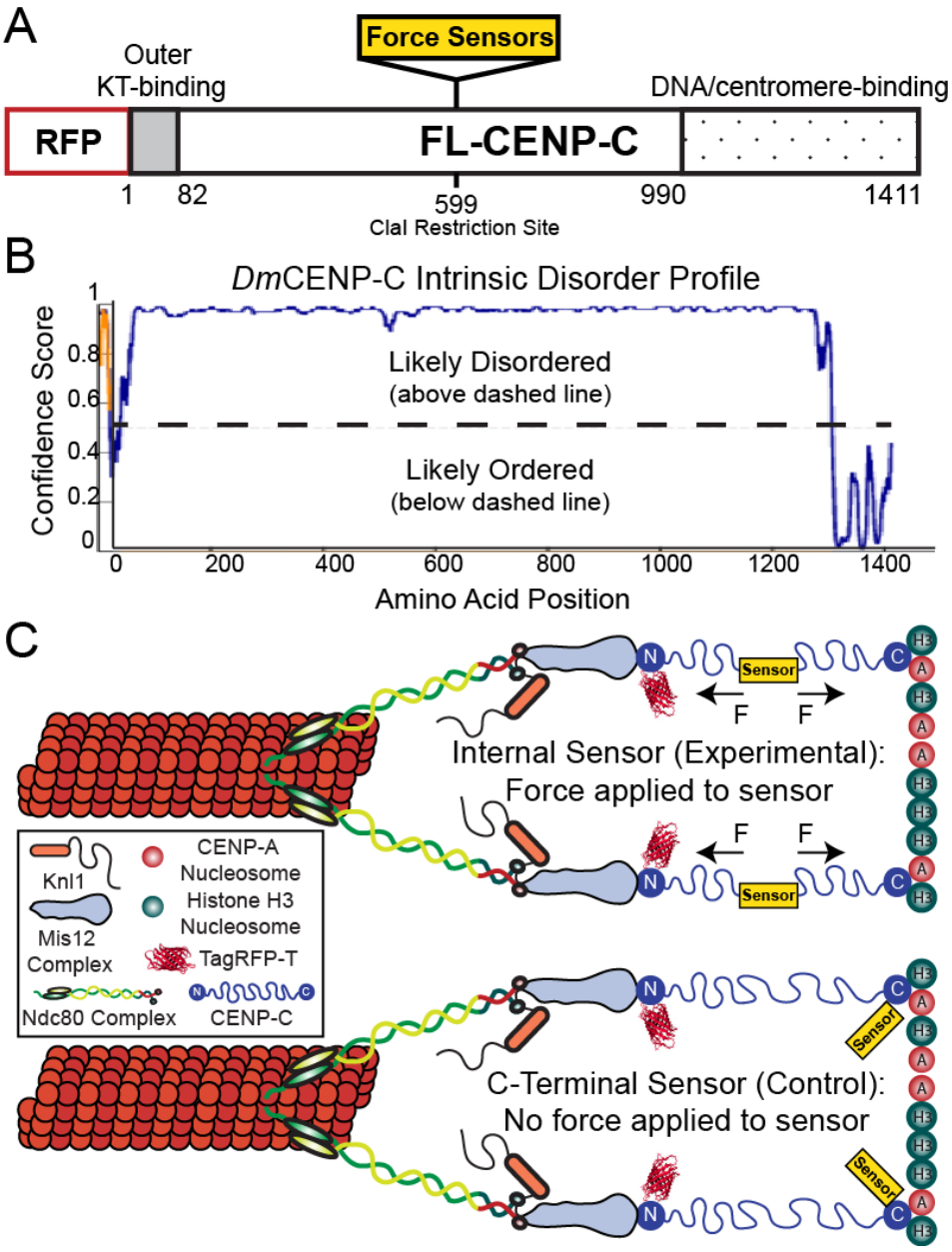

Figure 2.1. Construction of the CENP-C-based force sensors and the experimental design for force measurements.
(A) Drosophila CENP-C organization highlighting the N-terminal outer kinetochore (KT) binding domain (gray), the C-terminal DNA/centromere binding domain (polka dotted), and the placement of the internal force sensor. (B) Disorder profile plot of *Drosophila melanogaster* (*Dm*) CENP-C using the DISOPRED3 disorder prediction method at the PSIPRED Protein Sequence Analysis Workbench (Buchan et al., 2013) (http://bioinf.cs.ucl.ac.uk/psipred/). (C) Schematic of the *Drosophila* kinetochore and the experimental design showing CENP-C-based force sensors placed internally (experimental, force applied) versus at the C-terminus (control, no force applied).

2.2 Results

2.2.1 Measuring kinetochore forces with a FRET-based sensor

The first CENP-C force reporter was built using a modified version of a spider-silk-based FRET sensor called TSMod (tension sensor module) (Grashoff et al., 2010), comprised of the FRET pairs mTurquoise2 and mVenus flanking an elastic linker (Fig. 2.2). The application of force to TSMod leads to reduced FRET and, notably, the FRET sensor has been calibrated and shown to report on forces in the 1-6 pN range. Insertion of the TSMod reporter into CENP-C did not evidently disrupt its function as chromosome alignment was indistinguishable between control cells and cells treated with dsRNA targeting the 3'-untranslated region (3'-UTR) of the CENP-C transcript to knockdown (with ~50 - 60% efficiency) the endogenous CENP-C (Fig. 2.3A). CENP-C-TSMod exhibited a normal localization pattern as, like wildtype CENP-C, it constitutively associated with centromeres throughout the cell cycle when expressed in S2 cells (Fig. 2.3B). Interphase cells, which do not have assembled kinetochores, were used as the low/no force condition while bioriented metaphase kinetochores were the higher force condition. First, the FRET emission ratio (FRET signal / Donor (mTurquoise2) signal) of the reporter was measured. A statistically significant 7% decrease (p-value < 0.005) in the FRET emission ratio was measured in metaphase compared to interphase cells expressing the internal TSMod (Fig. 2.4A-B). The metaphase reduction in FRET was not a result of cell cycle effects on the behavior of the reporter and was dependent on the internal positioning of the sensor as there was not a statistically significant difference (p-value > 0.05) in

the FRET emission ratio of the C-terminal TSMod in interphase versus metaphase cells.

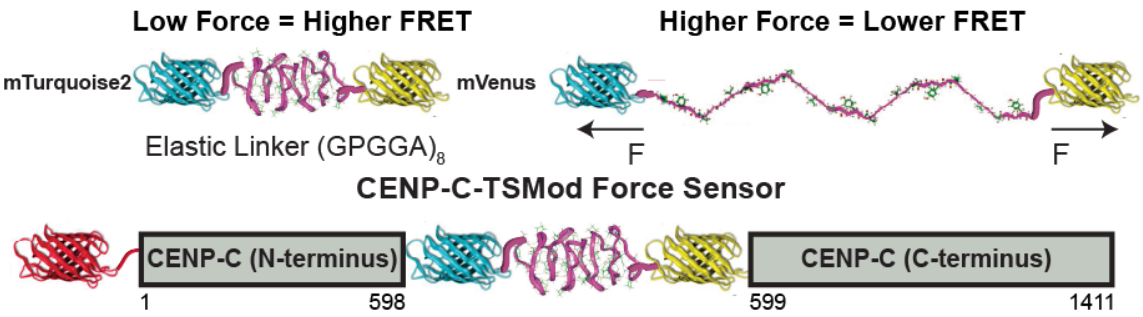

Figure 2.2. FRET based force sensor.
The TSMod force sensor is composed of an elastic linker flanked by two compatible fluorophores for FRET microscopy. The force sensor exhibits reduced FRET in response to applied opposing force, which results in separation of the two fluorophores. The TSMod force sensor is inserted into the middle of TagRFP-T-CENP-C to measure the magnitude of force being exerted on the kinetochore.

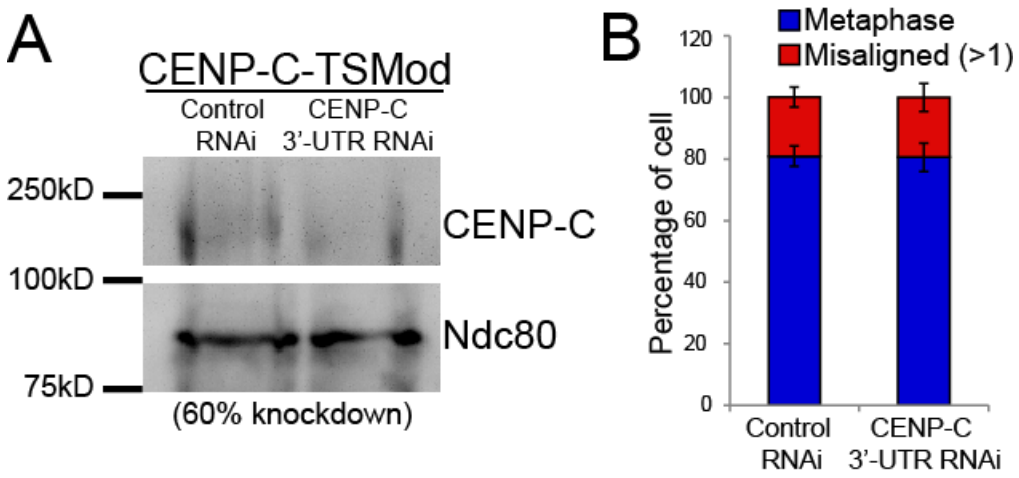

Figure 2.3. CENP-C-TSMod rescues FL CENP-C function.
(A) Western blot showing the level of endogenous CENP-C knockdown, with Ndc80 as a loading control. (B) Quantification of chromosome alignment in control and endogenous CENP-C depleted, internal CENP-C-TSMod expressing cells treated with MG132. Mean values from two independent experiments; Control RNAi: n = 105 cells, CENP-C 3'UTR RNAi; n = 104 cells. Error bars are SEM.

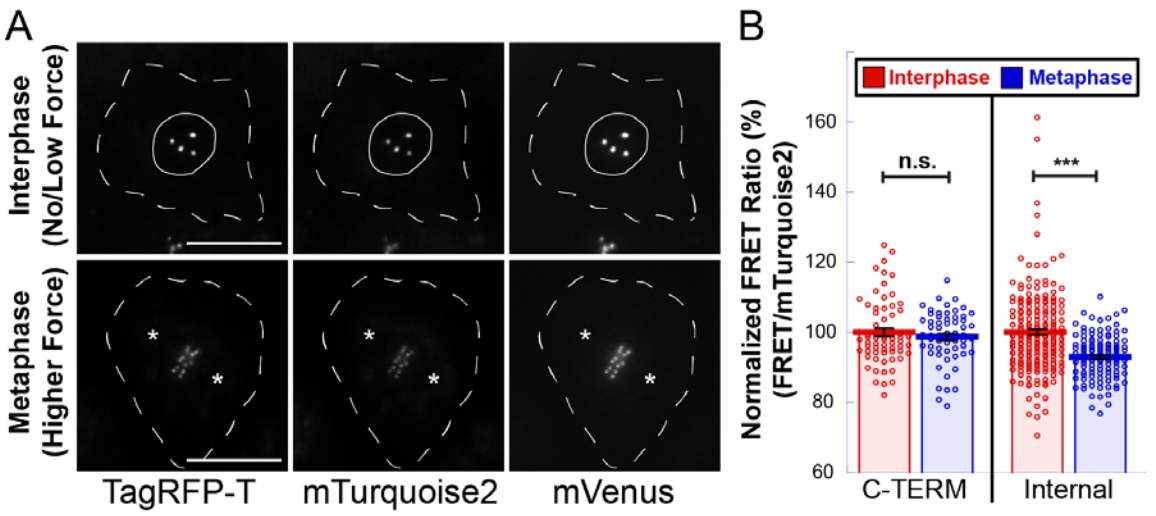

Figure 2.4. Bioriented kinetochores exhibit lower FRET ratio than interphase kinetochores.

(A) Cellular localization of the internal CENP-C-TSMod. Dashed lines denote cell boundaries, a solid line outlines the nucleus, and asterisks mark spindle poles. Comparable channels are displayed with identical contrast and brightness scaling. (B) FRET emission ratios of the internal and C-terminal reporters normalized to the interphase condition (set to 100%) for each reporter. C-terminal data are rom two independent experiments; n = 67 interphase cells, n=60 metaphase cells. Internal data are from three independent experiments; n=198 interphase cells, n=124 metaphase cells. Scale bar is 10μm. Error bars are SEM. P-values from Mann-Whitney Wilcoxon t-tests are reported: not significant (n.s.), p-value >.05, ***p-value 0.0005.

While the reduction in FRET emission ratio indicated that the internally positioned TSMod was under greater tension in metaphase than in interphase, it was difficult to estimate the magnitude of force applied to CENP-C from the change in the emission ratio as the reporter was originally calibrated based on changes in FRET efficiency. To overcome this limitation, acceptor photobleaching was applied to measure the FRET efficiency of the CENP-C TSMod reporters (Fig. 2.5A). In this approach, the FRET efficiency is measured by quantifying the extent to which the fluorescence intensity of the donor (mTurquoise2) increases following photobleaching of the acceptor (mVenus). In general agreement with the FRET emission ratio measurements, a statistically significant ~12.5% decrease (p-value < 0.005) in the FRET efficiency of the internal TSMod reporter was measured in metaphase (20.7 +/- 0.5% FRET efficiency) compared to interphase (23.6 +/- 0.6% FRET efficiency) while there was not a statistically significant (p-value > 0.05) change in the FRET efficiency of the C-terminal reporter (Fig. 2.5B). Chromosome biorientation was required to generate tension as the FRET efficiency of the internal TSMod at kinetochores associated with monopolar spindles following depletion of kinesin-5 was indistinguishable from interphase measurements (Fig. 2.5). Importantly, there was negligible (< 0.5%) or no detectable bleed-through from the TagRFP signal into any of the relevant channels used in the FRET-based imaging approaches. The live-cell FRET efficiency measurements compared remarkably well with the FRET efficiency-force estimation of the TSMod developed from single molecule calibrations(Grashoff et al., 2010). Based on the published force estimation

curve, the CENP-C-TSMod data are consistent with each CENP-C molecule experiencing forces below the limit of detection in interphase and, on average, ~1.2 - 1.4 pN at bioriented kinetochores (Fig. 2.5C).

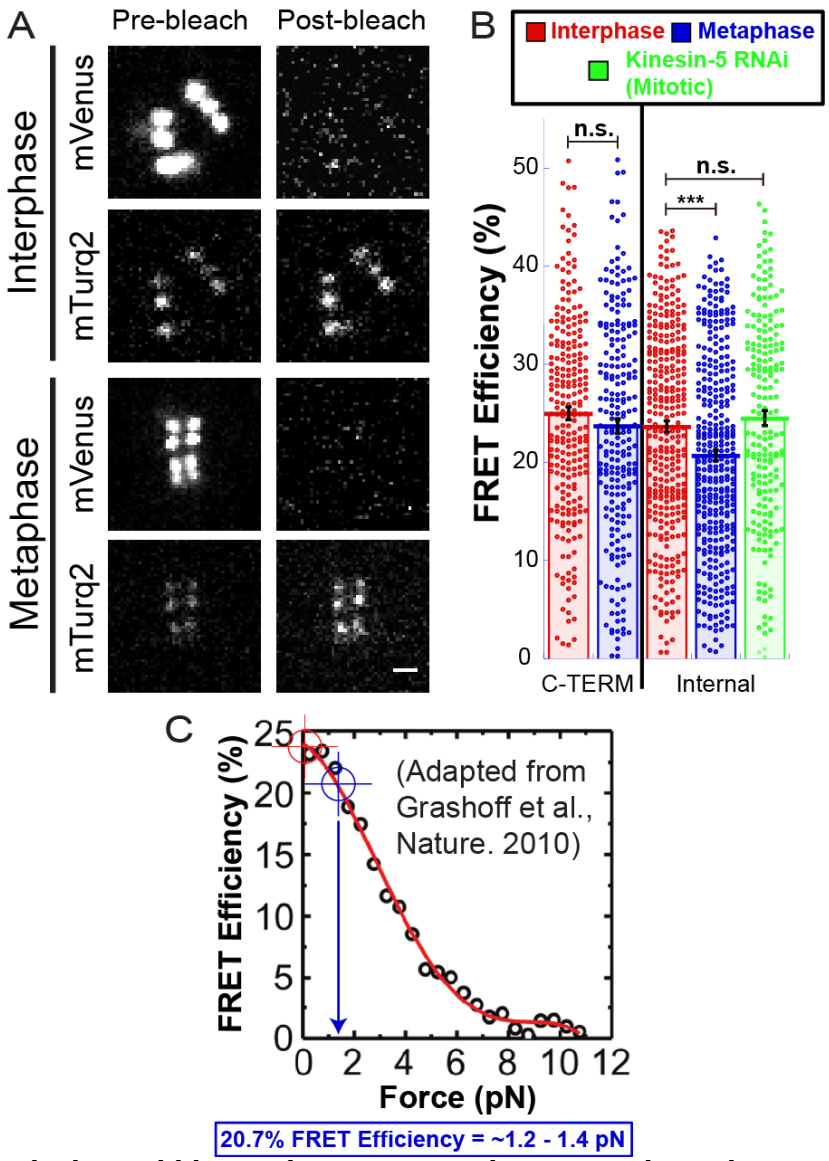

Figure 2.5. Bioriented kinetochores are under approximately 1pN of force. (A) A representative example of an acceptor photobleaching experiment of the internal TSMod. Comparable channels are displayed with identical contrast and brightness scaling. (B) FRET efficiency measurements from acceptor photobleaching experiments. C-terminal data are from 3 independent experiments; n=238 interphase centromeres, n=229 metaphase centromeres/kinetochores. Internal data are from 4 independent experiments; n=318 interphase centromeres, n=346 metaphase centromeres/kinetochores for untreated cells and 2 independent experiments for kinesin-5 RNAi-treated cells; n=198 metaphase centromeres/kinetochores (Kinesin-5 RNAi). (C) Based on the published calibration of the TSMod reporter(Grashoff et al., 2010), a 20.7% FRET efficiency of the internal CENP-C TSMod reporter corresponds to the application of ~1.2 – 1.4 pN. The red and blue crosshairs denote the mean FRET efficiency values of the internal TSMod reporter in interphase and metaphase cells respectively. Scale bars are 1 μm. Error bars are SEM. Two-tailed p-value of Student's t-test is reported for the C-terminal data in (B) otherwise p-values from Mann-Whitney Wilcoxon t-tests are reported: not significant (n.s.) p-value > 0.05, * p-value < 0.05, *** p-value < 0.0005.

2.2.2 MT dynamics contributes to metaphase force generation

The MT-stabilizing drug taxol was next used to assess the contribution of MT dynamics to kinetochore forces. Addition of taxol above concentrations of ~20-50 nM to *Drosophila* S2 cells results in monopolar spindles, but bipolar spindles form more frequently in the presence of higher concentrations of taxol following depletion of the minus-end directed motor dynein (Maresca and Salmon, 2009). While normal metaphase tension was generated at bioriented kinetochores in DMSO-treated cells following dynein heavy chain (Dhc) depletion, addition of 500 nM taxol resulted in a statistically significant (p-value < 0.05) increase in the FRET efficiency of the internal CENP-C-TSMod reporter at bioriented kinetochores in Dhc-depleted cells (Fig. 2.6). Thus, MT dynamics, but not the minus-end directed motor protein dynein contribute to force production at bioriented kinetochores.

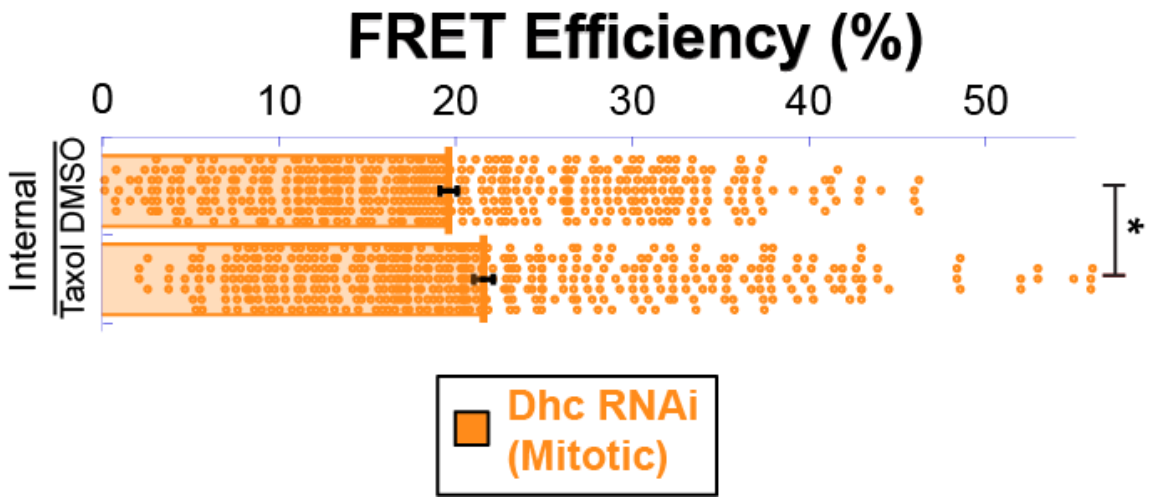

Figure 2.6. Force applied to bioeriented kinetochores requires dynamic microtubules.
FRET efficiency measurements from acceptor photobleaching of the internal TSMod reporter in mitotic Dhc-depleted cells treated with DMSO or 500 nM taxol. The Dhc RNAi data are from 5 independent experiments; n = 454 bioriented kinetochores in DMSO-treated cells, n = 433 bioriented kinetochores in taxol-treated cells. Dhc RNAi treatment exhibited the expected phenotype of a significant increase in metaphase cells.

2.2.3 Measuring kinetochore forces with focal adhesion components

To corroborate the FRET-based measurements, a second CENP-C force reporter was designed based on the focal adhesion protein talin and its binding partner vinculin. Single molecule experiments with the talin rod (TR) domain demonstrated that the application of force to the molecule increased the number of associated vinculin head (VH) molecules purportedly by exposing vinculin binding sites in the TR domain (Fig. 2.7A)(del Rio et al., 2009). As with the TSMod reporter, the TR domain was inserted into either the middle of TagRFP-T-CENP-C to measure force or at the C-terminus to serve as a negative control (Fig. 1b). Cell lines were built that expressed both VH-EGFP and the CENP-C-TR force sensors based on the hypothesis that the application of force to the TR domain in CENP-C should increase the number of bound VH molecules (Fig. 2.7B).

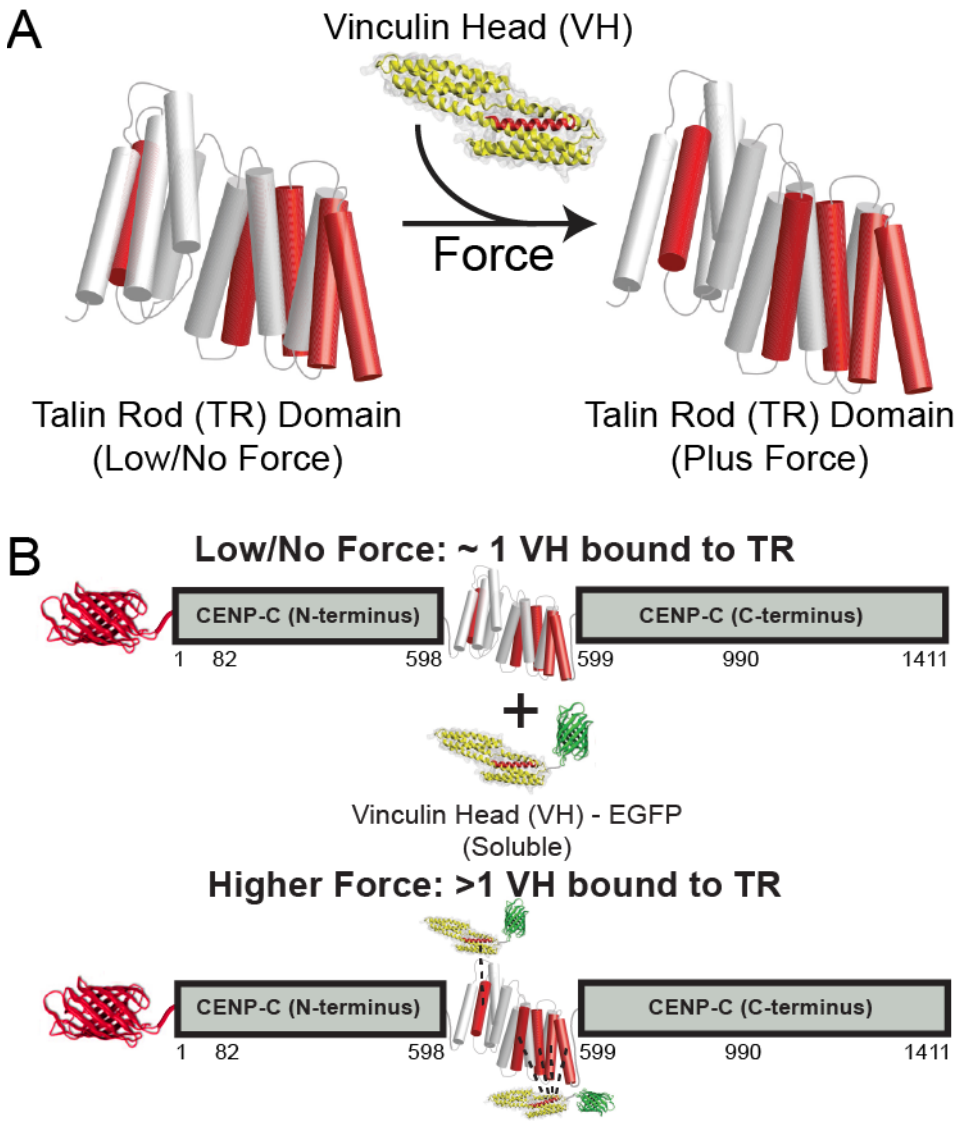

Figure 2.7. Force sensor based on focal adhesion Vinulin and Talin proteins.
(A) Schematic of the proposed effects of force on the structural organization of the TR domain and the potential exposure of VH binding sites in the TR domain based on a theoretical model of the chicken talin rod domain used here (aa 482-889)(Critchley, 2009). The red regions represent VH-binding domains in TR and the TR binding domain in VH. (B) Experimental design of the internal CENP-C-TR reporter in cells co-expressing soluble VH-EGFP. The dashed lines represent potential VH-TR interactions.

As observed for the TSMod force sensor, insertion of the TR reporter into the middle of CENP-C did not disrupt its function as chromosome alignment was normal in CENP-C-TR-expressing cells depleted of endogenous CENP-C (Fig. 2.8). Importantly, VH-EGFP localized to kinetochores in a CENP-C-TR-dependent manner (Fig. 2.9 A). To quantify the number of VH molecules associated per TR domain, a fluorescence correction ratio was determined prior to imaging the experimental conditions by imaging a reference CENP-C protein with an equal number of EGFP and TagRFP-T fluorophores. The correction ratio was then applied to the measured fluorescence intensities of VH-EGFP and Tag-RFP-T-tagged CENP-C-TR, which were imaged using the identical imaging parameters as the reference conditions. Since the assay involved a two component system and the VH-EGFP was distributed through the cytoplasm, nucleoplasm, and centromeres during interphase, the low/no force condition was created by generating unattached kinetochores through treatment with the MT-depolymerizing agent colchicine. The internal TR-reporter associated with an average of ~0.9 +/- 0.02 VH-EGFP molecules in colchicine-treated cells. There was not a significant difference (p-value > 0.05) between VH molecules bound per TR in colchicine-treated and metaphase cells expressing the C-terminal reporter although the mean number of VH molecules per TR was lower (~0.75 +/- 0.03) for the C-terminal reporter. Importantly, in metaphase cells expressing the internal TR, the VH-EGFP signal at bioriented kinetochores was brighter than at unattached kinetochores with an average of ~1.3 +/- 0.05 VH molecules per CENP-C-TR (Fig. 2.9 B). Fluorescence measurements were not impacted by the

fact that TagRFP-T and EGFP is a FRET pair as FRET was not detectable in either metaphase or colchicine-treated cells. The number of VH molecules per TR domain was counted in the absence of force and after applying 2 or 12 pN to single TR molecules with a magnetic trap(del Rio et al., 2009). While these measurements were done in vitro rather than in living cells, we feel that the approach employed here is bolstered by the fact that a comparable number of VHs per TR was measured in vitro in the absence of applied force and in colchicine-treated cells expressing the internal TR reporter (Fig. 2.9 C). The measurement of ~1.3 VH molecule bound per internal TR domain in living cells is slightly below the average number of VH molecules bound to a TR domain under 2 pN of force applied in vitro (Fig. 2.9 C).

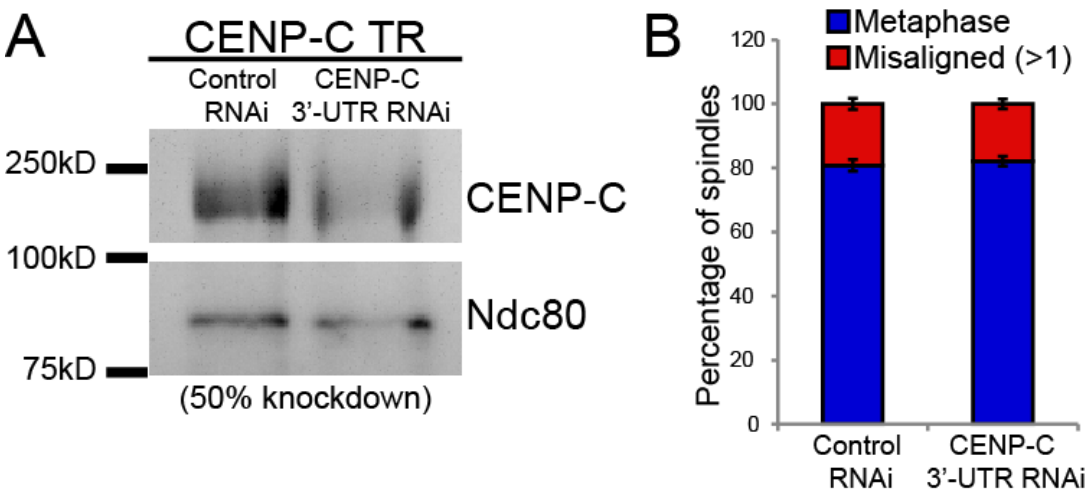

Figure 2.8. CENP-C TR rescues FL CENP-C functions.
(A) Western blot showing the level of endogenous CENP-C knockdown, with Ndc80 as a loading control. (B) Quantification of the percentage of MG132-treated cells with metaphase plates and >1 misaligned chromosomes in control and endogenous CENP-C depleted internal CENP-C-TR expressing cells (representative western blot - upper panel). Mean values from 3 independent experiments; Control RNAi; n = 162 cells, CENP-C 3'-UTR RNAi; n = 162 cells. Error bars are SEM.

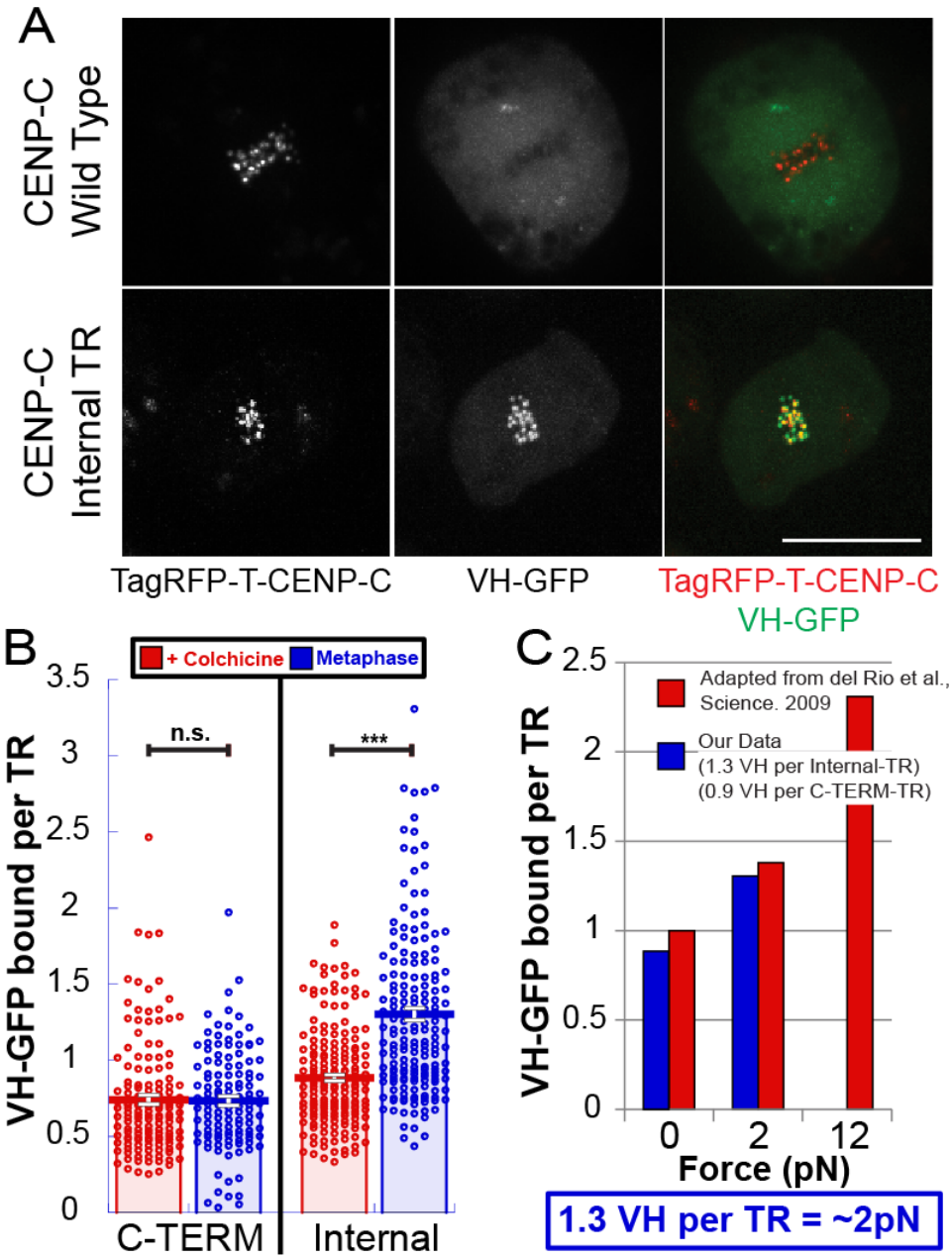

Figure 2.9. Localization and measurements using the TR force sensor. (A)VH-EGFP localizes to kinetochores in cells expressing CENP-C-TR but not wild type CENP-C. (B) Counting the number of VH-EGFP molecules associated per TR domain in the internal and C-terminal TR reporters in colchicine-treated and metaphase cells. The C-terminal TR data are from 5 independent experiments; n = 146 colchicine-treated cells, n = 125 metaphase cells. The internal TR data are from 6 independent experiments; n = 182 colchicine-treated cells, n = 179 metaphase cells. (C) Force estimation of the internal CENP-C-TR reporter based on published VH counting from single TR molecule magnetic trap experiments(del Rio et al., 2009). Scale bar is 10 μm. Error bars are SEM. p-values from Mann-Whitney Wilcoxon t-tests are reported: not significant (n.s.) p-value > 0.05, *** p-value < 0.0005.

2.3 Discussion

The TSMod- and TR-based reporters indicated that each CENP-C molecule experiences, on average, ~1 - 2 pN of force at bioriented kinetochores. It is important to recognize that both the FRET efficiency measurements and VH counting numbers come from ensembles of molecules some of which are likely in a resting state and others that are in a tense state. Furthermore, since all the measurements are done in the presence of endogenous CENP-C it is possible that the load could be shared unequally between the tagged and untagged CENP-C molecules or distributed through a greater number of CENP-C molecules than are typically present. Thus, the 1 - 2 pN per CENP-C estimate by no means excludes that forces are differentially distributed through individual CENP-C linkages, and may even underestimate the magnitude of force that can be applied to CENP-C. Nevertheless, the average estimate provides a solid framework from which to parlay our experimental findings into a reasonable proposal for a physiologically relevant range of forces produced by individual kt-MTs and the k-fiber as a whole. The MT and k-fiber estimates are based upon a generally accepted concept of the structural organization of the kinetochore (reviewed in(Rago and Cheeseman, 2013)), measurements of the number of CENP-C molecules (Joglekar et al., 2006; Lawrimore et al., 2011; Schittenhelm et al., 2010) and kt-MTs (Maiato et al., 2006) per *Drosophila* kinetochore, and the force per CENP-C molecule measured here (Fig. 2.10). The upper and lower limits of the proposal are defined by the range of force per CENP-C (1 - 2 pN) and previously reported *Drosophila* CENP-C counting experiments (Joglekar et

al., 2006; Lawrimore et al., 2011; Schittenhelm et al., 2010) based on a fluorescent standard (12 – 31 per MT). In *Drosophila*, we posit that the force produced by a single MT at mature bioriented attachments is distributed between CENP-C molecules arranged as a set of parallel springs that connect to the MT through the Mis12 complex and the Ndc80 complex. It would therefore hold that the force a single MT generates would be the number of CENP-C molecules (12 - 31) multiplied by the force applied to each CENP-C molecule (1 – 2 pN) meaning that, on average, a kt-MT exerts ~12 - 62 pN of poleward-directed force. The total force applied to the kinetochore would equal the force per MT multiplied by the number of MTs in the k-fiber. Since there is an average of 11 microtubules bound to *Drosophila* S2 cell kinetochores (Maiato et al., 2006), we propose that a typical bioriented kinetochore in these metazoan cells experiences between ~135 and 680 pN of poleward-directed pulling forces. This magnitude of force differs significantly from that measured in live-cell optical trapping experiments (Ferraro-Gideon et al., 2013), but largely agrees with the classic cell-based microneedle experiments in insect cells (Nicklas, 1983; Nicklas, 1988) as well as with the force estimate from a recent study combining experimentation and computational theory in mammalian cells (Kajtez et al., 2016).

We favor the interpretation that the depolymerizing kt-MT plus-end is the dominant poleward-directed force producer at bioriented *Drosophila* kinetochores for several reasons: 1) our estimate of up to 62 pN per kt-MT nearly equals measurements of the maximum amount of force depolymerizing MT plus-ends generate in vitro (Grishchuk et al., 2005), 2) suppressing plus-end MT dynamics

with 500 nM taxol reduces the amount of force at bioriented kinetochores. Prior work concluded that 1 μM taxol was necessary to fully suppress MT dynamics in S2 cells (Maresca and Salmon, 2009); unfortunately, sufficient numbers of bioriented kinetochores could not be measured in 1 μM taxol. While the data indicate that dynein is not a major force-generator at metaphase kinetochores, regulators aside from MTs may contribute since 500 nM taxol did not reduce the force to interphase levels. We cannot exclude the possibility; however, that 500 nM taxol dampens but does not fully suppress MT dynamics. Interestingly, since kinetochore/centromere associated kinesin-13 family members are capable of depolymerizing taxol-stabilized MT ends (Desai et al., 1999), it would be worthwhile to further investigate the contribution of these motors to force generation at bioriented kinetochores. It is also noteworthy that just 10 nM taxol is sufficient to reduce kt-MT flux by >90% in S2 cells(Matos et al., 2009) and so our data do not rule out k-fiber flux as a contributor to metaphase force generation. Given that k-fibers flux and pull, and that polymerizing and depolymerizing MTs are present within the same kinetochore(McIntosh et al., 2008; VandenBeldt et al., 2006), the relative contributions of kt-MT polymerization versus plus (and perhaps minus)-end depolymerization to kinetochore force transduction remains an open and important question, which has recently been investigated using FRET-based Ndc80 reporters in budding yeast (Suzuki et al., 2016).

We hypothesize that kt-MT plus-end depolymerization sets the maximum force applied to bioriented kinetochores and that this limit must be highly

conserved since it is derived, at its most fundamental level, from GTP hydrolysis (Koshland et al., 1988; McIntosh et al., 2010). Thus, kinetochores likely emerged and evolved in the presence of an evolutionarily fixed maximum force generator - the depolymerizing kt-MT. A common evolutionary strategy to building a kinetochore appears to have involved distributing k-fiber forces through a sufficient number of linkages such that individual components are not subjected to very high forces that would denature them or damage the underlying DNA. Defining the physical properties of force-transducing kinetochore components as well as how forces are transmitted across them will provide fundamental mechanical insights into kinetochore function, and cell division in general.

Why would cell division in metazoan cells benefit from having k-fibers capable of applying hundreds of pNs to kinetochores when much lower forces are sufficient to move chromosomes? It is possible that the ability of k-fibers to produce high forces allows for proper resolution of merotelic attachments in anaphase (Cimini et al., 2003) or for segregating chromatids to plow through unexpected cytoplasmic obstacles that may arise. However, because the measurements here are in close agreement with Nicklas' estimates of the amount of force (30 pN / MT) required to stabilize kt-MT attachments (Nicklas, 1988), we propose that the application of hundreds of pNs to kinetochores is most critical before anaphase to stabilize the geometrical configuration with the best segregation prospects - bioriented attachments.

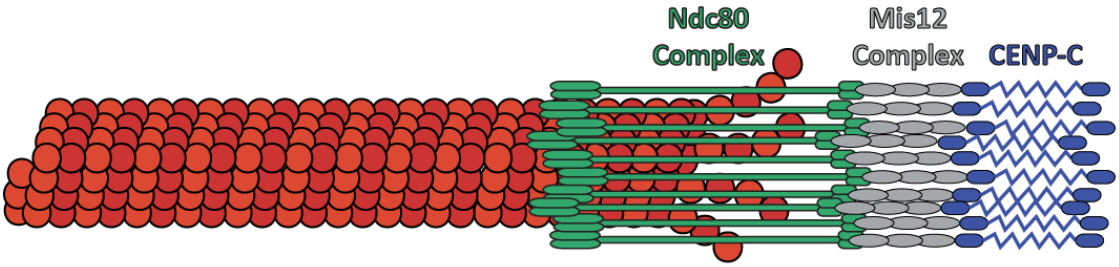

A simple *Drosophila* kinetochore model: Linkages arranged as a set of parallel springs

$$F_{MT} = F_{CENP\text{-}C} \times \#\ \text{CENP-C molecules per MT}$$

$$F_{kt} = F_{MT} \times \#\ \text{kinetochore-microtubules}$$

	$F_{CENP\text{-}C}$	# CENP-C per MT	F_{MT}	# kt-MTs^{+}	Max F_{kt}
Low	1 pN	12.3*	12.3 pN	11	135 pN
High	2 pN	30.8**	61.5 pN	11	677 pN

Figure 2.10. An estimate of the magnitude of force that is applied to a bioriented kinetochore.
The *Drosophila* kinetochore is envisioned as linkages between the DNA and the kt-MT arranged as a set of parallel springs that distribute forces produced by MT dynamics through linkages that bind to the MT. In *Drosophila* the path from the DNA to the MT is CENP-C, the Mis12 complex, and the MT-associating Ndc80 complex. For simplicity, Spc105/KNL1 has been omitted. The TSMod- and TR-based force sensors reported that each CENP-C molecule experiences, on average, ~1 - 2 pN of force. If the poleward force produced by a kt-MT is equally distributed across the CENP-C linkages then, based on CENP-C counting experiments, each kt-MT could generate between ~12 – 62 pN. Since there are 11 MTs bound to S2 cell kinetochores, if each kt-MT applies maximum poleward force then the total force applied to the kinetochore would be as high as 135 – 677 pN. *Measured by Schittenhelm et al.(Schittenhelm et al., 2010) based on Cse4 standards from Joglekar et al.(Joglekar et al., 2006) **Adjusted 2.5-fold based on recalibrated fluorescence measurements by Lawrimore et al.(Lawrimore et al., 2011) $^{+}$Measured in *Drosophila* S2 cells by Maiato et al.(Maiato et al., 2006)

2.4 Methods

2.4.1 Drosophila S2 cell lines

All cell lines were cultured in Schneider's (Life Technologies) media supplemented with 10% heat inactivated fetal bovine serum and 0.5x antibiotic-antimycotic cocktail (Life Technologies), maintained at 25°C. Transgenic cell lines were generated by transfecting DNA constructs using the Effectene Transfection Reagent system (Qiagen), following manufacturer protocol. Protein expression was confirmed by fluorescence microscopy. Cells were split in the presence of Blasticidin S HCl (Fisher) and/or Hygromycin (Sigma) to select for expressing cells.

2.4.2 DNA Constructs

The pMT-TagRFP-T-CENP-C construct was generated in multiple steps: (1) CENP-C was amplified from the cDNA, with 5' SpeI and 3' SacII sites and inserted into pMT-V5 B vector; (2) endogenous CENP-C promoter was amplified from genomic DNA with 5' XbaI site and 3' KpnI site and inserted into the above plasmid purified from dam-/dcm- E. coli; (3) TagRFP-T was amplified with 5'KpnI and 3'SpeI sites, and inserted between the promoter and CENP-C. Then, CENP-Cprom-TagRFP-T-CENP-C was amplified from the above construct with flanking XbaI sites and inserted into pMT-V5 B vector purified from dam-/dcm- E. coli to generate pMT-CENP-Cprom-TagRFP-T-CENP-C. To generate the tension sensor module (TSMod) construct, mTurquoise2 and mVenus were first inserted into pMT-V5 B vector between KpnI and SpeI sites, and NotI and SacII sites, respectively to build pMT-mTurquoise2-mVenus. The spider silk DNA sequence

with flanking homology regions to mTurquoise2/SpeI site (5' end) and NotI/mVenus (3' end) was synthesized (Life Technologies) and inserted between mTurquoise2 and mVenus in the pMT-mTurquoise2-mVenus plasmid by Gibson assembly. To generate the CENP-C-TSmod construct, the TSMod was amplified from the above construct with primers upstream of mTurquoise2 and downstream of mVenus with flanking ClaI sites, and inserted into pMT-CENP-C-prom-tagRFP-T-CENP-C purified from dam-/dcm- E. coli. To generate the control construct with the tension sensor in the C-terminus of CENP-C, a ClaI site was engineered into a pMT-CENP-Cprom-TagRFP-T-CENP-C (no stop codon) construct by inserting annealed complementary oligos encoding a ClaI site flanked by XbaI sites downstream of CENP-C at the XbaI site and the TSMod was then inserted into this newly engineered ClaI site as the internal ClaI site in CENP-C was methylated.

The CENP-C-TR construct was generated by amplifying talin rod domain (a.a. 482-889) from chicken gizzard cDNA (Zyagen) with flanking ClaI sites, and inserted into the pMT-CenpCprom-TagRFP-T-CENP-C construct described above. To generate the control construct, in which talin rod was at the 3' end of CENP-C, the rod domain was amplified with flanking XbaI sites and inserted downstream of CENP-C.

To generate the VH-GFP construct, the vinculin head domain (a.a. 1-258) was PCR amplified from a vinculin-mVenus construct [a gift from Martin Schwartz (Addgene plasmid # 27300)] with 5' KpnI and 3' XbaI sites and inserted into the pMT-V5 B vector with the EGFP sequence between the XbaI and SacII sites.

The CENP-C promoter was then inserted upstream of the vinculin gene with flanking KpnI sites to drive expression.

2.4.3 Double stranded RNA production

DNA templates for Dhc64C (CG7507), KLP61F (CG9191), and CENP-C 3'-UTR (CG31258) were produced to contain ~500 bp of complementary sequence flanked by T7 promoter sequence. dsRNAs were synthesized overnight at 37°C from the DNA templates using the T7 RiboMax Express Large Scale RNA Production System (Promega) following manufacturer protocol. For RNAi, media was aspired off semi-adhered cells at 25% confluence, replaced with 1ml of serum-free Schneider's medium containing 20µg of dsRNA, and after 1h, 1ml of fresh Schneider's plus FBS was added to the wells and incubated for 2 (Dhc, Klp61F) or 4 (CENP-C) days at 24°C.

2.4.4 Western blot

A total of 20 µg of protein was loaded onto a 10% SDS-PAGE gel, run out, and transferred to a nitrocellulose membrane on the Trans-Blot® Turbo™ transfer system (Bio-Rad Laboratories) for 15 min. All antibodies were diluted in TBS with 0.1% Tween and 5% milk. The membrane was first incubated with anti-CENP-C serum (gift from Bibi Mellone) at 1:7500, followed by anti-Ndc80 antibody (made in house) at 1:5000 as a loading control. Guinea pig (703-035-155) and chicken (706-035-148) HRP secondary antibodies (Jackson ImmunoResearch Laboratories, Inc.), diluted at 1:5000, were used in conjunction with their respective primaries and imaged with a GBox system controlled by GeneSnap software (Syngene). ImageJ was used to measure band intensities and the

CENP-C signal was normalized to the Ndc80 loading control to determine the knockdown efficiency.

2.4.5 FRET ratio imaging and analysis

Cells were allowed to adhere to acid-washed, concanavalin A (Sigma-Aldrich) coated coverslip (Corning) for exactly 1 hour, then assembled into a rose chamber containing Schneider's media with drugs or solvent control, when appropriate, and subjected to imaging at 25°C. Cells were imaged for a maximum of 1 hour on a TiE inverted microscope (Nikon) equipped with an iXON EMCCD camera (Andor Technology) using a 100x 1.4 NA Plan Apo violet-corrected series differential interference contrast objective (Nikon). Metamorph software (Molecular Devices) was used to control the imaging system. For imaging the TagRFP-T-CENP-C-TSMod FRET reporter, mitotic cells were identified by the presence of paired sister centromeres and the absence of a nucleus, and the best focal plane was determined in the RFP channel. Sequential images of mTurquoise2, mVenus, and FRET were taken with equal exposure times. Background-corrected fluorescence intensities for mTurquoise2 and FRET were measured in Metamorph software using region-in-a-region background subtraction by drawing concentric larger and smaller regions manually in MetaMorph around clusters of kinetochores/centromeres that were in focus. Bleed-through of the TagRFP-T into the CFP, YFP, and FRET channels was measured by imaging TagRFP-T-α-tubulin-expressing cells under identical conditions as the FRET imaging experiments. Background corrected CFP, YFP,

and FRET signals in MT-containing regions were then ratioed to the TagRFP signal from that region. The following equations were used:

$$(1)\ \text{Background signal} = \frac{\text{Integrated fluorescence intensity}_{\text{big area}} - \text{Integrated fluorescence intensity}_{\text{small area}}}{\text{Big Area} - \text{Small Area}}$$

$$(2)\ \text{Total Intensity} = \text{Integrated fluorescence intensity}_{\text{small area}} - (\text{Background signal} \times \text{Small Area})$$

The reported FRET emission ratios represent the ratios of the background corrected FRET signal over the background corrected mTurquoise2 signal.

2.4.6 Acceptor Photobleaching FRET

Cells were seeded onto a Concanavalin A coated acid-washed coverslip and allowed to adhere for 1 h. For Dhc RNAi experiments, cells were incubated for 1 h in taxol or 0.1% DMSO after allowing them to adhere to the coverslips for 1 h and imaging was done for a maximum of 60 minutes following the 1 h drug or DMSO treatment. Coverslips were then assembled into a rose chamber containing Schneider's media (containing 500 nM taxol or 0.1% DMSO where appropriate) and imaged at 25°C. All images were collected using a TiE inverted microscope (Nikon) coupled with A1R laser scanning confocal system (Nikon) using a 60x 1.4 NA Plan Apo objective (Nikon). Elements (Nikon) was used to control the imaging system. Best focal plane was determined by taking a single image using the 561nm laser. Single plane images were acquired using the 445nm and 514nm lasers pre- and post-photobleaching. To photobleach the acceptor fluorophore, a square region was drawn around a metaphase plate or interphase centromeres, and photobleached with the 514nm laser, using a 50mw

laser at 55% laser power. All image quantifications were done using Fiji Image J software. A region was drawn around individual kinetochores/centromeres in pre- and post- photobleach images to obtain the mTurquoise2 (donor) integrated intensity, which was corrected by subtracting the background signal obtained by placing the same sized region in the cytoplasm/nucleoplasm of the same cell. The following equation was applied to obtain the FRET efficiency:

$$FRET_{eff} = 1 - \frac{Intensity_{donor\ (pre\text{-}bleach)}}{Intensity_{donor\ (post\text{-}bleach)}}$$

All statistical analyses were performed using R or Prism. While mTFP1 was replaced with mTurquoise2 in the TSMod reporter used in this study, we feel that it is appropriate to present a force estimate from our reporter that is based on the theoretical calibration of the original TSMod[36] because the two reporters exhibit identical zero-force FRET efficiencies and have comparable Förster radii. Bleed-through of the TagRFP-T into the CFP and YFP channels was measured by imaging TagRFP-T-α-tubulin-expressing cells under identical conditions as the acceptor photobleaching experiments. Background corrected CFP and YFP signals in MT-containing regions were then ratioed to the TagRFP signal from that region.

2.4.7 Talin rod - vinculin imaging and analysis

Cells co-expressing CENP-C-TR and VH-EGP were seeded near full confluency in 500 μl volume onto concanavalin A coated acid-washed coverslips. After 20 minutes the volume was brought up to 2 mls with fresh Schneider's media (+0.1% DMSO or 25 μM colchicine) and assembled into a rose chamber ~40

minutes after seeding. For colchicine-treatments, the cells were treated with 25 μM colchicine for 60 minutes before seeding them onto coverslips. The cells were then imaged on the microscope described above (in “Fret ratio imaging and analysis”) between 45 - 90 minutes post seeding. Mitotic cells were identified as described above and the best focal plane was determined in the RFP channel and sequential images of TagRFP-T and EGFP were taken with equal exposure times. Background-corrected fluorescence intensities for TagRFP-T and EGFP were measured using region-in-a-region background subtraction as described above. To obtain the correction ratio, cells expressing TagRFP-T-CENP-C-EGFP and treated with 0.1% DMSO were imaged prior to each experiment using identical imaging conditions as would be applied to the experimental conditions. Region-in-a-region background subtraction was applied to measure the ratio of GFP to RFP signal intensities (the GFP signal was typically ~3.5X greater than that of RFP under the imaging conditions). Since TagRFP-T-CENP-C-EGFP has equal numbers of EGFP and TagRFP-T molecules, the correction ratio determined for that day was used to determine the number of VH molecules per TR in the experimental conditions by dividing the background corrected VH-EGFP to TagRFP-T-CENPC-TR ratio by the correction ratio. For example, if the correction ratio for a given day was measured to be 3.5 and the (background corrected) ratio of VH-EGFP to TagRFP-T-CENP-C-TR kinetochore signals was measured to be 7 then the number of VH per TR would be 2. This method does not count the total number of TRs or VHs per kinetochore but rather the number of VH molecules per CENP-C-TR.

To investigate if FRET was occurring between TagRFP-T tagged CENP-C-TR and VH-EGFP, cells were imaged on an Eclipse Ti-E inverted microscope (Nikon) equipped with a Borealis (Andor) retrofitted CSU-10 (Yokogawa) spinning disk head and ORCA-Flash4.0 LT Digital CMOS camera (Hamamatsu) using a 100x 1.49 NA Apo differential interference contrast objective (Nikon). Cells expressing either EGFP-α-tubulin or TagRFP-T-α-tubulin were imaged and background corrected signals from EGFP (donor) and TagRFP-T (acceptor) into the FRET channel (GFP excitation, RFP emission) in MT-containing regions were ratioed to the background corrected tubulin signal from that region to define the spectral bleed-through (*bt*) into the FRET channel (~6% for EGFP, and ~12% for TagRFP-T). TagRFP-T tagged CENP-C-TR and VH-EGFP expressing cells were then imaged under identical imaging conditions as the tubulin-expressing cells and corrected FRET (cFRET) was determined by subtracting the donor and acceptor *bt* from the background corrected raw FRET signal using the following equation:

$$\text{cFRET} = \text{raw FRET} - \text{EGFP}_{bt} - \text{TagRFP-T}_{bt}$$

The corrected FRET values were divided by the donor (EGFP) intensity and reported as a cFRET ratio.

CHAPTER 3

DROSOPHILA NOD, CLASSIFIED AS A NON-MOTILE KINESIN, POSSESSES PLUS-END DIRECTED MOTILITY AND INTERACTS WITH EB1 VIA A NEW MICROTUBULE TIP LOCALIZATION SEQUENCE.

This work was done under the guidance and help of Thomas J. Maresca.

3.1 Introduction

Equal distribution of the duplicated DNA is required to maintain genomic stability through cell division. The MT cytoskeleton is dramatically reorganized to form a bipolar spindle as cells enter mitosis or meiosis. Subsequently, chromosomes are positioned at the spindle equator during a process known as congression. Chromosome movements within the spindle are predominantly mediated by motor proteins that walk directionally on spindle MTs and associate with either kinetochores or chromosomes. CENP-E (Kinesin-7) and dynein are two well-characterized kinetochore-associated motor proteins that move chromosomes toward the mid-spindle and poles, respectively. The plus-end directed CENP-E aids in congressing mis-aligned chromosomes by transporting them along stable, detyrosinated MTs that comprise the kinetochore fibers of bioriented chromosomes (Barisic et al., 2014; Gudimchuk et al., 2013a; Kapoor et al., 2006). In contrast, dynein is a minus-end directed motor that moves chromosomes poleward (Rieder and Salmon, 1994; Yang et al., 2007). In the short term polar movement of chromosomes by dynein opposes congression, but it may promote chromosome congression in the longer term. It has recently been proposed that dynein prevents premature stabilization of erroneously attached chromosomes by positioning them near spindle poles (Barisic and Maiato, 2015), where an Aurora A kinase gradient locally destabilizes kt-MT attachments (Chmatal et al., 2015; Ye et al., 2015). Newly liberated chromosomes would then be free to congress by the actions of kinetochore-associated

CENP-E and MT-plus-end directed motors that bind to chromosome arms called chromokinesins.

Chromokinesins include two kinesin families, kinesin-4 and kinesin-10. Both kinesins work cooperatively to promote chromosome alignment during cell division (Goshima and Vale, 2003; Stumpff et al., 2012; Wandke et al., 2012). Human kinesin-4 (KIF4A) has been shown to be a plus-end directed motor that suppresses plus-end MT dynamics (Bringmann et al., 2004; Hu et al., 2011; Stumpff et al., 2012). The means by which KIF4A promotes chromosome congression is poorly understood especially given its potential PEF dampening activity. To the contrary, the role of kinesin-10 family chromokinesins in congression is more intuitive. The function of vertebrate kinesin-10 (Kid) was initially demonstrated in *Xenopus laevis* egg extracts in which the activity of Xkid, which coats chromosome arms, was required to establish and maintain chromosome arm congression within metaphase spindles (Antonio et al., 2000; Funabiki and Murray, 2000; Takagi et al., 2013). Depletion of Xkid from *Xenopus* egg extracts resulted in striking mis-alignment of chromosome arms, and while data from human cells have consistently shown that hKid contributes to congression, the alignment defects observed in tissue culture cells have not been as severe as those initially observed in the egg extract system (Levesque and Compton, 2001; Stumpff et al., 2012; Tokai-Nishizumi et al., 2005; Wandke et al., 2012). In fact, the hKid depletion phenotype is similar to that of CENP-E depletion, which typically results in several polar mis-aligned chromosomes, while the majority of chromosomes congress (Schaar et al., 1997; Wood et al., 1997). The similarity in the phenotypes of CENP-E and kinesin-10 depletions is consistent with the two proteins promoting congression as plus-end directed motors. Indeed, vertebrate kinesin-10s have been shown to possess plus-end directed motility and to generate force when bound to chromatin (Bieling et al., 2010; Brouhard and Hunt, 2005; Stumpff et al., 2012; Yajima et al., 2003).

The *Drosophila* kinesin-10 orthologue was initially identified and characterized genetically as the mutant no distributive disjunction (*nod*), which exhibited high frequencies of nondisjunction and chromosome loss in female meiosis (Carpenter, 1973; Zhang and Hawley, 1990). The nod gene was later cloned and found to encode a kinesin-like protein (NOD) with an N-terminal motor domain (Zhang et al., 1990). Detailed microscopy of oocytes lacking functional NOD protein revealed that achiasmate (nonexchange) chromosomes often failed to associate with spindles or were mis-positioned near spindle poles (Theurkauf and Hawley, 1992). The characterization of DNA binding activities in the C-terminus of NOD (Afshar et al., 1995b; Cui and Hawley, 2005) combined with knowledge of its N-terminal motor domain and mis-alignment phenotype supported the conclusion that NOD is the molecular mediator of PEF generation in fly oocytes (Afshar et al., 1995a) and later work in *Drosophila* tissue culture cells revealed a role for NOD in mitotic chromosome congression (Goshima and Vale, 2003). Although NOD possesses a conserved N-terminal motor domain and MT-stimulated ATPase activity, extensive efforts have failed to reconstitute directional motility *in vitro* (Matthies et al., 2001) leading to NOD being classified as a non-motile kinesin. How could a non-motile kinesin generate force? An alternative theory posits that, due to unique mechano-chemical properties of its motor domain, NOD may move chromosomes by associating with the plus-ends of polymerizing MTs (Cochran et al., 2009; Cui et al., 2005) although direct evidence for this mechanism is lacking. Physiological insights into NOD-based force production came from high resolution imaging of NOD-coated chromatin stretching that exhibited properties indicative of both plus-end directed motility and end-tracking coincident with EB1 comets (Cane et al., 2013).

3.2 Results

NOD possesses an N-terminal motor domain and two distinct C-terminal DNA binding regions comprised of HMG (high mobility group) repeats and a helix-hairpin-helix motif that mediate chromatin-association of full length (FL) NOD-mCherry throughout the cell cycle in *Drosophila* S2 cells. (Fig. 3.1 and 3.2). Between the motor and DNA-binding domains, NOD is predicted to contain intrinsically disordered regions (~50%) as well as four alpha-helices, one of which has a low probability of forming a parallel two-stranded coiled-coil (Buchan et al., 2013; Lupas et al., 1991). In order to dissect NOD motor function in vivo, truncations of NOD tagged at their C-termini with mCherry were expressed in GFP-α-tubulin expressing *Drosophila* S2 cells (Fig. 3.3). Interestingly, the motor domain alone (1-324) was not enriched on MTs in either mitosis or interphase, but rather appeared diffuse through the cytosol. Thus, unlike many well-characterized motor proteins, the NOD324 motor domain exhibits weak or no MT binding activity in cells. Given the high physiological concentration of ATP (mM range), this observation is in agreement with *in vitro* studies in which the nucleotide-bound state of the NOD motor domain exhibited significantly lower MT binding affinities (~6 - 8 μM) in the presence of excess ATP than conventional kinesin motors (Cochran et al., 2009; Matthies et al., 2001).

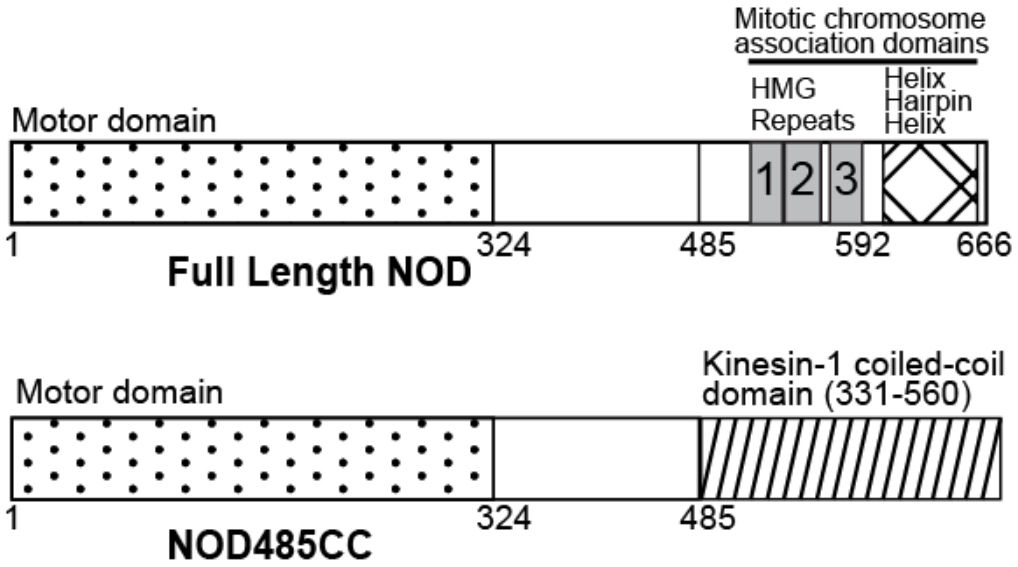

Figure 3.1. Schematic of the NOD constructs expressed in cells.
Full length NOD has a N-terminal motor domain (a.a. 1-324) and two chromatin associating domains, HMG repeats and helix hair helix, in the C-terminus. The region just downstream of the motor domain has a non-canonical neck structure that potentially mediates protein-protein interactions. The kinesin-1 coiled-coil domain was fused to NOD485 for dimerization and used in this study to dissect NOD motility.

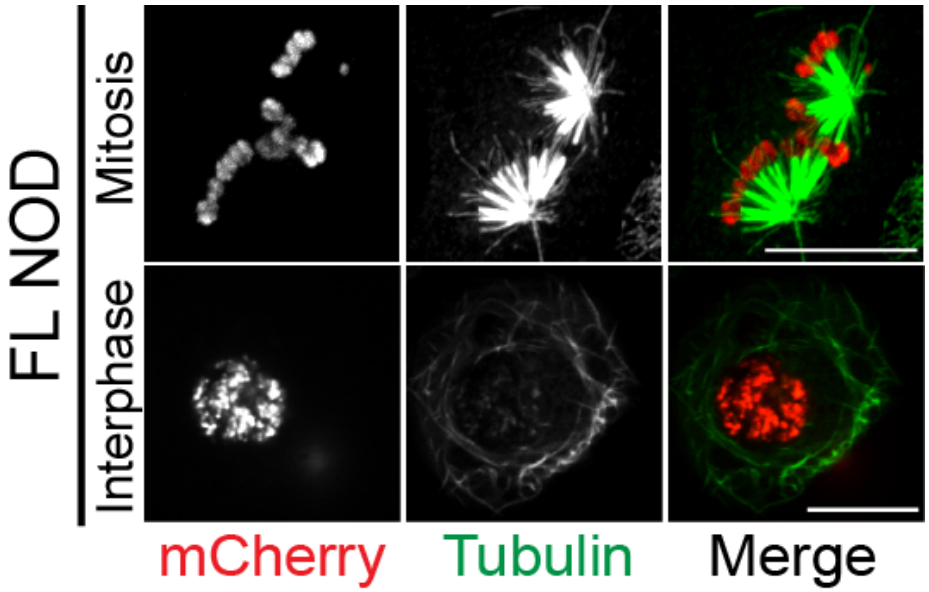

Figure 3. 2. Full length NOD localization.
Maximum projections of two color spinning disk confocal images showing the chromosomal localization of FL NOD over-expressed in *Drosophila* S2 cells. NOD is shown in red and microtubules are in green. Scale bar 10μm

Most N-terminal motor domain-containing kinesins possess a neck linker and a well-defined neck coiled-coil downstream of their motor domains; however, some kinesins, including NOD, have non-canonical neck regions that contribute to their functions in cells (Davies et al., 2015). We next generated cells expressing a longer truncation of NOD (1-485) that encompasses the motor domain and the non-canonical neck extension region. Addition of the neck extension conferred MT-binding activity in cells as NOD485 uniformly coated MTs throughout the cell cycle (Fig. 3.3). The addition of the non-conventional extension could promote MT binding through numerous non-exclusive mechanisms including the introduction of a second MT binding site, which has been shown for hKID (Shiroguchi et al., 2003), post-translational modifications, association with regulatory factors, or dimerization through the low probability

coiled-coil. While associated with MTs in living cells, the MT localization of NOD485 was significantly reduced upon fixation conditions leading us to believe that the interaction, while stronger than NOD324, may be relatively low affinity (Table 3.1). Nonetheless, the localization of NOD485 led us to reason that the oligomeric state of NOD warranted further investigation. We noted that several structural and functional aspects of NOD are reminiscent of the monomeric plus-end directed kinesin Unc104/KIF1A. First, kinesin-10 family members have been shown to exist as monomers *in vitro* (Shiroguchi et al., 2003), and, both NOD and Unc104/KIF1A possess low-probability/weak coiled-coil regions adjacent to their N-terminal motors while their C-termini contain domains cluster the motors on the surface of cargos: chromosomes and synaptic vesicles respectively (Klopfenstein et al., 2002; Klopfenstein and Vale, 2004). Prior work on Unc104 demonstrated that constitutive dimerization of the Unc104 motor domain and its adjacent "weak" coiled-coil converted the monomer into a processive, plus-end directed motor with physiological velocities (Tomishige et al., 2002). Thus, we utilized a comparable approach as that applied to Unc104, specifically fusion to the kinesin-1 "stalk" (strong) coiled-coil (CC), to examine how dimerization of the NOD motor domain affected its behavior (Fig. 1A).

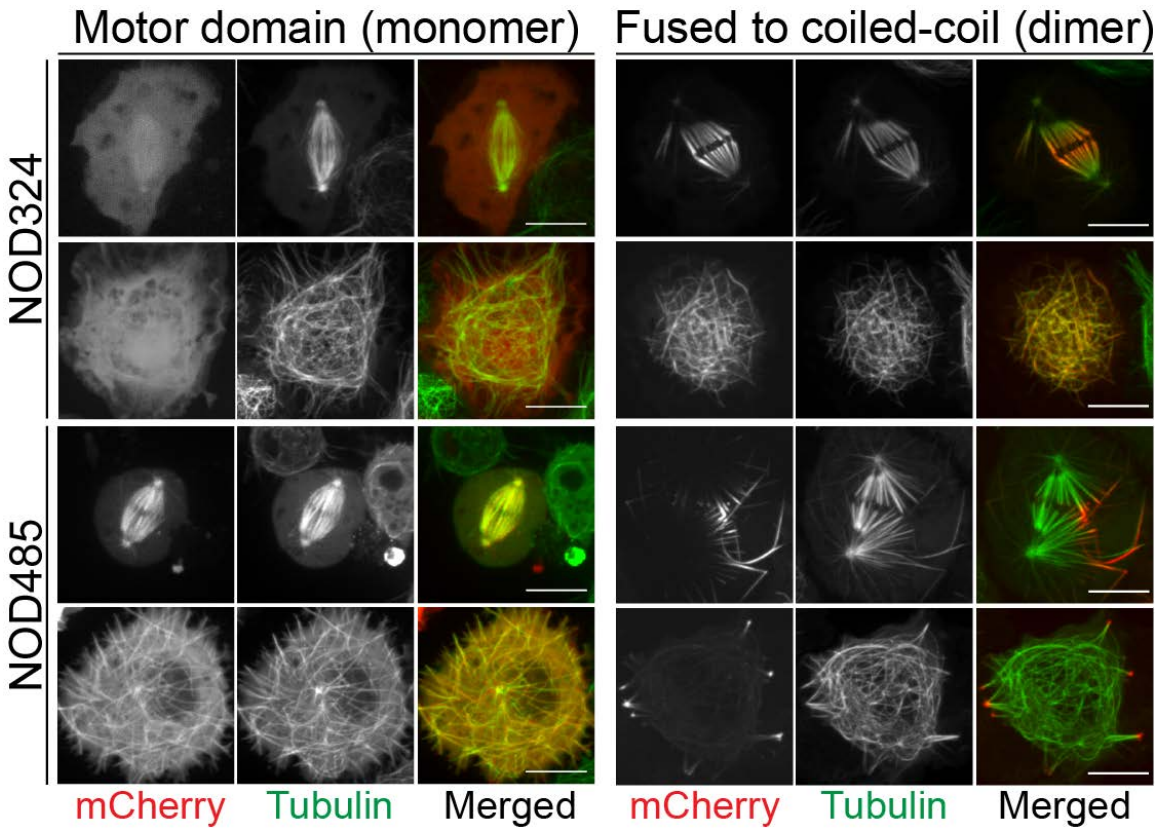

Figure 3.3. Localization of the different truncated NOD proteins.
Two-color confocal images of *Drosophila* S2 cells expressing GFP-tubulin (green) and NOD-mCherry (red). The motor domain, NOD324, alone does not bind to MTs in interphase or mitosis. When forced to dimerize, NOD324 equally coats all MTs. NOD485 has the downstream coiled-coil region, which has been classified as non-canonical neck structure. In contrary to NOD324, NOD485 monomers bind to MTs, and when dimerized, they stabilize and bundle MTs, and more prominently found at MT plus-ends. Scale bare are 5μm

The motor domain alone (1-324) was first dimerized. NOD324CC evenly coated interphase MTs and robustly associated with spindle MTs during mitosis, exhibiting a slight enrichment toward the plus-ends of kinetochore fibers in the vicinity of aligned chromosomes with some evident MT bundling (Fig 3.3). We next generated cells expressing dimerized NOD485 and, while NOD485 localized uniformly to MTs, NOD485CC exhibited a striking localization pattern in which it became highly enriched near MT plus-ends throughout mitosis and interphase. Interestingly, NOD485CC was nearly void from MTs in the vicinity of spindle poles suggestive of some form of spatial regulation of NOD localization and/or activities. Significant MT bundling was also observed throughout the cell cycle especially in cells with high levels of NOD485CC expression, which was not observed in the NOD485-expressing cells (Fig. 3.3). The localization patterns and behavior of the dimerized NOD truncations were not attributable to the kinesin-1 coiled coil since CC-mCherry only weakly associated with a subset of MTs in some cells and exhibited no obvious or consistent localization pattern or evident activity. Furthermore, the neck extension region, while necessary, was not sufficient for MT binding as the localization patterns of NOD325-485 and NOD325-485CC were identical to mCherry (diffuse with some haziness in the vicinity of spindles) or CC-mCherry respectively (Table 3.1).

Table 3.1. Summary of NOD localizations and activities.

	MT Association	Plus-end directed motility	Plus-end tracking
NOD324	-	-	-
NOD324CC	++	-	-
NOD485	+	-	-
NOD485CC	++	+	+
NOD325-485	-	-	-
NOD325-485-CC	+/-	-	-
Kinesin-1 Coiled-Coil	+/-	-	-

*CC = Kinesin-1 coiled-coil domain
+ weak association
++ strong association
- not observed
Note: Classifications were normally determined by live cell imaging; however, MT association of NOD485 was designated as weaker (+) because it was not retained after fixation with paraformaldehyde and permeabilization with detergent during preparations for immunofluorescence while the NOD324CC and NOD485CC were.

The localization pattern of NOD485CC suggested that the dimerized motor could possess MT plus-end directed motility in cells. This possibility was more closely examined by imaging cells using total internal reflection fluorescence (TIRF) microscopy to exclusively visualize the population of NOD molecules on the MTs closest to the cell cortex (Fig 3.4). Puncta of both NOD485 and NOD324CC were visible on MTs, but motility was not evident (Table 3.1). The behavior of NOD485CC was markedly different from the other truncations as NOD puncta were clearly observed moving processively on MTs toward the cell periphery (Fig. 3.5). Measurements of motile NOD485CC puncta in cells yielded an average velocity of 8.70 +/- 3.61 μm/min [note: mean +/- SD is reported for all motility measurements] (Fig. 3.5 bottom). These data demonstrate that

dimerization of the NOD motor domain alone (NOD324CC) promotes MT binding but not motility, most likely because it lacks a functional neck linker, which plays an important role in coordinating motor head functions (Vale and Milligan, 2000), whereas dimerization of the motor domain and non-conventional neck extension region converts NOD into a directional motor.

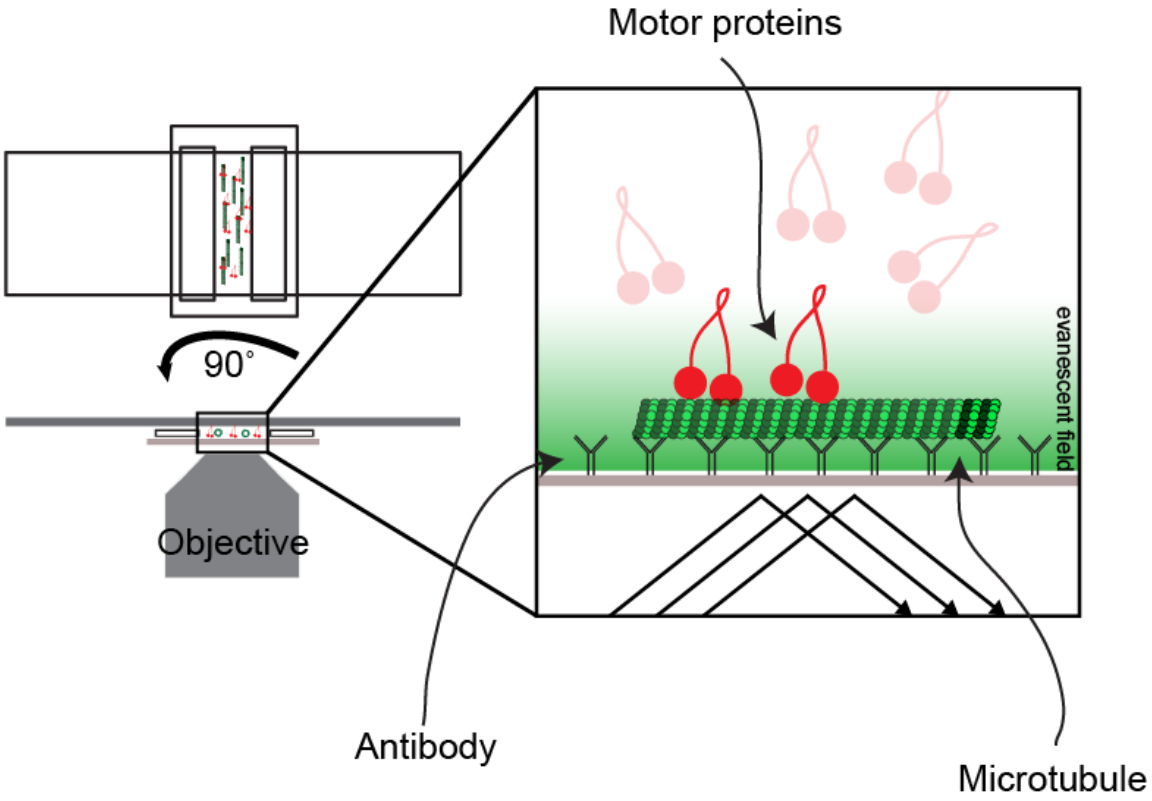

Figure 3.4. Total internal reflection fluorescent (TIRF) microscopy.
TIRF microscopy is a technique developed to image single molecules very close to the coverslip. The excitation light is 100% reflected at the coverslip, so that only a small amount of energy, also known as the evanescent energy is exciting fluorophores within 200nm of the coverslip. This technique allows for imaging single molecules with minimal background noise.

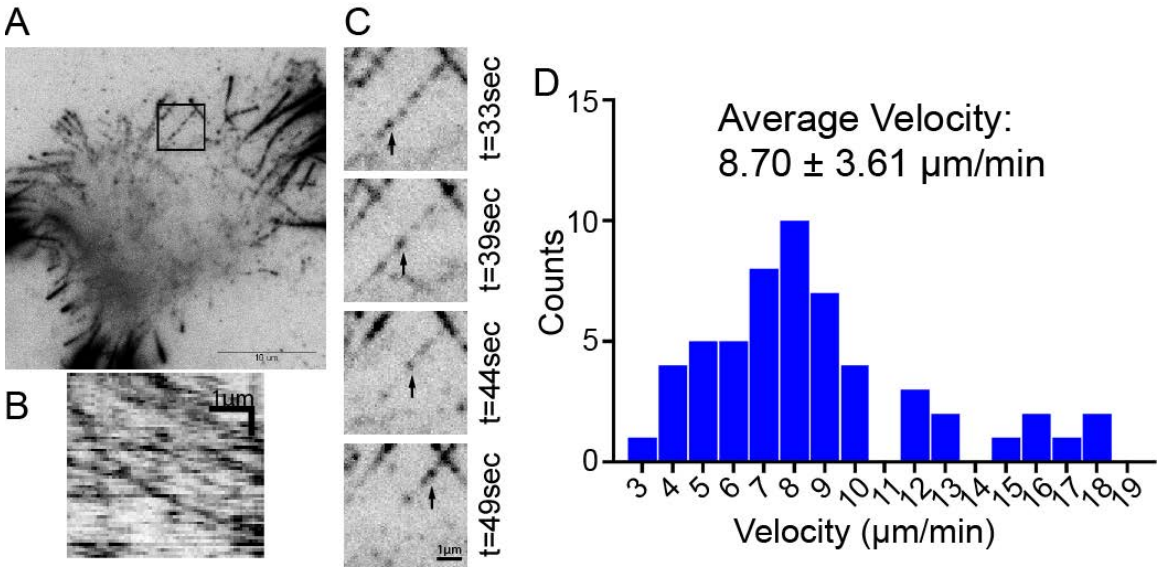

Figure 3.5 Dimerized NOD485 is motile in cells.
(A) Image of a whole cell expressing NOD485CC-mCherry in TIRF. (B) Kymograph of a NOD485CC molecule walking towards the cell periphery. (C) Zoomed in of the region highlighted in (A), still frames of timelapse TIRF imaging. The arrow points to a NOD485CC molecule walking towards the cell periphery. (D) Histogram of the velocity distribution of NOD485CC molecules walking in cells, with an average velocity of 8.7μm/min in cells, n = 55 molecules. Scale bars, 10μm in (A) and 1μm in (B) and (C).

To further characterize NOD motility *in vitro*, we applied TIRF-based imaging to cell extracts (Cai et al., 2007; Mann et al., 2017) in which the only fluorescently tagged protein was NOD485CC. Using this technique NOD motility could still be studied in near physiological conditions, but in a chamber in which the state of the MTs, which are attached to the cover-glass, as well as the buffering conditions can be tightly controlled. In cell lysates prepared from NOD485CC-expressing cells, NOD puncta were observed to walk unidirectionally along taxol stabilized MTs (Fig. 3.6). The mean velocity of 8.62 +/- 2.32 μm/min measured for motile NOD485CC molecules in the cell lysates was indistinguishable from measurements made from TIRF microscopy of living cells (Fig. 3.6). Dimerized NOD is a processive motor as it exhibited a mean run length of 1.49 +/- 0.66 μm

(Fig. 3.6), comparable to conventional kinesin (Friedman and Vale, 1999). NOD motility was ATP dependent since the addition of the non-hydrolysable ATP analogue, AMPPNP to cell lysates resulted in non-motile NOD485CC puncta on MTs (Fig. 3.6). Live-cell observations strongly suggested that NOD is a plus-end directed motor because NOD485CC puncta often moved toward the cell periphery where the MT plus-ends are typically oriented during interphase. To directly test if NOD485CC walks toward MT plus-ends, purified GFP-labeled human kinesin-1 (Kif5B) motor, a plus-end directed motor, was added to lysates from NOD485CC-mCherry expressing cells. NOD485CC and kinesin-1 walked in the same direction, establishing that NOD is a plus-end directed motor (Fig. 3.7).

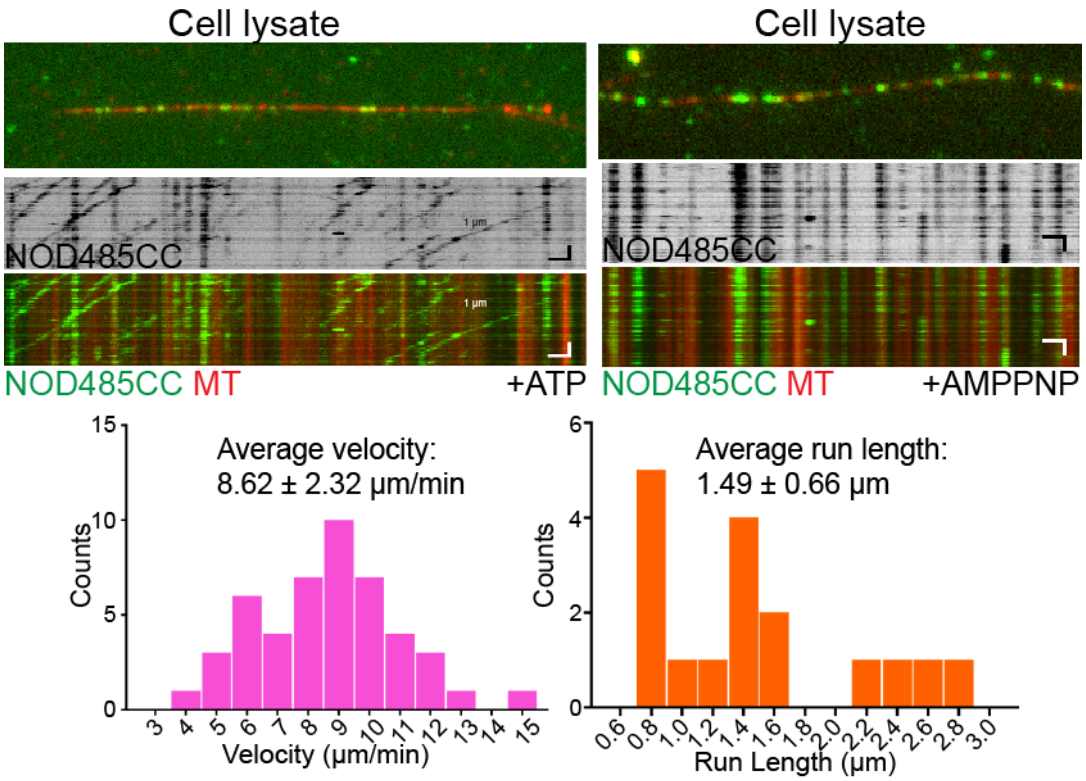

Figure 3.6. NOD485CC-mCherry cell extract is motile in *in vitro* TIRF assay. TIRF images of MT (red) and NOD485CC-EGFP (green) in the presence of ATP (left) or non-hydrolysable ATP analogue, AMPPNP (right). Kymograph of NOD485CC molecules walk unidirectionally on the MT in the presence of ATP, but are static in AMPPNP. Histogram of the velocity distribution of single NOD485CC-mCherry molecules, with an average of 8.62µm/min, with an average run length of 1.49µm. n=47 molecules. Scale bar, 1µm horizontal, 10sec vertical.

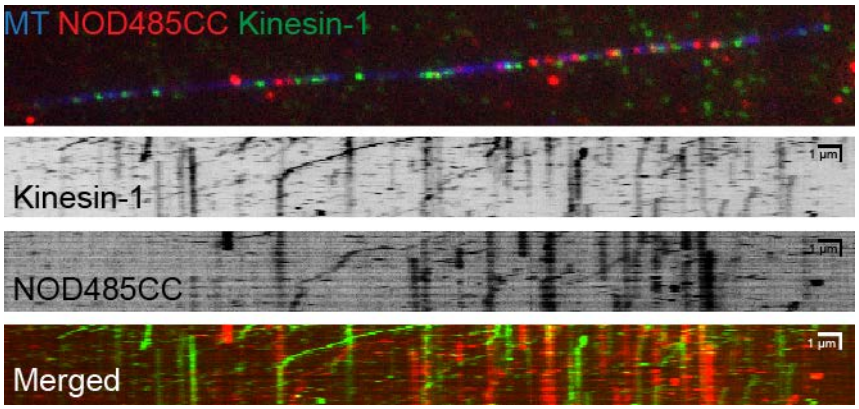

Figure 3.7. NOD is a plus-end directed motor.
To determine the directionality of the NOD motor, purified Kinesin-1 motor, K560-GFP (green), a well characterized plus-end directed motor was added to the same chamber as NOD485CC-mCherry (red). The kymographs show that NOD485CC and kinesin-1 are walking towards the same direction, thus NOD is a plus-end directed motor. Scale bar, 1μm horizontal, 10sec vertical.

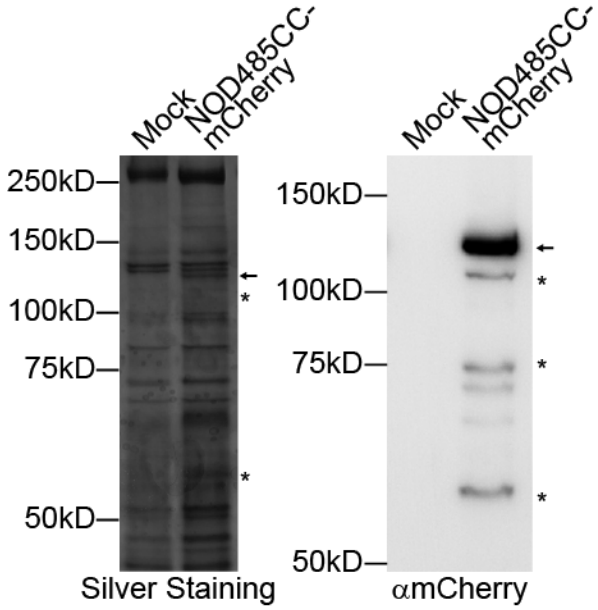

Figure 3.8. NOD485CC-mCherry-STREP purification.
Silver staining and western blot of NOD485CC-mCherry-STREP purification, compared to mock purification with WT cells. Silver staining of the SDS-PAGE gel revealed background bands with the same pattern as the mock purification, suggesting other biotinylated proteins are binding to the bead. A unique band only in the NOD purification is present at the expected size of ~110kD (arrow), while two other bands are potential degradation products (asterisks). Western blot analysis was done to further confirm NOD485CC-mCherry-STREP purification using a mCherry antibody.

NOD motility has never been reconstituted *in vitro* and, like others, we were unable to purify active NOD485CC from bacteria. Furthermore, NOD485CC activity in S2 cell lysates was labile and sensitive to buffer conditions. Thus, NOD485CC-mCherry was purified from *Drosophila* S2 cells using a C-terminal Strep-tag® that allows for affinity purification on a streptavidin-based matrix and gentle elution using biotin-containing buffers to better preserve protein activity. Silver staining of the purification revealed a unique band, when compared to a mock purification from wild type cell extracts, at the predicted size of NOD485CC-mCherry (~110 kDa), which was confirmed by western blot using an mCherry antibody (Fig. 3.8). While it is probable that NOD-associated proteins were co-purified in the preparation, the majority of background bands were likely biotinylated *Drosophila* proteins since a nearly identical banding pattern was observed in mock purifications from wild type cell extracts (Fig. 3.8). In TIRF assays the affinity purified NOD485CC-mCherry clearly exhibited ATP-dependent, unidirectional motility, although the mean velocity of 5.79 +/- 1.56 μm/min was somewhat slower than in cells and cell extracts while the average run length of 3.45 +/- 1.72 μm was longer than that measured in cell extracts (Fig. 3.9). The slower velocity of purified NOD485CC suggests that it may be in sub-optimal conditions when completely removed from a cytosolic environment consistent with our observations that the activity is labile. Nonetheless, the data in cells and *in vitro* consistently demonstrate that dimerized NOD is a processive, plus-end directed motor with velocities similar to those measured for Xkid and hKID (Bieling et al., 2010; Brouhard and Hunt, 2005; Yajima et al., 2003).

Furthermore, the measured velocities and run lengths for NOD485CC are nearly identical to the characteristics of chromatin stretching events that walked toward plus-ends in NOD-FL over-expressing cells supporting the conclusion that these events were revealing of MT plus-end directed motility by chromatin-bound NOD (Cane et al., 2013).

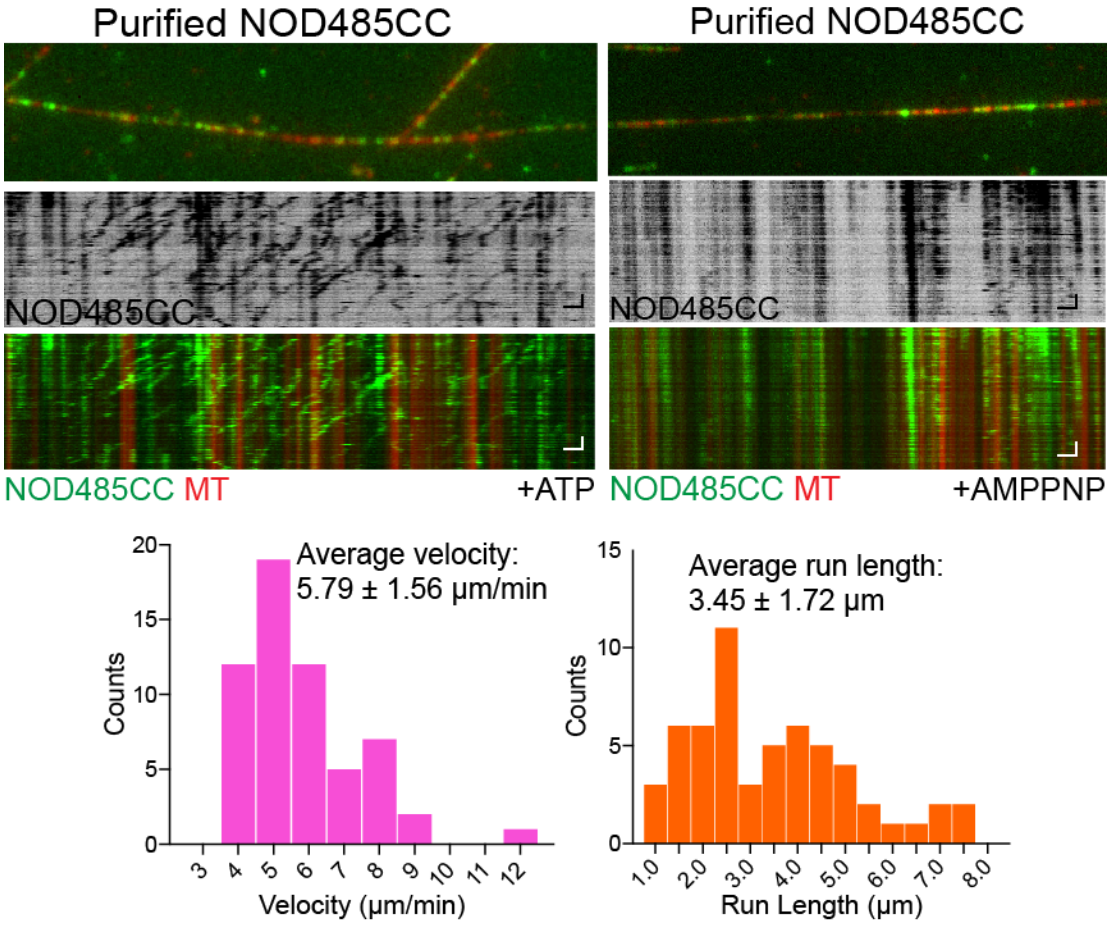

Figure 3.9. NOD485CC purified from *Drosophila* cells also possess motility. NOD485CC molecules purified from *Drosophila* cells have slower average velocity than molecules in cell extract, further supporting that NOD is a very labile molecule and sensitive to the buffer conditions. TIRF image of a MT (red) with purified NOD485CC-EGFP (green) in a chamber in ATP or AMPPNP. Kymograph of NOD485CC molecules walking unidirectionally on the MT. Histograms of the velocity distribution of NOD485CC molecules, with an average of 5.79µm/min and the average run length of 1.49µm. n=58 molecules. Scale bar, 1µm horizontal, 10sec vertical.

It is conceivable that dimerizing NOD485 by introducing the kinesin-1 CC could produce motile heterodimers that are not physiologically relevant. While NOD-mCherry, kinesin-1-GFP heterodimers were not evident when purified kinesin-1-GFP was added to NOD485CC extracts (Fig. 3.7), we wanted to further rule out this possibility by fusing rapamycin-inducible dimerization domains to NOD485. First, cell lines co-expressing dark (no fluorescent tag) NOD485-FRB and NOD485-FKBP-EGFP were generated (Fig. 3.10). Like NOD485, NOD485-FKBP-EGFP localized uniformly to MTs in the absence of rapamycin, but upon addition of 100 nM rapamycin to the media motile puncta of NOD485-FKBP-EGFP could be observed moving on MTs toward the cell periphery as was observed for NOD485CC (Fig. 3.11). Extracts were next prepared from NOD485-FKBP-EGFP, NOD485-FRB-expressing cells to visualize NOD on MTs by TIRF *in vitro*. Without rapamycin, non-motile puncta of NOD485-FKBP-EGFP associated with MTs (Fig. 3.12). However, unidirectional motility of NOD485-FKBP-EGFP puncta was achieved within minutes of adding 100 nM rapamycin to the same cell extracts that did not exhibit motility in the absence of rapamycin (Fig. 3.12). We next generated cell lines co-expressing NOD485-FKBP-EGFP and NOD485-FRB-mCherry (Fig. 3.13). In cells without rapamycin the mCherry and EGFP-tagged NODs uniformly coated the MTs similar to NOD485, but NOD localization changed quickly upon addition of 100 nM rapamycin as EGFP- and mCherry-tagged, chemically dimerized NOD485 accumulated toward MT plus-ends at the cell periphery similar to NOD485CC (Fig. 3.13). To further bolster the

conclusion that dimerization of NOD485 promotes its motility, we performed TIRF microscopy on lysates prepared from cells expressing NOD485-FKBP-EGFP and NOD485-FRB-mCherry. In agreement with prior observations, motile NOD485 puncta containing EGFP and mCherry were observed to move directionally on MTs (Fig. 3.14). Quantification of motile, rapamycin-induced NOD485 dimers from TIRF-based assays yielded an average mean velocity of 7.87 +/- 2.14 μm/min and a mean run length of 1.87 +/- 0.58 um (Fig. 3.14), which are comparable to the properties measured for NOD485CC motility in cells and lysates. Altogether, the data support the conclusion that multiple modes of NOD485 dimerization can support directional motility and that constitutive dimerization with the kinesin-1 CC did not produce artefactual NOD motility.

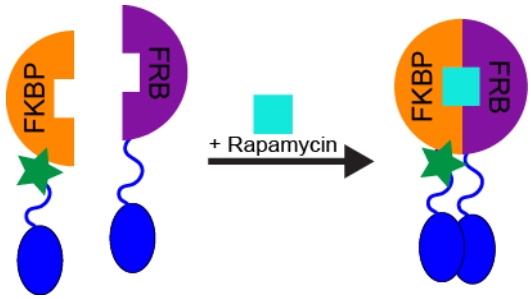

Figure 3.10. Schematic of a rapamycin dimerization system.
Schematic of a chemically induced NOD dimers. NOD485-FKBP-EGFP and NOD485-FRB (no fluorophore) is expressed in *Drosophila* cells to rule out that the dimerization through kinesin-1 coiled-coil domain is creating NOD heterodimers with other kinesins.

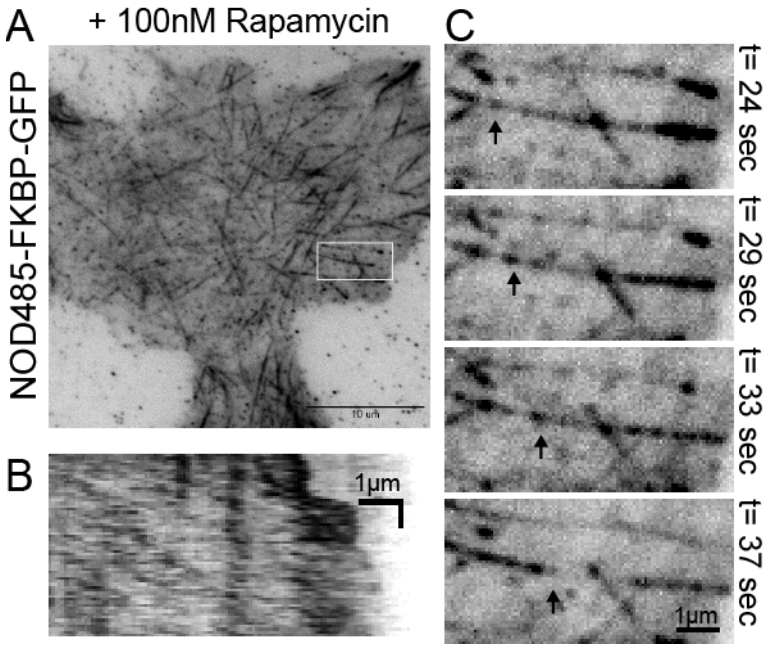

Figure 3.11. Rapamycin dimerized NOD485 also possesses motility in cells. (A) Image of a whole cell expressing NOD485-FKBP-EGFP and NOD485-FRB-mCherry in the presence of 100nM rapamycin in TIRF. (B) Kymograph of a NOD485-FKBP-EGFP molecule walking towards the cell periphery. (C) Zoomed in of the region highlighted in white box in (A), still frames of timelapse TIRF imaging. The arrow points to a NOD485-FKBP-EGFP molecule walking towards the cell periphery. Scale bars, 10µm in (A) and 1µm in (B) and (C).

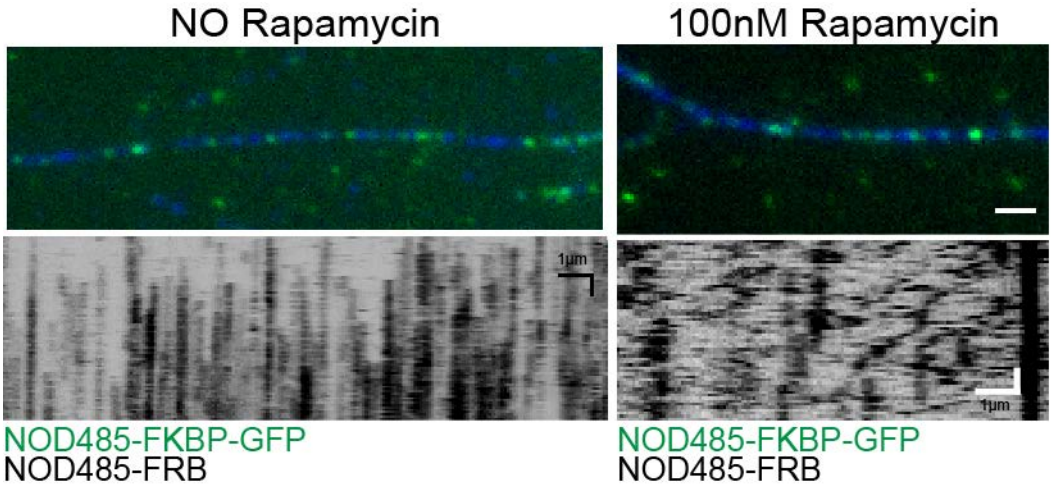

Figure 3.12. Rapamycin dimerized NOD485 has similar properties as NOD485CC.

In vitro TIRF assay using cell extract expressing NOD485-FKBP-EGFP and NOD485-FRB. In the absence of rapamycin, NOD molecules bind to the taxol stabilized MT, and even accumulate overtime, but are not motile. In the presence of 100nM rapamycin, molecules are seen walking unidiretionally.

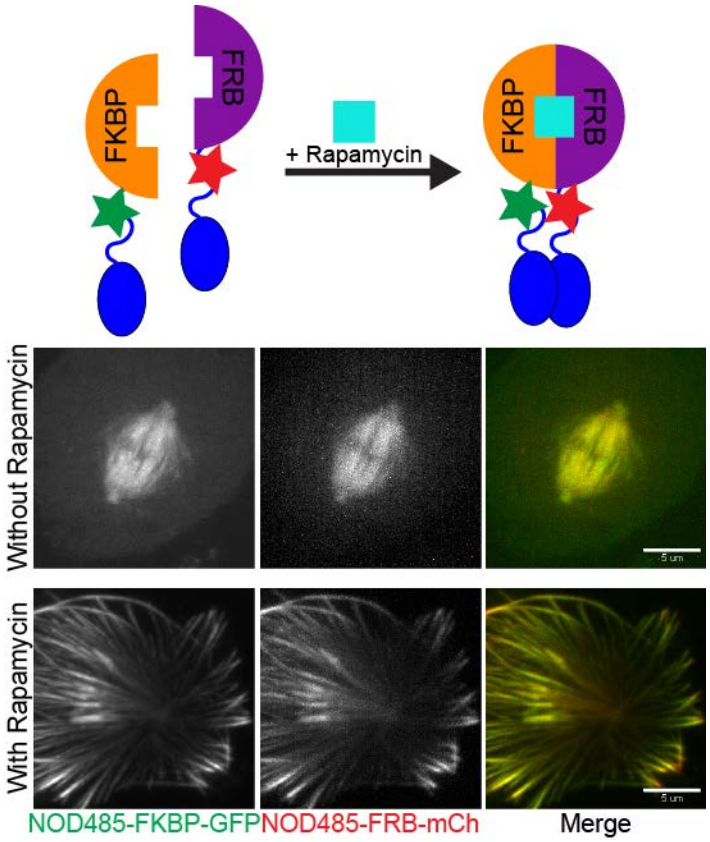

Figure 3.13. Rapamycin dimerized NOD485 localization is similar to NOD485CC.

Schematic of the rapamycin induced dimerization system used in this study. In the presence of 100nM rapamycin, NOD485 dimerizes through the FKBP and FRB domains, tagged with GFP and mCherry, respectively. Representative images of cells expressing NOD485-FKBP-EGFP and NOD485-FRB-mCherry in the absence (top) and presence (bottom) of rapamycin. Cells treated with 100nM rapamycin have similar localization patter to NOD485CC, where dimerized NOD485 is absent from the spindle poles, starts to accumulate at MT tips, stabilizes and bundles MTs. Scale bar 5μm.

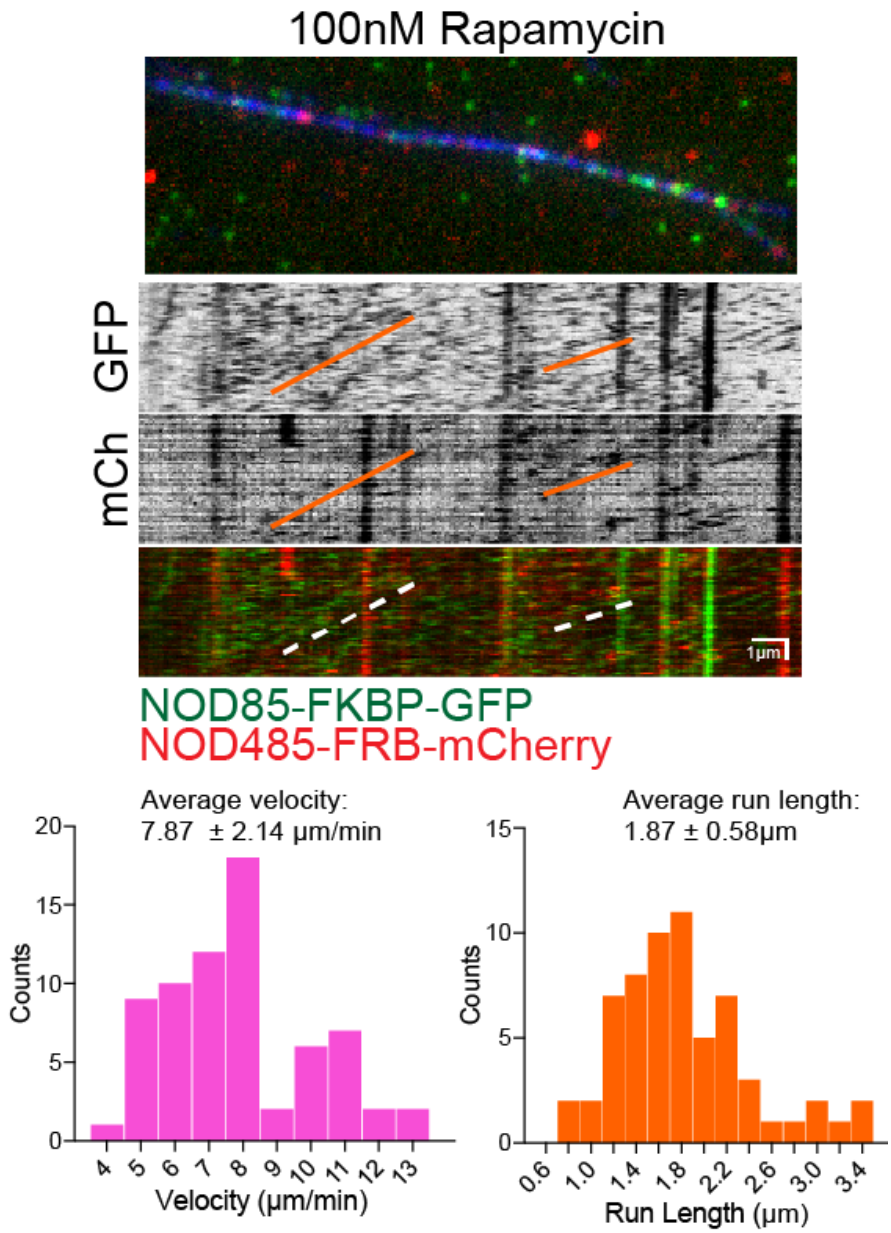

Figure 3.14. NOD485-FKBP-EGFP and NOD485-FRB-mCherry colocalize in *in vitro* TIRF assays.

TIRF assays using extract prepared from cells co-expressing NOD485FKBP-EGFP and NOD485-FRB-mCherry. In the presence of 100nM rapamycin molecules are observed walking on the MTs. Yellow lines are positioned below tracks to highlight co-localized, motile NOD485-FKBP-EGFP and NOD485-FRB-mCherry puncta. Histogram of the velocities of rapamycin-dimerized NOD485 molecules from TIRF assays using cell lysates, with an average velocity of 7.87 ± 2.14 μm/min, n = 69. Histogram of run lengths of rapamycin-dimerized NOD485 in TIRF assays, with an average run length of 1.87 ± 0.58 μm. Scale bar is 1μm in. Vertical scale bar is 10 secs. Mean ± SD

Consistent with the end-tracking hypothesis of NOD-based force production (Cochran et al., 2009; Cui et al., 2005), prior work from our group characterized NOD-coated chromatin stretch events that co-localized with EB1 comets as well as occasional cytoplasmic NOD fragments that tracked polymerizing and depolymerizing MT plus-ends (Cane et al., 2013). Spinning disk confocal imaging of cells co-expressing NOD485CC-EGFP and EB1-TagRFP-T revealed that NOD485CC often co-localized with EB1 tracks on MT plus-ends (Fig. 3.15). It is noteworthy that NOD remained associated with depolymerizing MTs through a mechanism that is presently unclear but that could be similar to the bi-directional tracking activity of CENP-E since hKID possesses a low affinity, but conserved, MT binding region outside of its motor domain (Gudimchuk et al., 2013a; Shiroguchi et al., 2003). Plus-end directed NOD485CC puncta were evident behind the tip-tracking NOD population in kymographs from NOD485CC-, EB1-expressing cells (Fig. 3.15) establishing that NOD485CC also exhibited plus-end directed motility in mitosis. The observed co-localization of NOD and EB1 led us to next test if NOD and EB1 directly interact in pulldown assays using purified components. Indeed, GST-EB1-TagRFP-T pulled down with MBP-NOD485CC-EGFP, but not the MBP-EGFP control protein (Fig. 3.16).

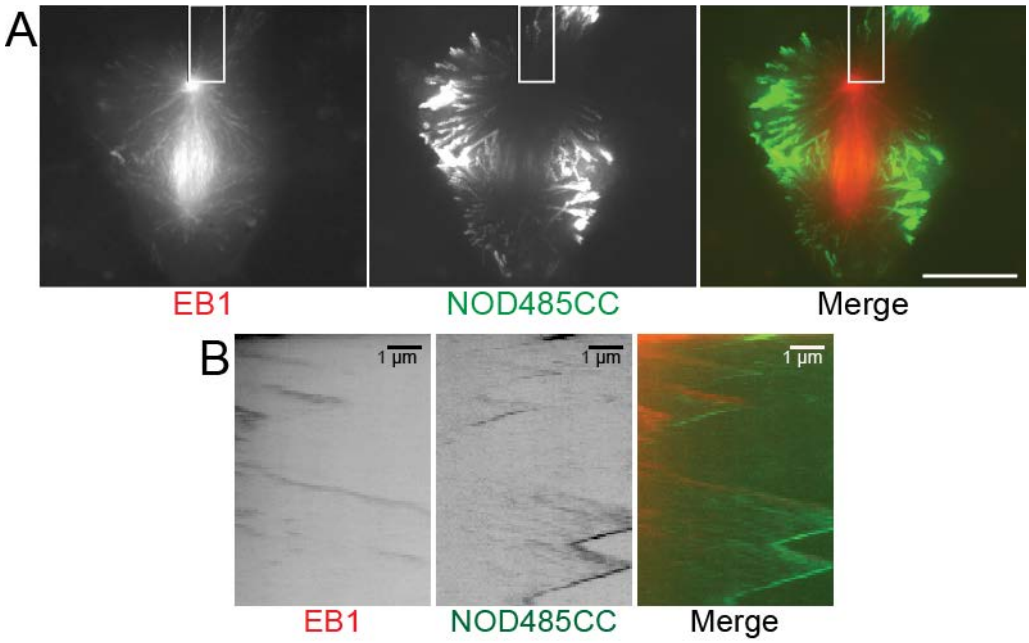

Figure 3.15. NOD485CC tracks growing and shrinking MTs.
(A) Maximum intensity projection of a cell expressing EB1-TagRFP-T (red) and NOD485-EGFP (green). Dimerized NOD485 localizes to the MT plus-ends in mitosis, where it potentially stabilizes and bundles microtubules. (B) Kymograph of a dynamic astral MT from the highlighted white box from (A). EB1 only associates with polymerizing MTs, while NOD colocalizes with EB1 at the tips of a growing MT, but it's capable of hanging on to the depolymerizing MT.

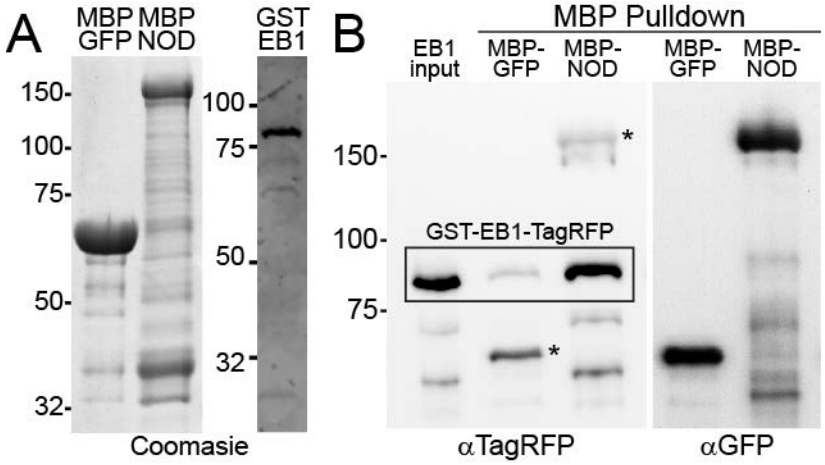

Figure 3.16. NOD485CC interacts with EB1.
Western blot of the pulldown assay using purified proteins. GST-EB1-TagRFP-T was incubated with MBP-NOD485CC-EGFP and MBP-EGFP, as control, and pulled out using magnetic amylose beads. Samples were analyzed by western blot with αTagRFP-T and αGFP antibodies. Asterisks mark the antibody cross reaction with MBP-EGFP (72kD) and MBP-NOD-EGFP (150kD).

To further characterize the NOD-EB1 interaction we turned our attention to amino acids 325-485 since NOD485CC exhibited MT plus-end tracking activity and NOD324CC did not. In looking closely at the amino acid sequence we noticed that NOD contains multiple disordered regions, centered around Proline (P) and Threonine (T) residues between residues 430-480, that looked similar to unconventional EB1-binding motifs recently identified in fungal species in the *S. cerevisiae* Kar9 motor and *S. pombe* Dis1/Tog MAP (Manatschal et al., 2016; Matsuo et al., 2016). Thus, we focused on the disordered regions, which we deemed “PT” motifs, using SPOT peptide arrays spanning residues 400-485, generating 15 amino acid peptides with an offset of 2 residues, and using a previously identified “perfect” SxIP aptamer as a positive control peptide (Leśniewska et al., 2014). The peptides exhibiting the strongest association with purified *Drosophila* EB1-TagRFP-T centered on the two so-called PT motifs (PT motif-1 and -2) we had speculated could bind EB1 (Fig. 3.17). The amino acids surrounding SxIP motifs significantly impact their affinities for EB1 (Jiang et al., 2012b; Leśniewska et al., 2014). To determine which PT-flanking amino acids contributed to EB1 binding, the two peptides that exhibited the strongest association with EB1 on the SPOT array were subjected to alanine scanning (Fig. 3.18). In each peptide, mutation of a surrounding arginine (R) residue ~3-6 amino acids upstream or downstream of the PT sequence eliminated EB1 binding. The results suggest that, like the SxIP motif, neighboring basic residues increase the affinity of PT motifs for EB1. However, the results of our mutational analyses differed from alanine scanning of the fungal PT motifs. While a slight

reduction in EB1 binding may have resulted from mutating the P, T, and some nearby hydrophobic residues, prior studies reported major reduction/loss of EB1 binding when the Proline or neighboring hydrophobic residues were mutated (Manatschal et al., 2016; Matsuo et al., 2016). During the preparation of this manuscript a study was published that extensively analyzed the unconventional Ka9-EB1-interaction designating this novel EB1 binding motif the LxxPTPh motif (Kumar et al., 2017b). While the PT motifs in NOD certainly resemble the LxxPTPh motif, the compositional differences could indicate that the *Drosophila* EB1-PT motif interaction may be slightly divergent and/or that significant variability in this new motif can still support EB1 interactions, as suggested by the composition of the Dis1/Tog motif (Matsuo et al., 2016).

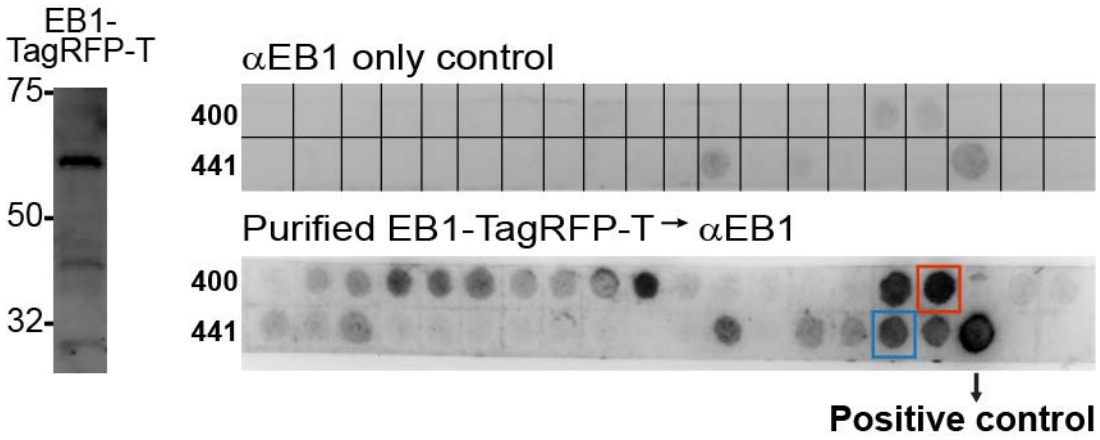

Figure 3.17. "PT" sequence motifs interact with purified EB1.
Coomasie staine SDS-PAGE gel showing the purified EB1-TagRFP-T used to probe the SPOT peptide arrays. SPOT peptide arrays of NOD 400-485 and a "perfect" SxIP peptide as a positive control, were probed with with anti-EB1 serum (control) or purified EB1-TagRFP-T followed by incubation with the anti-EB1 serum. Two peptides with positive EB1 binding are highlighted in red (PT motif-1) and blue (PT motif-2), were subjected to further analysis.

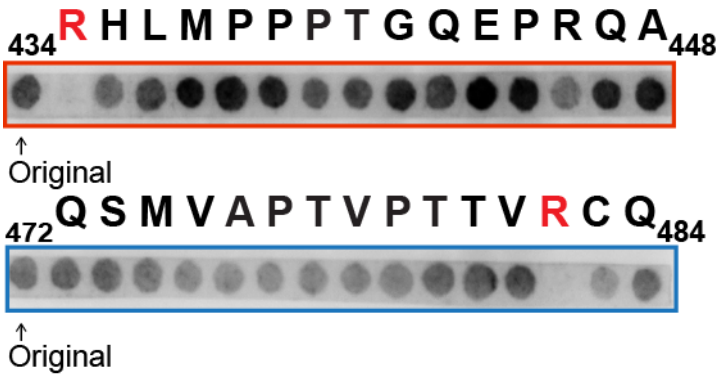

Figure 3.18. Alanine scan of the two "PT" motifs.
To determine the importance of the surrounding region for EB1 interaction, each amino acid was mutated to alanine. Arginine at positions 434 and 482 are absolutely required for EB1 binding.

We next employed microscale thermophoresis (MST) to measure the binding affinity of the NOD PT-motif 1 for EB1. The N-terminus of either the PT-motif 1 or a bona-fide "perfect" SxIP peptide (positive control) was labeled with fluorescein (FITC) dye and the movement of each fluorescently labeled peptide (fixed at 50 nM) in a temperature gradient was measured by MST while varying concentrations of unlabeled *Drosophila* GST-EB1 (Fig. 3.19). The binding affinity measured by MST for the SxIP motif was 807 nM, which is relatively close to the K_d (~570nM) measured by isothermal titration calorimetry using the "perfect" SxIP peptide and human EB1. Interestingly, the affinity of the PT motif-1 for *Drosophila* EB1 was measured to be 725 nM - slightly higher than the K_d of the positive control aptamer (Fig. 3.20), comparable to other bona-fide SxIP motifs, and higher than affinities measured for EB1-CAP-Gly interactions (Weisbrich et al., 2007). Thus, the NOD PT motif-1 exhibits a physiologically relevant affinity for *Drosophila* EB1 that is comparable or greater to the affinities of the two previously identified EB1-binding modules: SxIP motifs and CAP-Gly domains.

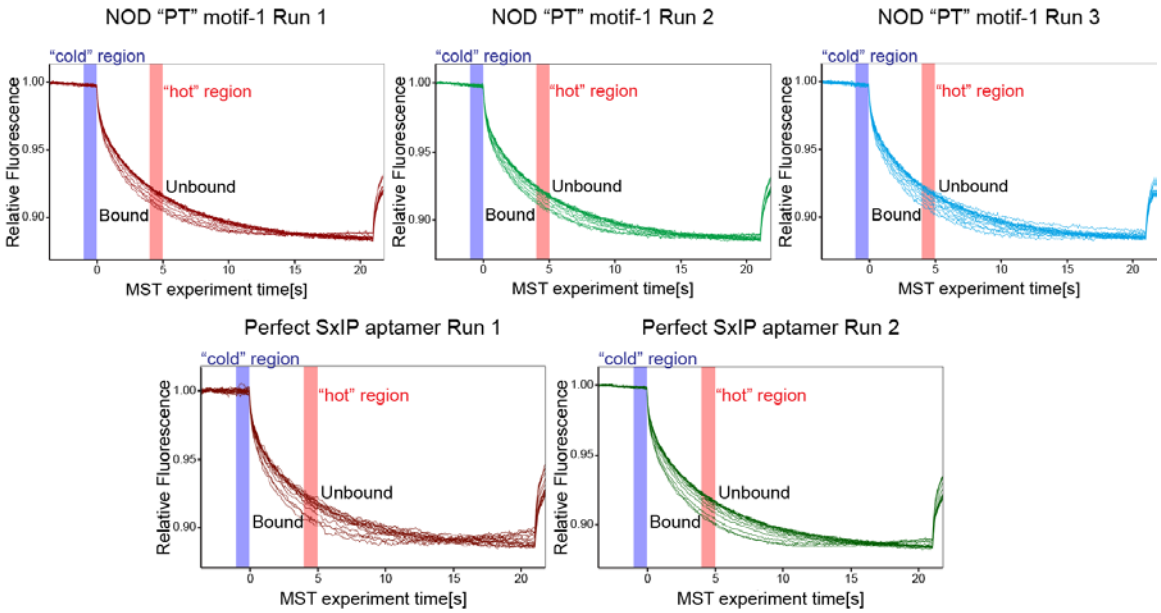

Figure 3.19. Raw data of microscale thermophoresis measurements. Graphs plotting the raw data of each MST measurement. The blue area highlights the "cold" region at time = 0 and the red area highlights the "hot" region at time = 5sec. F_{norm} represents the change in fluorescence at 5 secs that was used to calculate ΔF_{norm} in Fig 3.19.

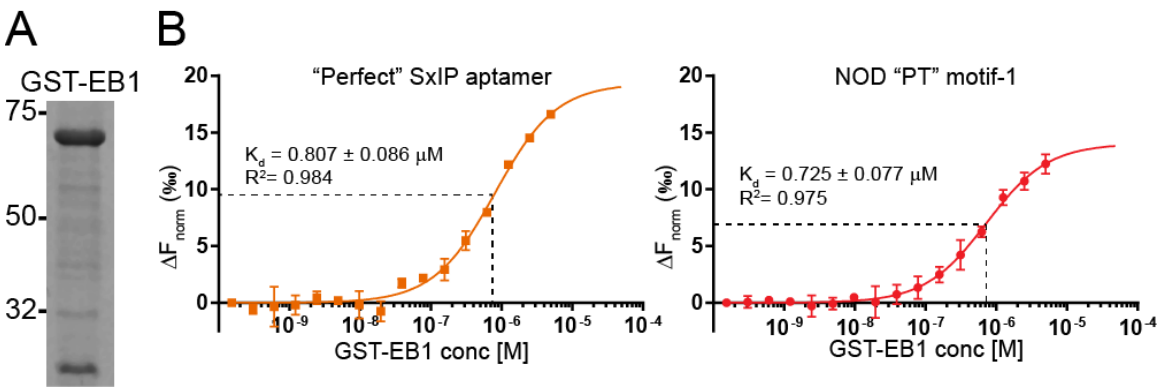

Figure 3.20. NOD interacts with EB1 via a new microtubule tip localization sequence.

(A) Coomassie stained SDS-PAGE gel showing the purified *Drosophila* GST-EB1 used in microscale thermophoresis (MST). (B) Microscale thermophoresis (MST) was done by titrating GST-EB1 while maintaining a constant concentrations of fluorescein (FITC)-labeled "perfect" SxIP aptamer (left) or NOD "PT" motif-1 (right) resulting in measurable changes in the fluorescence signal within a temperature gradient that can be used to calculate dissociation constants (SxIP K_d = 807 ± 86 nM and NOD PT motif-1 K_d = 725 ± 77 nM). Error bars represent standard deviation of n = 3 (PT motif-1) and 2 (SxIP motif) MST runs. The K_d values are reported as mean ± SEM.

3.3 Discussion

How the *Drosophila* kinesin-10 NOD generates PEFs has long been a mystery. Prior work (Cane et al., 2013) led us to hypothesize that NOD possesses two force producing activities: 1) MT plus-end directed motility, which had never been directly demonstrated, and 2) end-tracking on polymerizing MTs, the mechanism of which was entirely speculative. We demonstrate here, for the first time, that dimerized NOD exhibits plus-end directed motility in cells and *in vitro* and that NOD directly interacts with the master tip-tracking protein EB1 via a new type of conserved MT tip localization sequence (Fig. 5). It is noteworthy that both MT polymerization and motor activity were originally proposed as sources of the PEF when the phenomenon was first described (Rieder et al., 1986), >30 years later our findings reveal NOD as a molecular nexus of both force-producing mechanisms.

We propose that dimerization of NOD activates plus-end directed motility by bringing two alpha-helices from the non-conventional neck region, which normally have a low probability of forming a coiled-coil, into close enough proximity to support productive motor head dimerization similar to a mechanism proposed for Unc104 regulation (Al-Bassam et al., 2003). The fact that comparable motile properties were observed when NOD485 was dimerized by fundamentally different structural mechanisms, parallel coiled-coil versus rapamycin-mediated interaction of FKBP and FRB domains, suggests that any condition favoring a monomer to dimer transition, including localized enrichment on chromatin, should be sufficient to support NOD motility. In addition to

chromatin enrichment, we cannot rule out that an accessory protein(s) ("Factor X") promotes and/or stabilizes NOD dimers *in vivo*. Association of a Factor X could also regulate NOD's atypical mechano-chemical cycle (Cochran et al., 2009) such that it behaves more like conventional kinesin motors in cells. Like NOD, numerous motors have non-canonical neck structures that have been found to bind key regulatory factors in this region (Davies et al., 2015). While further investigation into the physiological regulation of NOD by post-translation modifications, accessory factors, etc., may be worthwhile to better refine our understanding of NOD motility, we argue that the demonstration of plus-end directed motility in this study sufficiently warrants NOD joining its kinesin-10 orthologues in being classified as a motile kinesin.

We also posit that NOD produces PEFs by coupling the force of MT polymerization into chromosome movement via a new EB1-binding motif within an intrinsically disordered region between the motor and DNA binding domains. Like motility, NOD tip-tracking in cells required dimerization of the motor domain and non-conventional neck extension region since obvious tip-tracking was not evident in NOD485- or NOD324CC-expressing cells. However, neither NOD325-485 nor NOD325-485CC exhibited tip-tracking in cells indicating that the neck extension was not sufficient for robust tip-tracking activity (Table 1). Thus, although we measured a Kd of 725 nM between the NOD PT motif-1 and Drosophila EB1, which is comparable to or stronger than the affinities of SxIP motifs and CAP-Gly domains for EB1, additional EB1 binding domains in the neck region and/or motor domain may contribute to NOD tip-tracking in cells (Fig.

5). Similarly, the motor Kar9 in which the LxxPTPh motif was recently characterized possesses three EB1-interacting motifs (1 LxxPTPh, 2 SxIPs) within its C-terminal disordered region (Kumar et al., 2017b; Manatschal et al., 2016). Indeed, the SPOT array identified a second potential PT motif in the neck extension region of NOD that will be further characterized. In conclusion, the identification of conserved new EB1-interacting motifs in NOD not only has ramifications for novel PEF-producing mechanism by chromosome-associated tip-trackers but, more broadly, for identifying and characterizing the functions of an entirely new class of tip-tracking proteins.

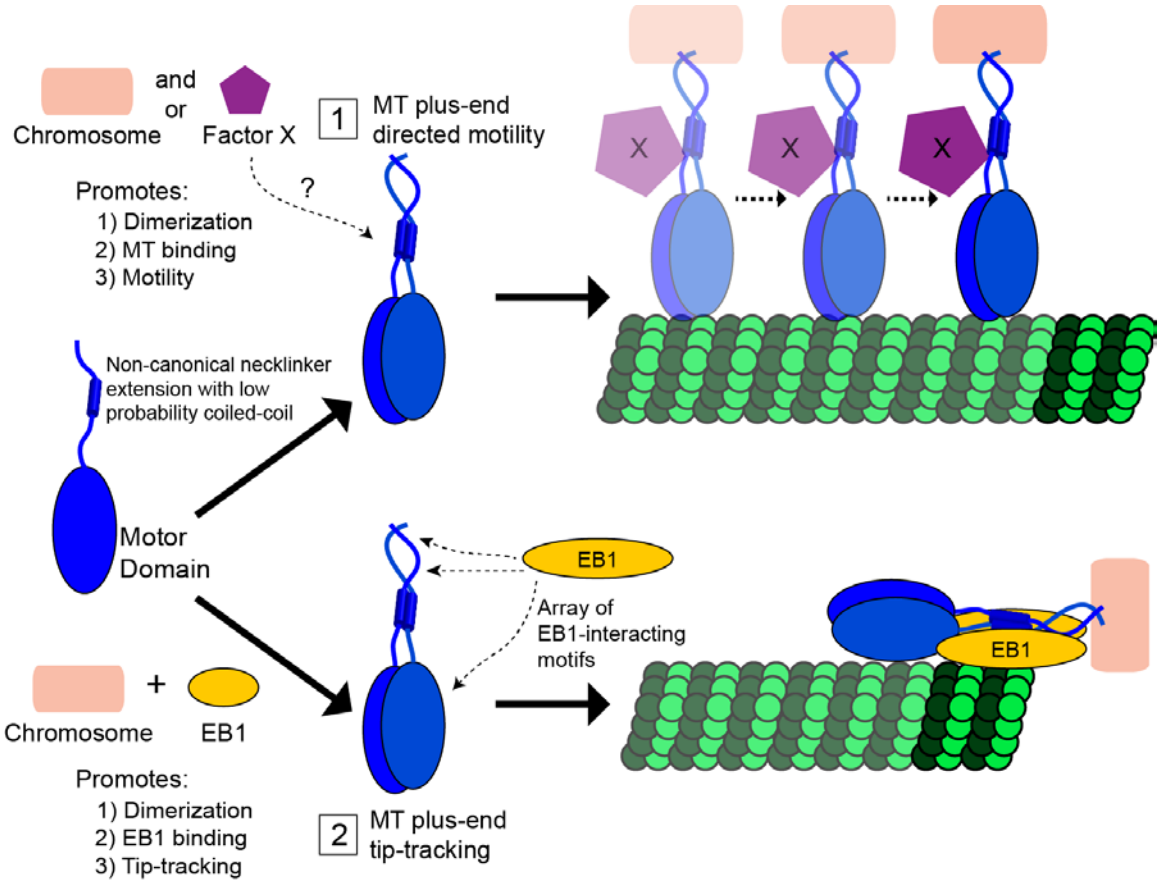

Figure 3.21. NOD generates PEFs through two mechanisms: MT plus-end directed motility and MT plus-end tip-tracking on polymerizing MTs via EB1 interaction.

Model for how NOD is generating PEFs via two pathways. (1) NOD dimerization through a low-probability coiled-coil domain activates plus-end directed motility. Dimerization could be promoted by (a) local concentration on the chromosome and/or (b) association of a binding partner(s) (Factor X) with the non-canonical neck extension region. (2) NOD tip-tracks on polymerizing MTs by interacting with EB1 through at least one novel “PT” motif located in the non-conventional neck extension region although there may be additional EB1 binding motifs located elsewhere in NOD, including the motor domain.

3.4 Materials and Methods

3.4.1 Cell Culture

Drosophila S2 cells were grown in Schneider's medium (Life Technologies) supplemented with 10% heat inactivated fetal bovine serum (FBS) and 0.5x antibiotic/antimycotic cocktail (Sigma), and maintained at 25°C. All cell lines were generated by transfecting the plasmid with Effectene Transfection Reagent system (Qiagen), following manufacture protocol. Expression of the proteins was checked by fluorescence microscopy. Cells expressing the constructs were selected by splitting them in the presence of 25µg/ml Blasticidin S HCl (Fisher) and/or 250µg/ml Hygromycin (Gibco) until cell death ceased at which point cells were maintained in media without drugs. Protein expression is induced with 500µM (high induction) or 25µM (low induction) $CuSO_4$ for 16-18 hours.

3.4.2 DNA Construct

Different NOD truncations were amplified from NOD cDNA (CG1763), with 5' KpnI and 3' SpeI sites and inserted into pMT-V5 vector with a C-terminal mCherry tag inserted between SpeI and SacII. Human kinesin-1 coiled-coil was amplified from a KIF5B construct (gift from Jennifer Ross) with flanking SpeI sites and inserted into the previous plasmid. A single Strep-tag® (ASWSHPQFEK) was added to the C-terminus by incorporating the DNA sequence (5' – GCTAGCTGGAGCCACCCGCAGTTCGAAAAA – 3') to the mCherry reverse primer. FKBP was amplified from FKBP-myc, a gift from Carolyn Bertozzi (Addgene plasmid # 20211) and FRB was amplified from pEYFP-Mitotrap, a gift

from Margaret Robinson (Addgene plasmid # 46942) with flanking SpeI sites and inserted between NOD and the fluorescent tag.

3.4.3 Protein Purification from *Drosophila* S2 cells

NOD85CC-mCherry-STREP was purified from *Drosophila* S2 cells. Cells were grown in 75mm^3 tissue culture flasks until confluent. Cells were induced with 500µM $CuSO_4$ 24 hrs prior to harvesting. Harvested cells were re-suspended in chromokinesin buffer (45mM KCl, 36mM Pipes, 90mM K acetate, 5mM $MgCl_2$, 1mM EGTA, 1% Glycerol, 1mM DTT, 1mM PMSF, 10µg/ml Pepstatin, 20µg Leupeptin, 1mM MgATP, 0.5% Triton X-100, 100µg/ml κ-casein) and spun at 15K RPM at 4°C for 15 minutes. The supernatant was added to washed MagStrep "type3" XT beads (IBA, Germany), incubated at 4°C for 1 hr, and subsequently eluted in chromokinesin buffer supplemented with 75mM biotin. The purified protein was then used in TIRF assays and run on SDS-PAGE gel for silver staining and western blot.

3.4.4 Live-cell TIRF and confocal microscopy

GST-EB1,Cells were allowed to adhere to a concanavalin A treated coverslip and mounted into a rose chamber, or plated on a concanavalin A coated glass bottom petri dish. Cells were imaged on a TIRF-Spinning Disk system assembled on an Eclipse Ti-E inverted microscope (Nikon) equipped with a Borealis (Andor) retrofitted CSU-10 (Yokogawa) spinning disk head and two ORCA-Flash4.0 LT Digital CMOS camera (Hamamatsu) using a 100x 1.49 NA Apo differential

interference contrast objective (Nikon). Metamorph software (Molecular Devices) was used to control the imaging system. Single and dual color TIRF images were acquired at 1 and 2 second intervals, respectively. NOD velocities were measured by manually following motile puncta in cells and *in vitro* assays. All graphs and statistics were done using Prism (GraphPad).

3.4.5 TIRF-based assay using cell lysates

Taxol Taxol stabilized MTs were made by polymerizing 100µM tubulin spiked with 1% Dylite649-labeled tubulin (Cytoskeleton) at 37ºC, and stabilized with 20µM taxol. Cell lysate was made by plating cells on a concanavalin A coated 100mm petri dish, and inducing NOD expression overnight. Cells were washed once with 1x PBS, and lysed in 300µL of chromokinesin buffer (45mM KCl, 36mM Pipes, 90mM K acetate, 5mM $MgCl_2$, 1mM EGTA, 1% Glycerol, 1mM DTT, 1mM PMSF, 10µg/ml Pepstatin, 20µg Leupeptin, 1mM MgATP, 0.5% Triton X-100, 100µg/ml κ-casein). The lysate was clarified by centrifugation at 4ºC for 10 min at 15K RPM. Flow cells were made by adhering a glass cover slip to a glass slide using 2 strips of double sided tape, leaving a chamber volume of ~10µl. Anti-tubulin antibody YL½ diluted to 100µg/ml was first flowed into the chamber and incubated for 5 minutes, then blocked with 5% pluronic F-127 for 5 minutes. Taxol stabilized microtubules (1µM) were next flowed into the chamber and incubated for 5 minutes followed by another block with 5% pluronic F-127 for 5 minutes and a wash with 1x BRB80. Finally, cell lysates and/or purified protein were diluted to achieve a reasonable density of NOD puncta on MTs into the

activation mix (45mM KCl, 36mM Pipes, 90mM K acetate, 5mM $MgCl_2$, 1mM EGTA, 1% Glycerol, 1mM DTT, 1mM MgATP, 0.5% Pluronic F-127, 0.5% Triton X-100, 100μg/ml κ-casein), flowed into the chamber, and subjected to TIRF imaging.

3.4.6 Bacterial Protein Purifications and Pulldown Assays

GST-EB1, MBP-NOD485CC-EGFP, and MBP-EGFP were expressed and purified from Rosetta™ (DE3) cells, following manufacturer's protocol, except the following buffer was used: 50mM Hepes, 50mM sucrose, 100mM KCl, 2mM $MgCl_2$, 0.5mM EGTA, 1mM PMSF, 1mM DTT, and protease inhibitor cocktail. Two-fold molar excess of MBP-NOD485CC-EGFP, and MBP-EGFP as control, was added to GST-EB1-TagRFP in the presence of 5mg/ml BSA, and incubated at 25°C with agitation for 1 hours, then added to amylose magnetic beads (NEB) and incubated for an additional hour at 25°C. Amylose magnetic beads were washed and pre-blocked with 10mg/ml BSA for 1 hour prior to addition of the proteins. Protein was eluted from the beads with 20 μl of 1x SDS sample buffer, and 5 μl of the elution samples were run on a SDS-PAGE gel for analysis with 5% of the EB1 input, and transferred to a nitrocellulose membrane for western blot analysis. Samples were run in parallel, blotted with α-GFP antibody (Abcam) at 1:30,000 or α-TagRFP (Evrogen) at 1:5000 separately, using the appropriate HRP secondary antibodies.

3.4.7 Western Blots

Proteins were loaded into a 10% SDS-PAGE gel, run out, and transferred to a nitrocellulose membrane on the Trans-Blot® Turbo™ transfer system (Bio-Rad Laboratories) using the preprogrammed “MIXED MW” 7 minute protocol. All antibodies were diluted in TBS with 0.1% Tween and 5% milk. Antibodies used were: anti-EB1 serum (gift from Steve Rogers) at 1:5000, anti-mCherry (ThermoFisher) at 1:5000, anti-GFP (Abcam) at 1:30,000 and anti-TagRFP (Evrogen) at 1:5000. All secondary antibodies (Jackson ImmunoResearch Laboratories, Inc.), diluted at 1:5000, were used in conjunction with their respective primaries. Imaging of the membrane was done on a G:Box system controlled by GeneSnap software (Syngene).

3.4.8 Peptide Array

SPOT peptide array membranes were generated by Biopolymers & Proteomics Laboratory at Koch Institute at MIT. The membrane was first blocked with blocking buffer (1x blocking buffer [Sigma], 1x TBS, .05% sucrose) overnight at room temperature (RT), then incubated with 5µg/ml purified EB1-TagRFP-T for 3 hours at RT, and then washed 3x with 1x TBS. Protein binding was detected using anti-EB1 serum diluted at 1:1000 in the blocking buffer, followed by 3X wash with 1X TBS, and incubation with the corresponding HRP secondary. The control blot of the SPOT array was blocked overnight then washed 3x with 1x TBS before incubating with anti-EB1 serum.

3.4.9 Microscale thermophoresis (MST)

NOD “PT” motif-1 and perfect SxIP aptamer was N-terminal labeled with FITC by incubating 5-fold molar excess of the dye to the peptide in 1x PBS and incubated at room temperature (25°C) for 2 hours. The free dye was removed from the

labeled peptide through Ziptip C18 (Milipore). Peptide concentration after labeling was determined by 205nm absorbance, with the extinction coefficient defined according to (Anthis and Clore, 2013). A series of GST-EB1 titrations were added to 50nM of labeled peptide in the presence of 0.5% tween, filled into 16 standard MST capillary tubes (NanoTemper Technologies) for a single experiment, then subjected to thermophoresis measurements in a Monolith NT.115 (Nanotemper). Fluorescence was recorded for 20 secs using 20% laser power. F_{norm}(‰) is the change in fluorescence of the “hot” region at 5 seconds in respect to the “cold” region at time = 0. The dissociation constants were calculated by plotting ΔF_{norm} (change of F_{norm} in respect to the zero EB1 concentration) against GST-EB1 concentrations on a log scale X-axis, and fitting the data using a Michaelis-Menten equation in Prism (GraphPad).

CHAPTER 4

AURORA A KINASE CONTRIBUTES TO A POLE-BASED ERROR CORRECTION PATHWAY

All experiments were achieved in collaboration with Christopher M. Hoel (UMASS), Jovanna Deretic and Julie P. Welburn (University of Edinburgh), and Albert W. Hinman and Daniela Cimini (Virginia Tech). CMH did the MLN8237 titration and Mad1 experiments. JD and JPW did all experiments in HeLa cell. AWH and DC did all the experiments in Ptk1 cells. With the guidance of Prof Thomas Maresca, I developed the FRET assays and validated all chemical inhibitions and RNAi conditions. This chapter is published in *Current Biology* in 2015 (Ye et al., 2015).

4.1 Introduction

Chromosome biorientation, where sister kinetochores attach to microtubules (MTs) from opposing spindle poles, is the configuration that best ensures equal partitioning of the genome during cell division. Erroneous kinetochore-microtubule (kt-MT) attachments are commonplace but often corrected prior to anaphase (Cimini et al., 2003; Kitajima et al., 2011). Error correction, thought to be mediated primarily by the centromere-enriched Aurora B kinase (ABK) (Cimini et al., 2006; Kelly and Funabiki, 2009; Tanaka et al., 2002), typically occurs near spindle poles(Lampson et al., 2004); albeit, the relevance of this locale is unclear. Furthermore, polar ejection forces (PEFs), highest near poles (Ke et al., 2009), can stabilize improper attachments by pushing mal-oriented chromosome

arms away from spindle poles (Cane et al., 2013; Nicklas and Koch, 1969). Hence, a conundrum: erroneous kt-MT attachments are weakened where PEFs are most likely to strengthen them. Here we investigate this discrepancy and report that Aurora A kinase (AAK) opposes the stabilizing effect of PEFs. AAK phosphorylates kinetochore substrates near poles and its inhibition results in chromosome mis-alignment and an increased incidence of erroneous kt-MT attachments in *Drosophila* and mammalian cells. Furthermore, AAK contributes to phosphorylation of a bona-fide ABK site in the N-terminal tail of Ndc80/Hec1 that has been implicated in reducing the core kt-MT attachment factor's affinity for MTs when phosphorylated (Cheeseman et al., 2006; Ciferri et al., 2008; DeLuca et al., 2006). We propose that spatial positioning of mal-oriented chromosomes near spindle poles reduces kt-MT attachment stability via an AAK error correction gradient.

4.2 Results

Bioriented attachments are thought to be stabilized, in part, by tension-dependent movements (Maresca and Salmon, 2009; Uchida et al., 2009) of outer kinetochore components away from AURKB. The resultant spatial separation correlates with a reduction in phosphorylation of kt-MT attachment factors (Liu et al., 2009; Suzuki et al., 2014) that is proposed to increase the kinetochore's affinity for MTs (Welburn et al., 2010). Flawed attachments are weakened in favor of bioriented kinetochores through a process called error correction. Many models evoke tension-dependent inhibition of centromere (CEN)-based error correction via spatial separation (Maresca and Salmon, 2010). The concept is reasonable if erroneous attachments are "tensionless", yet improper attachments may come under tension when mal-oriented chromosomes are opposed by PEFs (Cassimeris et al., 1994). In support of this, we previously reported that elevated PEFs stabilize syntelic attachments (Cane et al., 2013), where sister kinetochores attach to the same pole, by overwhelming AURKB. Thus, while CEN-based models explain the instability of tensionless attachments, they fail to account for error correction when PEF-generated tension opposes AURKB. Furthermore, recent work suggests that CEN-based Aurora kinase is dispensable for error correction in budding yeast as mutants with Ipl1 (*S.c.* Aurora homologue) enriched on the spindle rather than the centromeres still achieved biorientation (Campbell and Desai, 2013). Clearly, a more comprehensive understanding of error correction requires further inquiry.

Unlike budding yeast, metazoans possess multiple Aurora kinases, most notably AURKB and AURKA, enriched at centromeres and spindle poles/centrosomes respectively (Carmena and Earnshaw, 2003). As the kinases share nearly identical consensus target motifs (Cheeseman et al., 2002), it is likely that the principal determinant of their substrate specificity is their respective sub-cellular localizations (Li et al., 2015). Here, we investigate whether a non-CEN-based pathway contributes to error correction by testing the hypothesis that AURKA phosphorylates kinetochore substrates in the vicinity of poles.

We previously developed a cell-based assay in which tension can be experimentally elevated at kinetochores by manipulating PEF-production (Cane et al., 2013). In the PEF assay, inducible over-expression of the major PEF-producing kinesin-10 motor NOD (Theurkauf and Hawley, 1992) results in a dose-dependent increase in stable syntelic attachments in *Drosophila* S2 cells. To examine if AURKA affects the ability of PEFs to stabilize syntelic attachments, a cell line was created in which both NOD and AURKA could be over-expressed simultaneously via $CuSO_4$ induction (Figure 4.1A). AURKA-GFP localized to spindle MTs to varying degrees depending on the level of overexpression and was always highly enriched at centrosomes (Figures 4.1B and 4.1C). In agreement with previous observations in HeLa cells (Stenoien et al., 2003), the centrosome-enriched population of AURKA-GFP turned over with rapid kinetics ($t_{1/2}$ of 7seconds) in S2 cells (Figures S1A, S1B). Inducible NOD-mCherry and AURKA-GFP cells co-expressing Ndc80-GFP, to assess attachment states, were subjected to the PEF assay. Cells with and without AURKA-GFP expression on

the same coverslip could be compared due to variability in expression levels. Importantly, AURKA over-expression reduced the potency of the PEF effect (Figures 4.1D-G). Thus, AURKA over-expression attenuates the kt-MT attachment stabilizing effects of elevated PEFs in S2 cells.

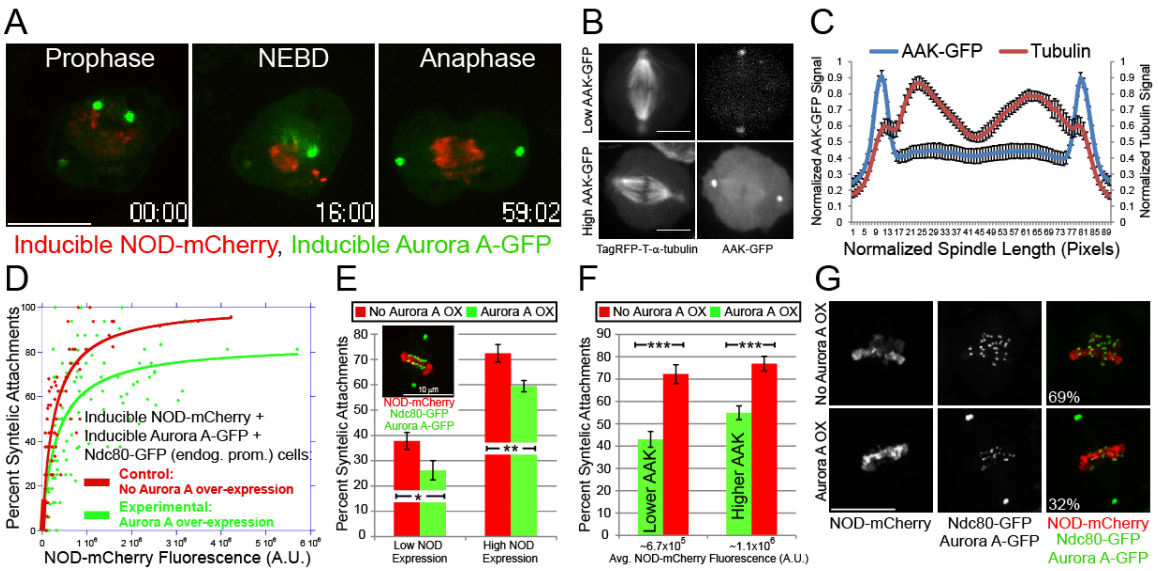

Figure 4.1. Aurora A kinase at the poles counteracts kt-MT stabilizing effects of elevated NOD expression.

(A) Still frames from a time-lapse of a dividing S2 cell expressing inducible NOD-mCherry and inducible AAK-GFP. (B) Scanning confocal images showing examples of low (top) and high (bottom) over-expressing cells. Microtubule localization is more evident in the higher expressing cell. (C) Normalized fluorescence intensities of AAK-GFP and Tag-RFP-α-tubulin along the length of 14 mitotic spindles (normalized for variability in spindle length) from cells with a range of AAK-GFP over-expression. AAK-GFP is most abundant at centrosomes and its levels are slightly higher closer to the spindle poles than in the mid-spindle. (D) Plots of percent syntelic attachments versus NOD-mCherry fluorescence for cells with (green) and without (red) AAK-GFP over-expression. PEF-mediated stabilization of syntelic attachments is less potent in AAK-GFP over-expressing cells. Data from 6 independent experiments were fit with a hyperbolic function; Control; n = 64 cells, Aurora A over-expression; n = 117 cells. R-values are 0.81 (no Aurora A over-expression) and 0.72 (Aurora A over-expression). (E) Mean percent syntelic attachments for low and high NOD-expressing cells, defined by the halfway point of the expression range in control cells, in control versus AAK-GFP over-expressing (inset) cells. The percentage of syntelic attachments is significantly lower in AAK over-expressing cells than in control cells at low and high NOD expression levels. (F) AAK-GFP levels were quantified and the mean percent of syntelic attachments in cells from both the lower and upper half of the AAK-GFP over-expression range are significantly lower than groupings of control cells with comparable levels of NOD over-expression. (G) Maximum intensity projections of Ndc80-GFP (green), NOD-mCherry (red) expressing cells with and without over-expressed AAK-GFP (green) but with comparable levels of NOD-mCherry. The percentage of syntelic attachments, which is lower in the AAK-GFP over-expressing cell, is shown in the merged images.

The observation that centrosomal/spindle pole-enriched AURKA affected kt-MT attachment stability suggested that the kinase could phosphorylate substrates at a distance through an activity gradient. A FRET-based sensor that exhibits changes in intramolecular FRET upon phosphorylation (Violin et al., 2003) was used to probe this possibility. In the reporter used here, Aurora kinase phosphorylation causes a structural rearrangement such that phosphorylation leads to reduced FRET efficiency (Fuller et al., 2008) and a prior strategy (Tseng et al., 2010) was adapted to target the reporter to microtubules in S2 cells (Figure 4.2A). To isolate the contribution of AURKA to probe phosphorylation, cells co-expressing TagRFP-T-α-tubulin and the Tau-Aurora FRET reporter were treated with a high dose (40 μM) of the *Drosophila* AURKB-specific inhibitor binucleine 2 (Eggert et al., 2004; Smurnyy et al., 2010). This treatment, which requires the addition of MG132 to prevent mitotic exit, results in monopolar spindle assembly in a majority of cells. Three categories of FRET emission ratios at the monopole center, as defined by Tag-RFP-α-tubulin signal, relative to ~3 μm away emerged when FRET of the MT-associated reporter was examined across monopoles (Figure 4.1B): weak/undetectable gradients (<5% reduction in FRET ratio), moderate gradients (5-10% reduction), and strong gradients (>10% reduction). AURKA activity was required for FRET-based visualization of the gradients as depletion of AURKA led to a reduction in the number of cells with strong gradients relative to control RNAi-treated cells (Figures 4.1C) and most AURKA-depleted cells had weak/undetectable gradients (Figure 4.1D). A substantial majority of cells (86%) did not have detectable

gradients in cells expressing a non-phosphorylatable (negative control) version of the reporter (Figure 4.1E). Thus, a pole-centered AURKA phosphorylation gradient is present in mitotic *Drosophila* S2 cells.

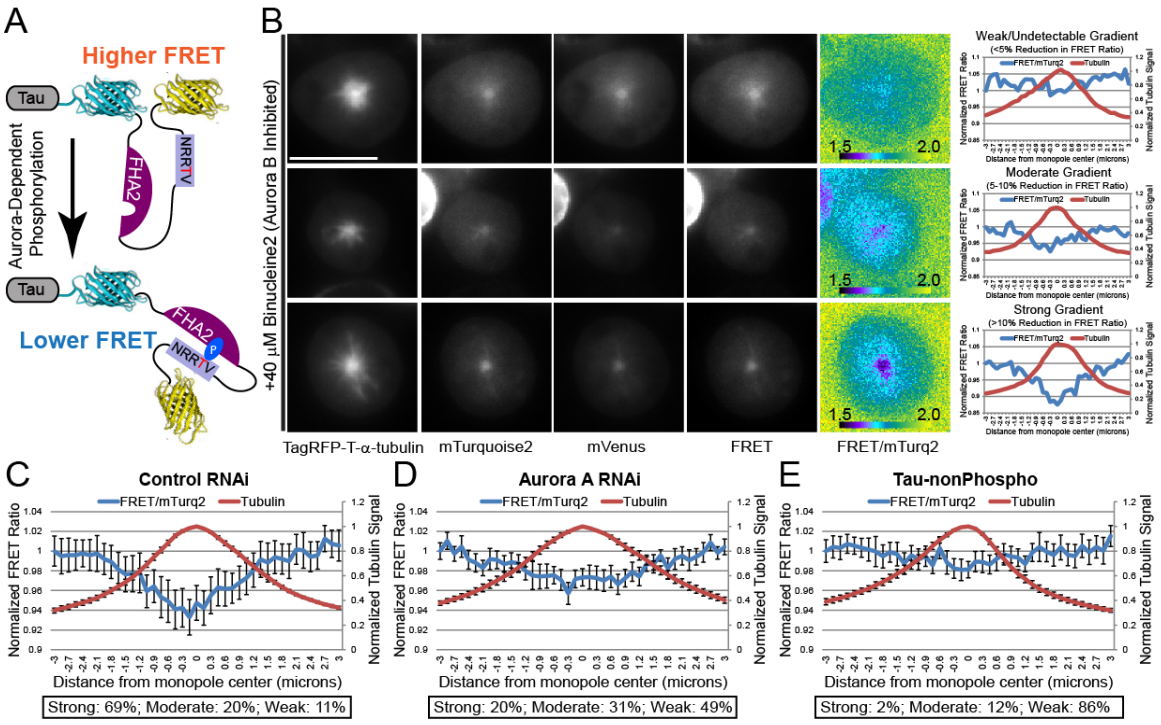

Figure 4.2.Aurora A Kinase gradient around the centrosomes.
(A) Schematic of the microtubule-targeted Tau-Aurora FRET sensor used in this study. (B) Representative images of cells co-expressing TagRFP-T-α-tubulin and the Tau-Aurora FRET reporter treated with binucleine 2 and MG132. The FRET emission ratio images "FRET/mTurq2" are pseudo-colored and the color wedge spans ratio values of 1.5 (black) to 2.0 (yellow). Examples of cells with Weak/Undetectable, Moderate, and Strong gradients (as defined by the % reduction in FRET efficiency in the monopole center relative to 3 μm away) are shown. (**C-E**) Normalized FRET ratios across monopoles (normalized tubulin intensity) from 10 cells per condition. Each plot contains data reflecting the percentage of each type of gradient in that condition (for example, the control RNAi plot is from 7 strong, 2, moderate and 1 weak). Control RNAi, n = 35 cells; Aurora A RNAi, n = 45 cells; Tau-nonPhospho, n =41 cells. Scale bars, 10 μm. Error bars are SEM.

While PEFs act on chromosome arms, it is the transmission of opposing force through the mis-attached kinetochores that leads to their stabilization. Thus, we

reasoned that the AURKA activity gradient counteracts the PEF effect by targeting kinetochore substrates that approach the spindle poles. To test this hypothesis we adapted a strategy previously used to target the Aurora kinase FRET sensor to human kinetochores (Liu et al., 2009) for use in *Drosophila* S2 cells by fusing the FRET reporter to the C-terminus of TagRFP-T-tagged *Drosophila* Mis12, a component of the core kt-MT attachment complex (Cheeseman et al., 2006) (Figure 4.3). We confirmed earlier findings from HeLa cells (Liu et al., 2009) that the sensor is more phosphorylated (lower emission ratio) at unattached kinetochores than at bioriented kinetochores in *Drosophila* S2 cells (Figures 4.3). Cells treated with binucleine 2 exhibited reduced sensor phosphorylation at unattached kinetochores (Figures 4.3). The FRET measurements in binucleine 2-treated cells likely underestimate the reduction in phosphorylation given that a non-phosphorylatable reporter, which has equally high emission ratios at bioriented and unattached kinetochores, exhibited a 5% reduction in FRET in the presence of 40 μM binucleine 2 (Figures S2A and S2B). Taken together, the data suggest that AURKB is the dominant kinase targeting the Mis12-FRET sensor at unattached kinetochores in S2 cells.

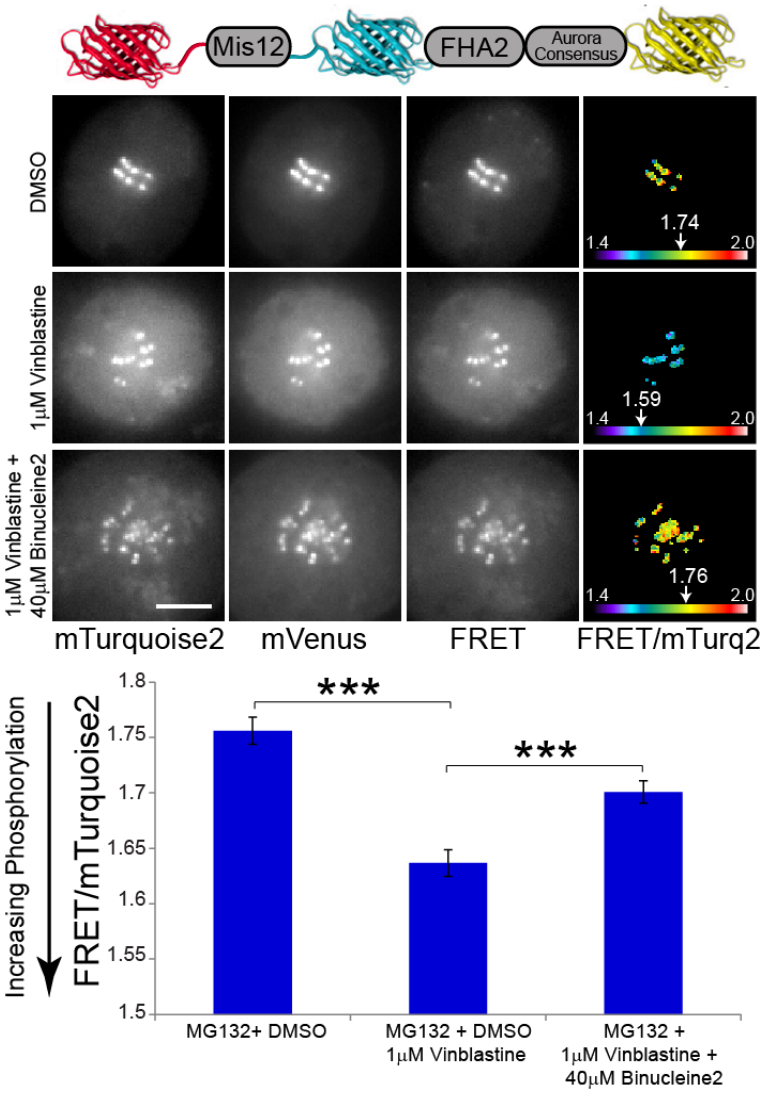

Figure 4.3. Kinetochore targeted FRET based sensor detects phosphorylation of unattached kinetochores.

(A) Schematic of the kinetochore-targeted Mis12-Aurora FRET sensor used in this study. (B) Representative images of the FRET reporter in the conditions shown in (c). The FRET emission ratio images "FRET/mTurq2" are pseudo-colored and the arrows point to the position on the color wedge (spanning ratio values of 1.4 to 2.0) corresponding to the average emission ratio measured for the kinetochore-targeted sensor in that cell. (C) Vinblastine treatment, to generate unattached kinetochores, lowers the emission ratio of the FRET reporter indicating that it is more phosphorylated. Binucleine 2 treatment leads to an increase in the reporter FRET emission ratio at kinetochores in vinblastine-treated cells demonstrating that ABK contributes to phosphorylation of the sensor at unattached kinetochores. Mean values from 3 independent experiments; DMSO; n = 106 cells, vinblastine; n = 104 cells, vinblastine + binucleine 2; n =108 cells. All error bars represent the SEM. Scale bars, 5μm. P-values from Mann-Whitney Wilcoxon t-test are reported: not significant (n.s.) p-value > 0.05, * p-value < 0.05, *** p-value < 0.0005.

Sensor phosphorylation at aligned and polar kinetochores was next evaluated. The *Drosophila* CENP-E homologue (CENP-meta) was depleted from cells expressing the kinetochore-targeted FRET sensor to increase the number of polar chromosomes (Yucel et al., 2000). The FRET sensor was more phosphorylated at polar kinetochores than at bioriented kinetochores (Figures 4.4A and 4.4B). Since polar chromosomes in CENP-E depleted mouse fibroblasts have been shown to lack kt-MT attachments (Putkey et al., 2002), the increased phosphorylation observed at these kinetochores may have solely been a result of AURKB-mediated phosphorylation of unattached kinetochores. However, this was not the case, as double depletion of CENP-meta and AURKA, which did not reduce AURKB activity, resulted in a reduction in phosphorylation of the reporter at polar kinetochores relative to those in CENP-meta RNAi cells (Figures 4.4A and 4.4B). The data do not rule out a role for AURKB in phosphorylating polar kinetochores in S2 cells, which may account for the statistically significant increase in phosphorylation of the reporter at polar versus aligned kinetochores that remained in AURKA depleted cells (Figure 4.4A). Unfortunately, the effects of binucleine 2 on FRET measurements combined with catastrophic failure in bipolar spindle assembly in AURKB-inhibited S2 cells made it technically infeasible to measure FRET ratios at polar versus bioriented attachments in AURKB-inhibited cells. Nonetheless, the data support the conclusion that an AURKA activity gradient contributes to phosphorylation of the Mis12-FRET sensor at polar kinetochores in S2 cells.

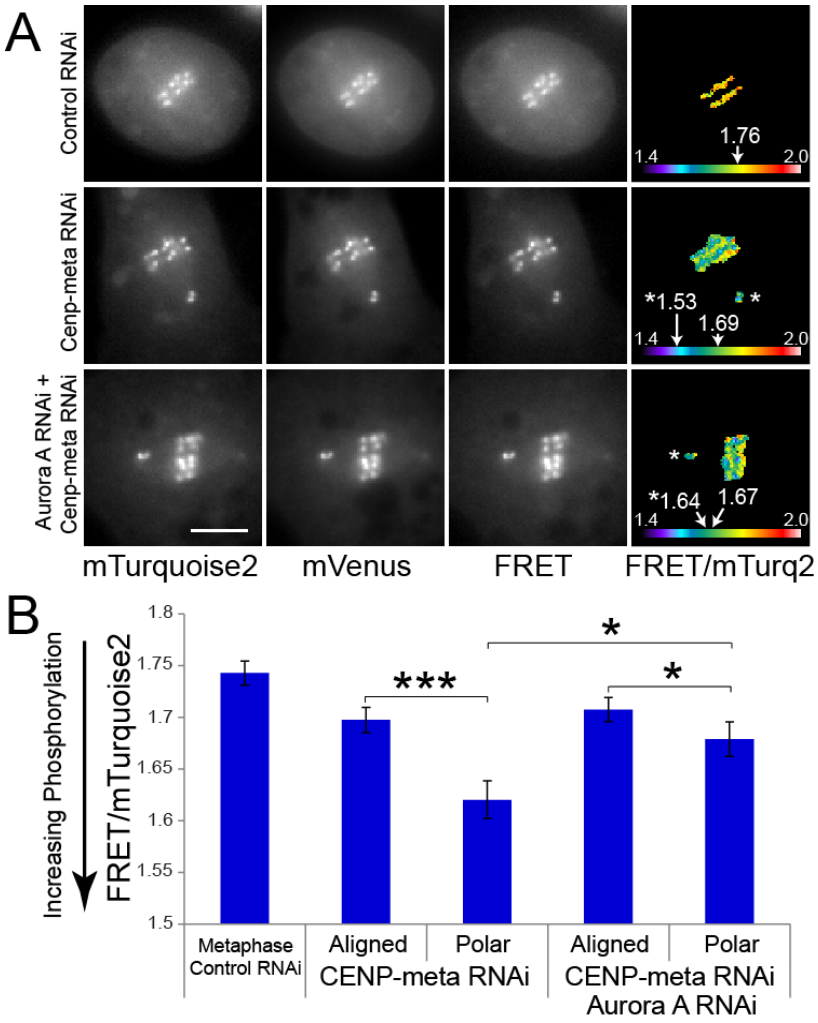

Figure 4.4. Misaligned kinetochores near the pole are more phosphorylated than aligned ones, in an AAK dependent manner.

(A) Representative images of the FRET reporter in the conditions shown in (B). The FRET emission ratio images "FRET/mTurq2" are pseudo-colored and the arrows point to the position on the color wedge (spanning ratio values of 1.4 to 2.0) corresponding to the FRET emission ratios measured for the sensor at aligned and, when appropriate, polar kinetochores (asterisk) in that cell. (B) The mean FRET emission ratio of the sensor is lower at polar kinetochores, generated by depleting CENP-meta, than at aligned kinetochores. Co-depleting AAK leads to an increase in the emission ratio at polar kinetochores compared to polar kinetochores in CENP-meta depleted. Thus, the sensor is more phosphorylated at kinetochores near spindle poles than at bioriented kinetochores and AAK contributes to this difference in the phosphorylation state. Mean values from 3 independent experiments; Control RNAi; metaphase; n = 119 cells, CENP-meta RNAi; metaphase; n = 98, misaligned; n = 107; CENP-meta, Aurora A double RNAi; metaphase; n =106, misaligned; n = 120. All error bars represent the SEM. Scale bars, 5μm. P-values from Mann-Whitney Wilcoxon t-test are reported: not significant (n.s.) p-value > 0.05, * p-value < 0.05, *** p-value < 0.0005.

The checkpoint protein Mad1, which is depleted from stable kt-MT attachments (Shah et al., 2004), was next used to probe the attachment states of polar kinetochores in the presence and absence of AURKA activity. Mad1 levels at kinetochores were examined in CENP-meta depleted cells expressing Mad1-GFP under the control of its endogenous promoter (Figures 4.5A and 4.5B). To measure Mad1 enrichment at polar kinetochores, the ratio of background corrected fluorescence intensities of Mad1-GFP to Ndc80 signals at mis-aligned kinetochores was compared to the average Mad1 to Ndc80 ratio intensities of 6 bioriented kinetochores within the same cell. Indicative of a lack of attachment (Putkey et al., 2002), polar kinetochores, on average, exhibited a ~26 fold increase in Mad1 levels relative to bioriented attachments in CENP-meta depleted cells treated with DMSO. Treatment with 125 nM MLN8237, an AURKA-specific inhibitor (Pollard and Mortimore, 2009), that potently and specifically inhibits *Drosophila* AURKA (Figures S3A-S3C) caused a significant reduction in Mad1 enrichment (~4 fold) at polar kinetochores. The observed differences in kinetochore-associated Mad1 levels were not due to general effects of the treatments on Mad1 localization as neither MLN-treatment, CENP-meta depletion, nor the combination affected Mad1 loading at unattached kinetochores (Figure 4.5C). These findings along with recent work (Barisic et al., 2014) suggest that polar kinetochores in CENP-meta depleted cells establish stable attachments when AURKA is inhibited.

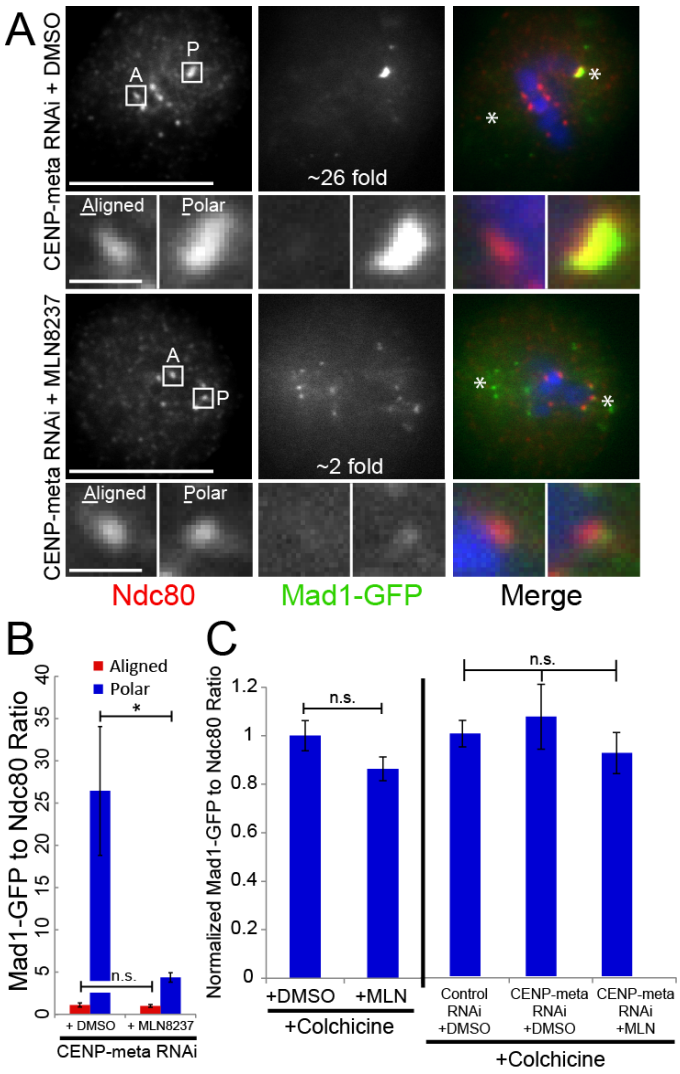

Figure 4.5. Kt-MT attachment of polar kts is destabilized by AAK.
(A) Single planes from representative images of CENP-meta depleted Mad1-GFP (green in merged images) expressing cells treated with DMSO or 125 nM MLN8237 and stained for Ndc80 (red) and DAPI (blue). Examples of aligned (A) and polar (P) kinetochores for each condition are shown in the (5x zoom) insets. The fold-enrichments of Mad1 at the polar relative to aligned kinetochores are indicated in the Mad1-GFP images for each cell. Asterisks indicate the position of the spindle poles. (B) Quantifications of fold Mad1-GFP enrichment at polar kinetochores in CENP-meta depleted cells treated with DMSO (control) or 125 nM MLN8237. Mean values from CENP-meta RNAi + DMSO; n = 18 polar kinetochores; n = 42 aligned kinetochores, CENP-meta RNAi + MLN; n = 46 polar kinetochores, n = 48 aligned kinetochores. (C) Levels of Mad1-GFP ratioed to Ndc80 at unattached kinetochores are unaffected by MLN treatment and CENP-meta depletion. Mean values from 2 independent experiments with colchicine +: DMSO, n = 255 kinetochores; MLN8237, n = 255 kinetochores; Control RNAi + DMSO, n = 200 kinetochores; CENP-meta RNAi + DMSO, n = 198 kinetochores; CENP-meta RNAi + MLN8237, n = 200 kinetochores. All error bars represent the SEM. Scale bars, 10 μm, 1 μm (insets). Two-tailed p-values of Student's t-test are reported: not significant (n.s.) p-value > 0.05, * p-value < 0.05, *** p-value < 0.0005.

Chromosome alignment and kt-MT attachment states were next examined in cells with compromised AURKA activity. Similar to previous observations in S2 cells (Giet et al., 2002), AURKA depletion resulted in ~40% of MG132-treated mitotic cells exhibiting “abnormal metaphases” with at least one misaligned chromosome (Figures 4.6A and 4.6B). Treatment with 125 nM MLN8237 mirrored the AURKA RNAi depletion phenotype (Figures 4.6C and 4.6D). The attachment states of mis-aligned chromosomes were evaluated by carefully examining serial fluorescent z-sections of chromosomes, kinetochores and microtubules in AURKA-inhibited cells (Figures 4.6E-H). The attachment states of the mis-aligned chromosomes fell into four categories: 1) “Mono-oriented (k-fiber)” if one kinetochore was attached to a pole and the other kinetochore was nucleating a second kinetochore fiber (k-fiber) or focused spindle pole extending into the cytoplasm, 2) “Mono-oriented/Lateral” if one kinetochore was attached to a pole and its sister was either unattached or was laterally interacting with a nearby k-fiber (likely in the process of CENP-E-mediated congression (Kapoor et al., 2006)), 3) “Syntelic” if sister kinetochores were attached to the same pole and 4) “Unknown” if the attachment state could not be discerned. Once again, the MLN8237 treatment phenocopied AURKA RNAi (Figures 4.6F and 4.6H). In both conditions, the majority of mis-aligned chromosomes (50-60%) had syntelic attachments while 25-30% had mono-oriented/lateral interactions, suggesting that CENP-meta is active in AURKA inhibited S2 cells. A role for AURKA in error correction was further evidenced by the observation that the PEF effect was more potent in AURKA-depleted cells relative to control RNAi cells (Figures S3D-

S3F). The fixed cell data were corroborated by live-cell imaging of AURKA depleted Ndc80-GFP expressing cells (Figure 4.6I). In an excellent example that captured the chromosome misalignment types observed in fixed AURKA-inhibited cells, a syntelically attached chromosome remained “pinned” at the spindle pole for at least 40 minutes before congressing, most likely via a mono-oriented/lateral interaction, at a rate consistent with CENP-E-driven congression (Kapoor et al., 2006). One of the sister kinetochores then became merotelically attached to both poles, laterally deformed and briefly lagged in anaphase before properly segregating.

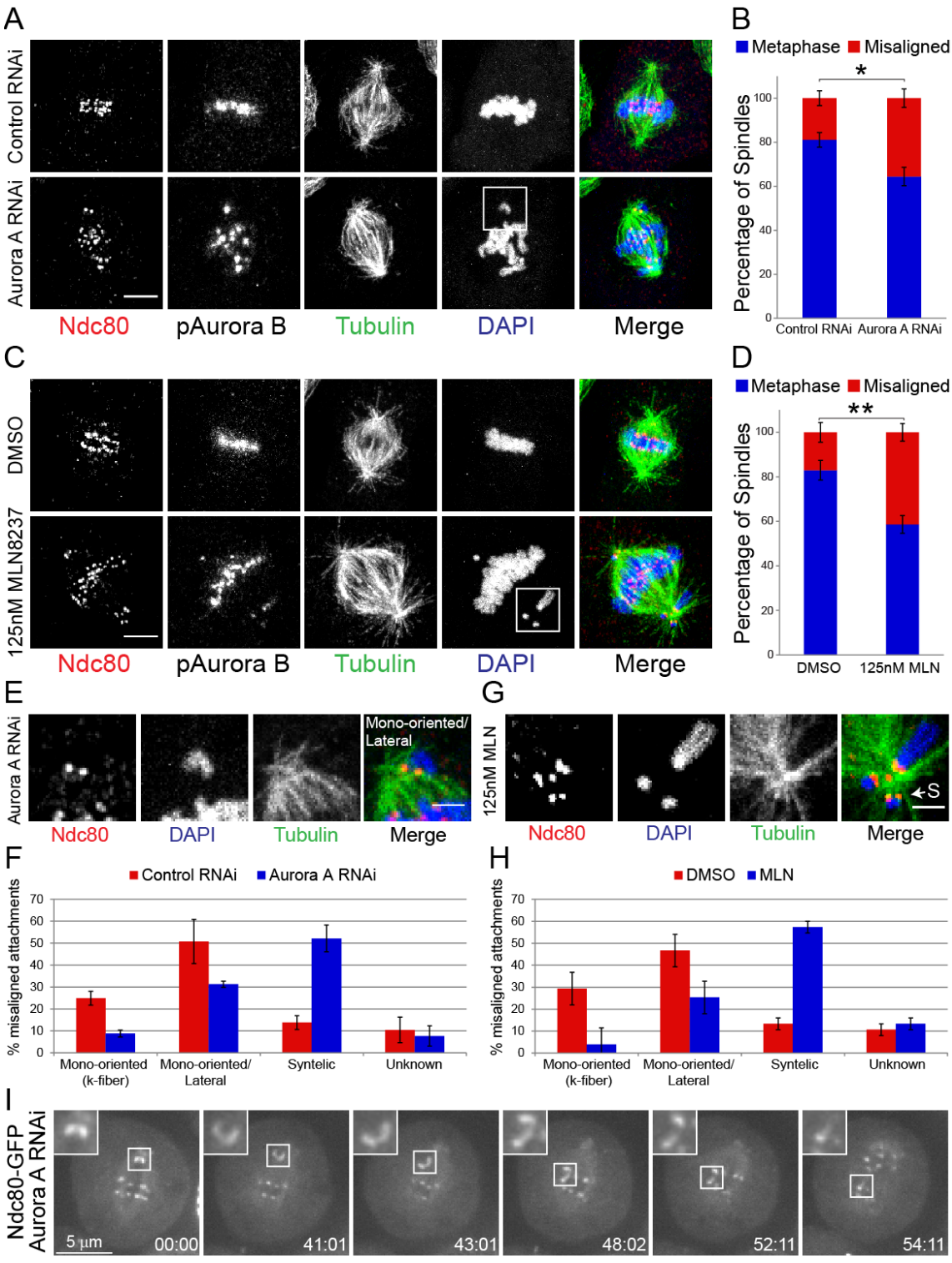
A
Control RNAi
Aurora A RNAi
Ndc80
pAurora B
Tubulin
DAPI
Merge
B
Metaphase
Misaligned
*
Percentage of Spindles
Control RNAi
Aurora A RNAi
C
DMSO
125nM MLN8237
D
**
DMSO
125nM MLN
E
Mono-oriented/ Lateral
G
S
F
Control RNAi
Aurora A RNAi
% misaligned attachments
Mono-oriented (k-fiber)
Mono-oriented/ Lateral
Syntelic
Unknown
H
DMSO
MLN
I
Ndc80-GFP Aurora A RNAi
5 µm
00:00
41:01
43:01
48:02
52:11
54:11

Figure 4.6. AAK is required for efficient error correction in *Drosophila* S2 cells.

(A) Representative maximum projections from confocal z-sections of control and AAK-depleted cells stained for Ndc80 (red in the merged image), phospho-Aurora B, tubulin (green) and DAPI (blue). Misaligned chromosomes with normal levels of centromere-enriched phospho-Aurora B are more prevalent in AAK depleted cells than in control cells. (B) Quantification of the percentage of MG132-treated cells with normal metaphase plates and misaligned chromosomes in control and AAK-depleted cells. Mean values from 3 independent experiments; Control RNAi; n = 317 cells, Aurora A RNAi; n = 326 cells. (C) Representative maximum projections from confocal z-sections of DMSO and MLN8237-treated cells stained for Ndc80 (red in the merged image), phospho-Aurora B, tubulin (green) and DAPI (blue). Treatment with 125 nM MLN8237 phenocopies AAK depletion. (D) Quantification of the percentage of MG132-treated cells with normal metaphase plates and misaligned chromosomes in DMSO- and MLN8237-treated cells. Mean values from 3 independent experiments; DMSO; n = 318 cells, 125 nM MLN8237; n = 322 cells. (E) Zoomed views of the insets highlighted in the DAPI channel in (A). In the merged image Ndc80 is red, tubulin is green and DAPI is blue. (F) Mean values of each type of attachment at misaligned chromosomes in control- and AAK-depleted cells from 3 independent experiments; Control RNAi; n = 71 kinetochore pairs, Aurora A RNAi; n = 80 kinetochore pairs. (G) Zoomed views of the insets highlighted in the DAPI channel in (C). In the merged image Ndc80 is red, tubulin is green and DAPI is blue. Arrow points to a syntelic (S) attachment. (H) Mean values of each type of attachment at misaligned chromosomes in DMSO- and MLN8237-treated cells from 3 independent experiments; n = 75 kinetochore pairs each for DMSO and MLN conditions. (I) Still frames from a spinning disk confocal time-lapse of an Ndc80-GFP expressing S2 cell depleted of AAK. Inset shows an 8X zoom of the highlighted region. Two-tailed p-values of Student's t-test are reported. Error bars are SEM. Scale bars are 5 μm (A, C) and 2 μm (E, G). Two-tailed p-values of Student's t-test are reported: * p-value < 0.05, ** p-value < 0.005.

To investigate if the contribution of AURKA to error correction is conserved beyond *Drosophila*, we used PtK1 cells which, due to their low chromosome number, have been an excellent model for characterizing error correction mechanisms (Cimini et al., 2006; Lampson et al., 2004). First, we identified a concentration (1 μM) of the AURKA inhibitor MLN8054 (Manfredi et al., 2007) that affected chromosome behavior, but did not alter mitotic index, distribution of mitotic stages, or spindle assembly. PtK1 cells treated with 1 μM MLN8054 did not exhibit a reduction in centromere-associated phosphorylated-AURKB, indicating that AURKB activity was not affected by this drug concentration. However, kinetochores in MLN8054-treated prometaphase cells were, on average, positioned closer to the spindle poles than in untreated cells and a significant number of kinetochores localized very close to the poles, which was never observed in control cells (Figures 4.7A and 4.7B). Moreover, MLN8054-treated PtK1 cells displayed higher frequencies of merotelic kinetochores at the metaphase plate than control cells (Figures 4.7C and 4.7D) and; as a result, significantly more anaphase lagging chromosomes were observed in MLN8054-treated cells (Figure 4.7E). These data demonstrate that inhibiting AURKA compromises error correction and results in chromosome mis-segregation in mammalian PtK1 cells.

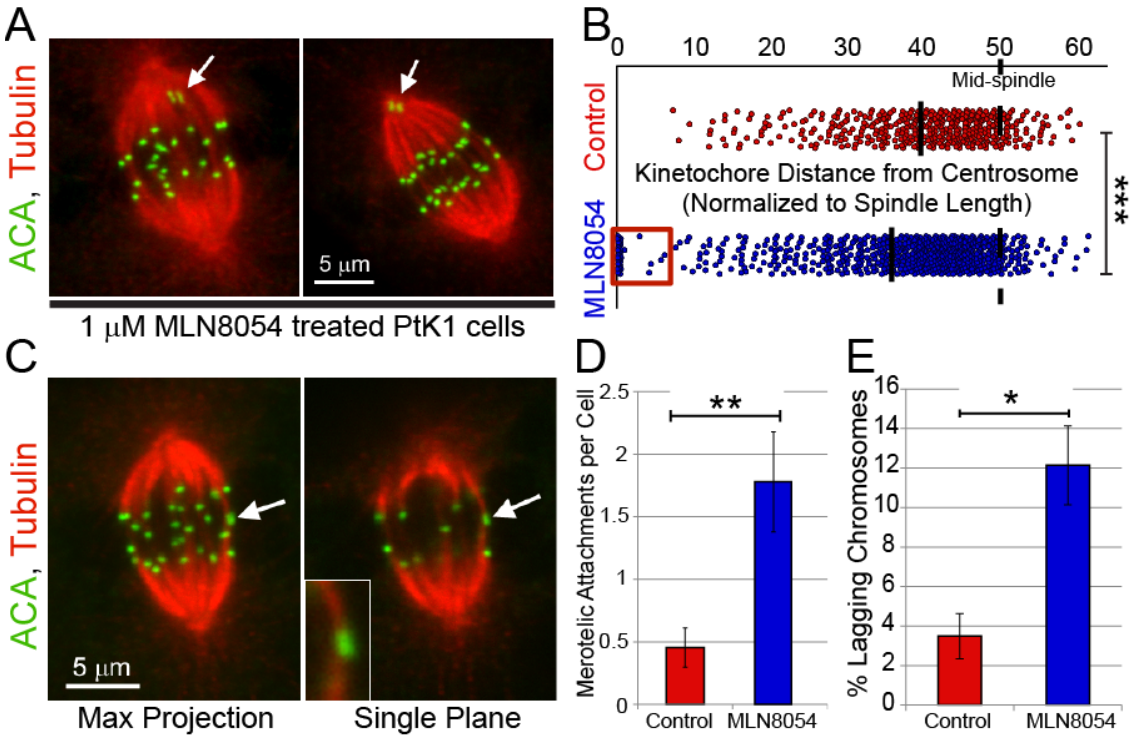

Figure 4.7. AAK contributes to error correction in mammalian cells.
(A) Representative maximum projections of confocal z-sections of PtK1 cells treated with 1 μM MLN8054 and stained for tubulin (red) and centromeres (green). Arrows point to polar, misaligned chromosomes. (B) Scatter plots of relative kinetochore positions normalized to the spindle length in control and MLN8054-treated PtK1 cells. The "0" position represents the spindle pole and the "50" position marks the mid-spindle (dashed black line). The average centromere position (black bar) is closer to the spindle poles in MLN8054-treated cells than in control cells and a significant population of kinetochores are "pinned" to the poles (near 0) in MLN8054-treated cells (red box). Control; n = 406 kinetochores, and 1 μM MLN8054; n = 642 kinetochores. (C) Representative images (maximum projection – left, and single focal plane – right) of a PtK1 cell treated with 1 μM MLN8054 and stained for tubulin (red) and centromeres (green). Arrows point to a merotelic kinetochore at the metaphase plate that is attached to both spindle poles. (D) MLN8054 treatment leads to a significant increase in the average number of merotelic attachments per cell relative to control cells. Control; n = 191 kinetochores from 11 cells, 1 μM MLN8054; n = 144 kinetochores from 9 cells. (E) MLN8054 treatment leads to a significant increase in the percentage of lagging chromosomes in anaphase cells relative to control cells. Mean values of lagging chromosomes from 3 independent experiments for Control; n = 270 anaphase chromosomes, and 1 μM MLN8054; n = 268 anaphase chromosomes. Error bars are SEM. Scale bars are 5 μm (a, c). Two-tailed p-values of Student's t-test are reported: not significant (n.s.) p-value > 0.05, * p-value < 0.05, ** p-value < 0.005, *** p-value < 0.0005.

We reasoned that AURKA regulates error correction by targeting many of the same substrates as AURKB. A crucial target of AURKB is the Ndc80 complex, which directly binds MTs (Alushin et al., 2010; Cheeseman et al., 2006; Ciferri et al., 2008; Wei et al., 2007). High affinity interactions between the Ndc80 complex and MTs requires the unstructured and highly basic N-terminal tail of Ndc80/Hec1 (Ciferri et al., 2008; Guimaraes et al., 2008; Miller et al., 2008; Wei et al., 2007), which contains numerous AURKB sites (Cheeseman et al., 2002; Cheeseman et al., 2006; Ciferri et al., 2008; DeLuca et al., 2006) that, when phosphorylated, lower the complex's affinity for MTs (Cheeseman et al., 2006; Ciferri et al., 2008; Welburn et al., 2010). Thus, we examined the contribution of AURKA to the phosphorylation of a previously defined AURKB site in Ndc80/Hec1 (Ser55) (Cheeseman et al., 2006; Ciferri et al., 2008; DeLuca et al., 2006) by using a phospho-specific antibody against pSer55 in HeLa cells. Compared to control cells, treatment with 300 nM MLN8237 significantly reduced kinetochore pSer55 staining at attached (Figures 4.8A and 4.8B) and unattached kinetochores. The 300 nM MLN8237 treatment caused a minor but significant reduction in Ndc80 levels relative to CENP-A, which may be due to partial inhibition of AURKB at this inhibitor concentration, although phospho-H3-Ser10 levels were not significantly reduced relative to control metaphase cells. These data are consistent with a phospho-proteomic study that implicated AURKA as the primary kinase targeting Ndc80-Ser55 (Kettenbach et al., 2011). While cell-based inhibitor studies suggest that AURKA contributes to phosphorylation of Ser55, they are not a direct demonstration of AURKA-mediated phosphorylation.

To test if AURKA directly phosphorylates Ser55, an in vitro phosphorylation assay was done with recombinant bonsai Ndc80 complex (Ciferri et al., 2008) and purified AURKA. When incubated with the bonsai Ndc80 complex in phosphorylation buffer, AURKA efficiently phosphorylated Ser55 (Figure 4.8C). Finally, to examine the spatial contribution of AURKA activity to phosphorylation of Ndc80-Ser55, the CENP-E inhibitor (Wood et al., 2010) GSK923295 was used to generate polar and aligned kinetochores in HeLa cells in the presence and absence of MLN8237 (Figure 4.8D). In agreement with the S2 cell findings, polar kinetochores were more phosphorylated than aligned/away from the pole kinetochores and the polar bias in phosphorylation was lost when cells were treated with 300 nM MLN8237 (Figure 4.8E). While these findings do not exclude a role for AURKB in phosphorylating Ndc80-Ser55 or other kinetochore substrates in the vicinity of spindle poles, taken together, the data do demonstrate that AURKA can directly phosphorylate Ndc80-Ser55, and that AURKA activity contributes to phosphorylation of this residue in HeLa cells.

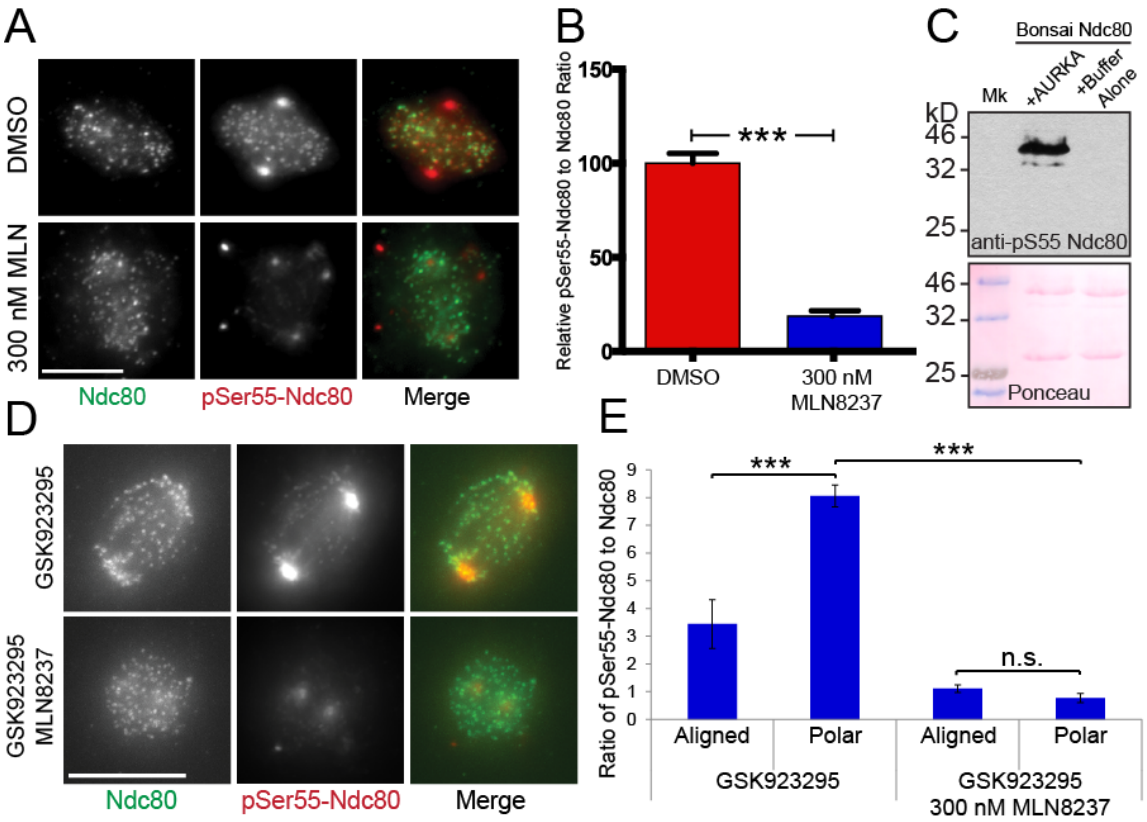

Figure 4.8. AAK phosphorylates the N-terminal tail of Ndc80/Hec1 in human cells.

(A) Representative images of control (DMSO) and AAK inhibited (300 nM MLN8237) HeLa cells stained for pSer55-Ndc80 (red) and Ndc80 (green). (B) Mean values of pSer55-Ndc80 to Ndc80 ratios for DMSO; n = 280 kinetochores from 14 cells, and 300 nM MLN; n = 275 kinetochores from 12 cells. (C) An in vitro phosphorylation assay with purified Ndc80 bonsai complex plus and minus purified AAK blotted for anti-pSer55. AAK directly phosphorylates Ndc80 in vitro. (D) Representative images of GSK923295-treated HeLa cells plus and minus MLN8237 stained for pSer55-Ndc80 (red) and Ndc80 (green). (E) Polar kinetochores are more phosphorylated than aligned kinetochores in GSK923295-treated cells and the polar bias in Ser55 phosphorylation is lost in the presence of MLN8237. Mean values of pSer55-Ndc80 to Ndc80 ratios from 4 independent experiments for GSK923295; aligned, n = 408 kinetochores from 68 cells; polar, n = 239 kinetochores from 68 cells; and 3 independent experiments for GSK923295 + MLN 8237; aligned, n = 465 kinetochores from 55 cells; polar, n = 207 kinetochores from 55 cells. Error bars are SEM. Scale bars are 10 μm. Two-tailed p-values of Student's t-test are reported: not significant (n.s.) p-value > 0.05, * p-value < 0.05, ** p-value < 0.005, *** p-value < 0.0005.

4.3 Discussion

While it has been postulated that AURKA could create a kt-MT attachment destabilizing environment near spindle poles (Godek et al., 2015), it has not been demonstrated experimentally. Here we directly test this hypothesis and our findings support the existence of a pole-centered AURKA phosphorylation gradient that contributes to error correction and counters the potential side-effects of elevated PEFs. We envision that superimposed PEF and AURKA gradients create a balance of activities near spindle poles that promotes error correction, congression, and biorientation resulting in a spatiotemporal path from mal- to bioriented chromosomes (Figure 4.9). First, as an erroneous attachment moves poleward it may become stabilized by progressively higher levels of opposing PEFs. Second, at some distance from the pole, the PEF effect is countered by an AURKA gradient that phosphorylates attachment factors such as the Ndc80 complex. Third, AURKA facilitates congression by biasing CENP-E activity, which has been shown to be phospho-regulated near spindle poles by Aurora kinases (Kim et al., 2010), towards the mid-spindle and by allowing PEFs to push chromosomes away from poles. Note that, in this model, production of an unattached kinetochore(s) by AURKA is not only a prerequisite for biorientation, but also permits PEFs to congress chromosomes without generating unwanted tension at incorrect attachments.

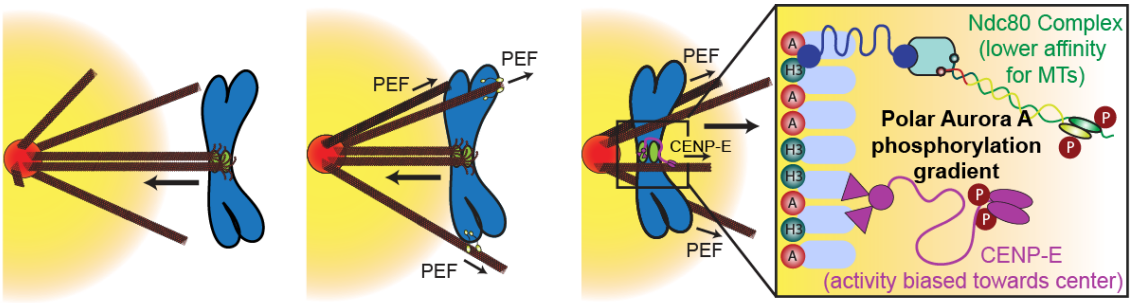

Erroneous attachments (example syntelic) move poleward.

Opposing PEFs stabilize erroneous attachments.

An Aurora A gradient mediates error correction by phosphorylating the Ndc80 complex and licenses congression by PEFs and CENP-E.

Figure 4.9. A spatiotemporal model for the path from maloriented to bioriented chromosomes.
As a syntelic attachment moves poleward it becomes stabilized as it encounters increasing PEFs until encountering the AAK phosphorylation gradient. AAK mediates error correction by phosphorylating kt-MT attachment factors such as Ndc80/Hec1 at Ser55. The AAK gradient also facilitates congression by biasing CENP-E activity towards the mid-spindle and by allowing PEFs to push chromosome arms away from the poles without stabilizing syntelic attachments.

Both the CEN- and pole-based pathways are spatial positioning phenomena with the CEN-based system depending on positioning of kinetochore targets relative to AURKB, and the pole-based pathway relying on spatial positioning of kinetochores relative to spindle poles and AURKA. Although both error correction pathways likely share common targets (e.g. Ndc80/Hec1), we view the CEN-based pathway as kinetochore-intrinsic because the correction machinery (AURKB) localizes to the kinetochore region while the pole-based pathway is kinetochore-extrinsic since the correction machinery is primarily enriched outside the kinetochore region at the spindle poles/centrosomes. There may be orders of magnitude difference in the working distances of the CEN- and pole-based systems as changes in spatial separation occur on the nanometer (Liu et al., 2009; Maresca and Salmon, 2009; Suzuki et al., 2014; Uchida et al.,

2009; Wan et al., 2009; Welburn et al., 2010) and micrometer scale (Lampson et al., 2004) respectively. It will be worthwhile to characterize how the working distance of the pole-based AURKA gradient is defined. While *Drosophila* TPX2 does not regulate AURKA (Goshima, 2011), in other organisms TPX2, which localizes AURKA to spindle poles (Kufer et al., 2002) and activates its kinase activity (Eyers et al., 2003; Tsai et al., 2003), may delineate and amplify an AURKA gradient (Greenan et al., 2010). Regardless of the effective range of AURKA activity, we propose that a key difference between the two pathways is that tension opposes CEN-based error correction while the pole-based pathway is regulated, not by tension, but by positioning kinetochores within the spindle relative to the poles. The pole-based error correction pathway appears to be conserved in meiotic cells as a concurrent study using mouse oocytes found that AURKA activity contributes to destabilizing kt-MT attachments near spindle poles (Chmatal et al., 2015).

It is imperative that mal-oriented chromosomes near spindle poles are corrected because, whereas only a fraction of merotelic kinetochores at the metaphase plate results in chromosome mis-segregation (Thompson and Compton, 2011), mitotic progression in the presence of polar chromosomes would inevitably lead to aneuploidy. Furthermore, we view the consequences of inhibiting AURKA-mediated error correction not merely as more subtle than the effects of AURKB inhibition, but as more insidious. While catastrophic failure in error correction, like that seen following potent AURKB inhibition, would lead to massive and, most likely, lethal aneuploidy, the presence of comparatively low

numbers of “pinned” polar chromosomes when the AURKA pathway is compromised would increase the frequency of single chromosome mis-segregation events and be more likely to yield viable aneuploid cells. Our findings support the conclusion that an AURKA phosphorylation gradient contributes to correcting such hazardous polar attachments before cells divide.

.

4.4 Materials and Methods

4.4.1 Cell culture and drug treatments

Drosophila S2 cells were cultured at 24°C in Schneider's media (Life Technologies) supplemented with 10% heat-inactivated fetal bovine (FBS) serum (Life Technologies) and 0.5x antibiotic-antimycotic cocktail (Life Technologies). Drugs and/or DMSO controls were used as indicated through the manuscript at the following concentrations: 5μM MG132 (Sigma-Aldrich), 1μM vinblastine (Sigma-Aldrich), 40μM binucleine 2 (Sigma-Aldrich), 125 nM MLN8237 (Selleck Chemicals), 25μM colchicine (Sigma-Aldrich).

PtK1 cells were grown in HAM's F-12 media (Life Technologies) supplemented with 5% Sodium Pyruvate (Life Technologies), 1% antibiotic-antimycotic mixture (Life Technologies), and 10% fetal bovine serum (Gibco), and maintained at 37°C and 5% CO_2 in a humidified incubator. For experiments, cells were grown on sterilized acid-washed coverslips inside 35 mm Petri dishes for 48 hours before fixation. For AAK inhibition, MLN8054 was diluted in fresh media at a final concentration of 1 μM and this solution was used to replace the culture media 45 minutes prior to fixation.

HeLa Cells were maintained in DMEM (Lonza) supplemented with 10% FBS, penicillin/streptomycin (Gibco) at 37°C in a humidified atmosphere with 5% CO2. HeLa cells were incubated for 1.5 hours with drugs at the following concentrations: 300 ng/ml nocodazole, 2 μM ZM447439, 300 nM MLN8237.

4.4.2 Generation of S2 cell lines

S2 cells expressing NOD-mCherry and Ndc80-GFP were generated according to previous work (Cane et al., 2013). The *Drosophila* Aurora A gene (CG3068) was amplified from cDNA clone LD16949 with a 5' SpeI site and 3' EcoRI site. The product was inserted into the multiple cloning site of a pMT/V5 His-B vector (Life Technologies) containing the GFP gene and a stop codon between the EcoRI and SacII sites.

The FHA2 domain and the Aurora substrate sequence was amplified from human Mis12-targeted Aurora B FRET sensor (gift from Michael Lampson, Addgene plasmid #45231) with 5'SpeI site and 3' NotI site, and inserted into a pMT/V5 His-B vector (Life Technologies) flanked by mTurquoise2 and mVenus to generate the Aurora sensor. The Threonine in the recognition peptide was replaced with Alanine to generate the non-phosphorylatable FRET sensor. For targeting to the kinetochore, the FRET sensor was amplified using primers flanking the fluorophores (due to high sequence identity between mTurquoise2 and mVenus) with 5' EcoRI and 3' SacII sites and ligated into pMT/V5 His-B vector (Life Technologies) containing N-terminal TagRFP-T-tagged Mis12 under the control of its endogenous promoter. The *Drosophila* Mis12 gene (CG18156) and promoter sequences were each amplified from genomic DNA and cloned with TagRFP-T into a pMT-V5 His-B vector as follows: TagRFP-T was inserted between the KpnI and SpeI sites before inserting the Mis12 promoter at the KpnI site, the Mis12 gene was cloned between the SpeI and EcoRI sites. See Table I for primer sequences.

All cell lines were generated by transfecting DNA constructs using the Effectene Transfection Reagent system (QIAGEN) following manufacturer's instruction, with an addition of 1mL of Schneider's media (Life Technologies) with 10% FBS 1 day after transfection. Cells were checked for fluorescence protein expression and made stable with addition of Blasticidin and/or Hygromycin (Life Technologies).

4.4.3 Production of double-stranded RNAs (dsRNAs)

DNA templates for CENP-meta (CG6392) and Aurora A (CG3068) containing ~500bp of complementary sequence flanked by T7 promoter sequences were generated by PCR. dsRNAs were synthesized overnight at 37°C from the DNA templates using the T7 RiboMax Express Large Scale RNA Production System (Promega). For RNAi experiments, media from semi-adhered cells at 25% confluence in 10mm tissue culture dishes was removed and replaced with 1 mL of serum-free Schneider's medium containing a total of ~20µg dsRNA. After 1 hour, 1 mL of fresh Schneider's with 10% FBS was added to the dishes and incubated for 2-4 days at 24°C. See Table 1 for target sequences.

4.4.4 FRET imagining analysis

Cells were treated with 5µM MG132 in a tissue culture dish for 1 hour, followed by addition of 1µM vinblastine (Sigma-Aldrich) and/or 40µM binucleine 2 (Sigma-Aldrich) or an equal volume of DMSO for controls. Cells were allowed to adhere to acid-washed, concanavalin A (Sigma-Aldrich) coated coverslip (Corning) for exactly 1 hour, then assembled into a rose chamber containing Schneider's media with the appropriate drugs or solvent control and subjected to imaging at

24°C. Cells were imaged for a maximum of 1 hour on a TiE inverted microscope (Nikon) equipped with an iXON EMCCD camera (Andor Technology) using a 100x 1.4 NA Plan Apo violet-corrected series differential interference contrast objective (Nikon). Metamorph software (Molecular Devices) was used to control the imaging system. Mitotic cells were identified and the best focal plane was determined in the RFP channel. Sequential images of mTurquoise2, mVenus, and FRET (ECFP excitation, EYFP emission) were taken with equal exposure times. Background-corrected fluorescence intensities for mTurquoise2 and FRET were measured in Metamorph software using region-in-a-region background subtraction as previously described (Maresca and Salmon, 2009). The reported emission ratio represents the ratio of the background corrected FRET signal over the background corrected mTurquoise2 signal.

4.4.5 FRAP

An ~2-3 μm^2 region around the GFP-Aurora A signal was bleached at the centrosome with a 5-10 second pulse from a Micropoint laser (Andor Technology) using the 481-nm dye cell containing Coumarin 440 dye. Images were then acquired every 5 seconds for 100 seconds. The fluorescence intensities of the bleached regions were measured and corrected for photobleaching over time using Metamorph software (Molecular Devices). To determine the $t_{1/2,}$ the recovery data was fit with a hyperbolic function, y = (x*m2)/(m1+x).

4.4.6 PEF assay

S2 cells expressing Ndc80-GFP and inducible NOD-mCherry alone or in combination with inducible Aurora A-GFP were treated with 500μM $CuSO_4$ for 6-18 hours to induce expression. For AAK RNAi experiments, cells expressing Ndc80-GFP and NOD-mCherry were subjected to RNAi for 4 days. At day 3, cells were treated with $CuSO_4$ to induce NOD-mCherry expression. All PEF assay imaging and quantitative analyses were performed as previously described (Cane et al., 2013). Cells were imaged on a TE300 microscope stand (Nikon) equipped with a CSU10 spinning disk confocal head (Yokogawa) attached to a cooled charge-couple device Orca ER camera (Hamamatsu) using a 100x 1.4 NA Plan Apochromat (Apo) differential interference contrast objective.

4.4.7 Immunostaining and fluorescence microscopy

S2 cells were allowed to adhere to acid-washed concanavalin A (Sigma-Aldrich) for 1 hour before being rinsed with BRB80 and then fixed with 10% paraformaldehyde for 10 minutes. Cells were then permeabilized with PBS containing 1% Triton X-100 for 8 minutes, rinsed three times with PBS plus 0.1% Triton X-100, and blocked with boiled donkey serum for 60 minutes. All primary antibodies were diluted in boiled donkey serum. Anti-Phospho-Aurora A/B/C (Rabbit mAb #2914 – Cell Signaling Technology) and anti-Phospho-Aurora A (Rabbit mAb #3079 Cell Signaling Technology) were diluted 1:1000, DM1α (anti-tubulin antibody; Sigma-Aldrich) at 1:1000, anti-Ndc80 (Maresca Lab) at 1:100 to a final concentration of 2 μg/ml. All secondary antibodies (Jackson ImmunoResearch Laboratories, Inc.) were diluted 1:200 to a final concentration

of 3 μg/ml in boiled donkey serum. After secondary treatment, coverslips were washed two times with PBS plus 0.1% Triton X-100, followed by incubation with DAPI (1:1000) at a final concentration of 1 μg/ml for 5 minutes, and two additional washes. Cover slips were sealed in mounting media containing 20mM Tris, pH 8.0, 0.5% N-propyl gallate, and 90% glycerol.

Fixed S2 cells were imaged on two different systems: (1) a TiE inverted microscope (Nikon) equipped with Orca R2 camera (Hamamatsu) using a 100x 1.4 NA Plan Apo violet-corrected series differential interference contrast objective (Nikon), and (2) a TiE inverted microscope (Nikon) coupled with A1R laser scanning confocal system (Nikon) using a 60x 1.4 NA Plan Apo objective (Nikon). Metamorph software (Molecular Devices) and Elements (Nikon) were used to control the imaging systems, respectively. Three- or four- colour Z series consisting of ~30 planes at 0.2μm intervals were acquired for GFP, dsRED, Cy5 (where appropriate), and DAPI channels. Equivalent exposure conditions were used between control and drug-treated conditions. Ratio fluorescence intensities of region-in-a-region background corrected phospho-Aurora B and phospho-Aurora A to DAPI and centrosomes, respectively, were done similar to previous work (Maresca and Salmon, 2009).

PtK1 cells were rapidly rinsed in 1x PHEM buffer (60mM Pipes, 25mM HEPES, 10mM EGTA, 2mM $MgSO_4$, pH 7.0), and incubated in ice-cold 95% Methanol with 5mM EGTA for 5 min first and then again for 20 min at -20^{o}C. Subsequently, cells were washed in PBS, and then blocked in 10% boiled goat serum for 1 h at room temperature. The coverslips were then incubated overnight

at 4°C in primary antibodies diluted in 5% boiled goat serum. Cells were finally washed in PBST (PBS with 0.05% Tween 20), incubated in secondary antibodies diluted in 5% boiled goat serum for 1 hour at room temperature, washed again, stained with DAPI, and mounted in an antifade solution containing 90% glycerol and 0.5% *N*-propyl gallate. Primary antibodies were diluted as follows: ACA (human anti-centromere antigen, Antibodies Inc.), diluted 1:100; mouse anti-α-tubulin (DM1A, Sigma-Aldrich), diluted 1:500. Secondary antibodies were diluted as follows: X-Rhodamine goat-anti–human (Jackson ImmunoResearch Laboratories, Inc.), diluted 1:100; Alexa 488 goat-anti–mouse (Molecular Probes), diluted 1:400.

PtK1 Cells were imaged with a Swept Field Confocal system (Prairie Technologies) on a Nikon Eclipse TE-2000U inverted microscope. The microscope was equipped with a 100× 1.4 NA Plan-Apochromatic phase–contrast objective lens, phase–contrast transillumination, transmitted light shutter, and automated ProScan stage (Prior Scientific). Illumination was achieved via a four-line monolithic high power laser module with AOTF (Agilent Technologies). Digital images were acquired with an HQ2 CCD camera (Photometrics). Image acquisition, shutter, Z-axis position, laser lines, and confocal system were all controlled by NIS Elements AR software (Nikon). Z-series optical sections through each cell analyzed were obtained at 0.6 µm steps.

HeLa cells were plated on 18-mm glass coverslips coated with poly-L-lysine (Sigma-Aldrich) and immunostained as previously described (Kline et al., 2006) using antibodies against mouse anti-CENP-A (Abcam), and rabbit anti-

Phospho-Hec1 pSer55 (Pierce) per the manufacturer's instructions. HeLa cell images were acquired on a DeltaVision Core deconvolution microscope (Applied Precision) equipped with a CoolSnap HQ2 CCD camera. Thirty Z-sections were acquired at 0.2μm steps using a 1.3 NA Olympus U-PlanApo objective without binning. Equivalent exposure conditions were used between controls and drug-treated cells. To quantify fluorescent intensity, individual kinetochores were selected from projections (selected based on co-localization with CENP-A), and the integrated intensity was determined after subtracting the background fluorescence measured from adjacent regions of the cell using Metamorph software. Fluorescent levels at kinetochores were normalized with respect to control cells.

4.4.8 PtK1 cell analysis

For analysis of mitotic index, mitotic staging, and mitotic defects, cells were examined visually and data recorded. In each experiment, at least 1,000 cells were examined when recording mitotic indices, at least 200 mitotic cells for mitotic staging, and at least 100 prometaphases and 100 anaphases for mitotic defects. For kinetochore position within the spindle, prometaphase cells were imaged and then analyzed as follows: the pole-to-pole and kinetochore-to-pole distances were measured for each cell analyzed. Kinetochore-to-pole distances were then represented as a percentage of the pole-to-pole distance. Merotelically attached kinetochores were identified by scrolling through the Z-axis to visualize kinetochores bound to microtubule bundles oriented in opposite directions. The focal planes above and below the kinetochore were then analyzed to exclude

cases in which a microtubule bundle ran past a kinetochore rather than ending on it.

4.4.9 Western Blotting

A total of 10µg of protein was loaded into a 10% SDS-PAGE gel, run out, and transferred to a nitrocellulose membrane on the Trans-Blot® Turbo™ transfer system (Bio-Rad Laboratories) using the preprogrammed “MIXED MW” 7 minute protocol. All antibodies were diluted in TBS with 0.1% Tween and 5% milk. The membrane was first incubated with anti-Aurora A (gift from Marcin Przewloka and David Glover, University of Cambridge, UK) at 1:5000, followed by DM1α (anti-α-tubulin antibody; Sigma Aldrich) at 1:5000. Rabbit and mouse HRP secondary antibodies (Jackson ImmunoResearch Laboratories, Inc.), diluted at 1:5000, were used in conjunction with their respective primaries and visualized with a GBox system controlled by GeneSnap software (Syngene).

Table 4.1 Primers used in this chapter.

	RNAi Primer Sequence (5'→3')
CENP-meta RNAi Forward	TAATACGACTCACTATAGGGGTTAGAGAGCGTTGAATCTGCC
CENP-meta RNAi Reverse	TAATACGACTCACTATAGGGCGTCAAAATCGGAGCTTATACC
Aurora A RNAi Forward	TAATACGACTCACTATAGGGATGTCCCATCCGTCTGACCA
Auror A RNAi Reverse	TAATACGACTCACTATAGGGTTGCCAAACTTGCCCCGTCC

	Cloning Primers (5'→3')
Mis12 Forward	CCACTAGTATGGACTTCAATAGCCTAGC
Mis12 Reverse	GGGAATTCATCAGTCTCCTTCTTTAT
Mi12 Promoter Forward	GCG GTA CCA TTT GCT TCC TTT GTT TGT T
Mis12 Promoter Rev	GGGGTACCTATGACAGTTAACAACAATA
tagRFP-T Forward	ATTGGTACCATGGTGTCTAAGGGCGAAGA
tagRFP-T Reverse	ACGGGTACCCTTGTACAGCTCGTCCATGC
Aurora A Forward	GGACTAGTATGTCCCATCCGTCTGACCA
Aurora A Reverse	CGGAATTCCTGCGTGTGCGCCAGGATCC
FHA Forward	ATACTAGTAAGGGTAATGGTAGGTTTTT
FHA Reverse	ATGCGGCCGCCACCACCGATGGCCACGGTGC
FRET Forward	CTGAATTCCAAGTTTCAATTGCAAAT
FRET Reverse	GGGATAGGCTTACCTTCGAA

CHAPTER 5

AURORA A KINASE AMPLIFIES A MIDZONE PHOSPHORYLATION GRADIENT TO PROMOTE HIGH-FIDELITY CYTOKINESIS

This work was completed with the guidance of Thomas J. Maresca, in collaboration with Julia Torabi. J.T. was a very hard working undergraduate student in the lab that I trained since her freshman year. We worked together to develop all the initial assays. I did all the TIRF imaging and completion of the paper. This chapter is published in *Biological Bulletin* in 2016 (Ye et al., 2016b), and partially in Julia's senior thesis.

5.1 Introduction

Mitosis is the process by which a cell divides its duplicated genetic material into two daughter cells. Equal segregation of the DNA is required for cell viability, and, thus, it is critical that this process is orchestrated flawlessly every time. Cytokinesis is achieved by an actin-myosin contractile ring that physically divides the cell into two daughter cells following separation of the sister chromatids during anaphase. Proper positioning of the contractile ring and, hence, the cleavage furrow is critically important for cytokinesis, but current understanding of the cues that spatially determine where the furrow forms is incomplete.

The aurora family of proteins is a group of mitotic serine/threonine kinases that regulate many aspects of cell division (Carmena et al., 2009; Hochegger et al., 2013). aurora A kinase (AAK) and aurora B kinase (ABK), the two members found in *Drosophila melanogaster,* have highly conserved C-terminal kinase domains that phosphorylate many of the same substrates. However, their

cellular functions are distinct and dictated by their different cellular localizations, which are determined by the divergent N-terminal regulatory domain (Li et al., 2015). Aurora B kinase is part of a multi-subunit protein complex called the chromosomal passenger complex (CPC). Prior to anaphase, the CPC is highly enriched at the inner centromere and ABK activity contributes to spindle and kinetochore assembly, spindle assembly checkpoint signaling, and error correction (Emanuele et al., 2008; Lampson and Cheeseman, 2011; Moutinho-Pereira et al., 2013; Tanaka et al., 2002). Aurora B kinase activity is essential for proper cytokinesis (Adams et al., 2001; Echard et al., 2004; Eggert et al., 2004; Smurnyy et al., 2010) and, at onset of anaphase, the CPC complex relocalizes to the spindle midzone (Adams et al., 2000), an area comprised of stable, overlapping microtubules (MTs). The midzone-associated CPC generates an activity gradient (Fuller et al., 2008; Tan and Kapoor, 2011) that helps ensure complete sister chromatid separation (Afonso et al., 2014), and that is proposed to contribute to positioning of the cleavage furrow (Adams et al., 2000; Tan and Kapoor, 2011; Terada, 2001)). Aurora A kinase is required for centrosome maturation, separation, and function (Giet et al., 2002; Glover et al., 1995; Hannak et al., 2001), proper kinetochore-MT attachment (Bakhoum et al., 2014; Barisic et al., 2014; Chmatal et al., 2015; Ye et al., 2015), chromosome segregation (Hégarat *et al.,* 2011), MT nucleation (Scrofani et al., 2015), and robust assembly of midzone MTs (Lioutas and Vernos, 2013; Reboutier et al., 2013).

While it is clear that MTs are required for positioning of the cleavage furrow (Rappaport, 1971), MT-dependent and MT-independent mechanisms have been proposed to contribute to faithful cytokinesis (Alsop and Zhang, 2003; Canman et al., 2003; Field et al., 2015; Foe and von Dassow, 2008; Murthy and Wadsworth, 2008; Nguyen et al., 2014; Rodrigues et al., 2015). Broadly speaking, two major models are evoked to explain how cells define where the cleavage furrow is positioned during cytokinesis. Equatorial stimulation holds that a positive signal promotes cortical contractility through activation of myosin in between the spindle poles, while polar and/or astral relaxation posits that a signal coming from the vicinity of the spindle poles inhibits contractility, causing the polar cortex to relax. While there is evidence that astral MTs in the polar region contribute to polar relaxation (Murthy and Wadsworth, 2008), recent work suggests that the signal does not require astral MTs, but rather is mediated by a kinetochore-derived phosphatase gradient (Rodrigues et al., 2015). Equatorial stimulation depends on signals from both the midzone, which is enriched for essential cytokinesis regulators, including the CPC (Glotzer, 2005; Nguyen et al., 2014), and an “astral” stimulation signal that requires a subpopulation of stable MTs in the vicinity of the furrow site (Canman et al., 2003; Field et al., 2015; Foe and von Dassow, 2008). Thus, three potentially redundant pathways regulate the formation and positioning of the cleavage furrow: 1) polar relaxation, 2) midzone stimulation, and 3) astral stimulation. Here, we apply a variety of live-cell imaging techniques in *Drosophila* S2 cells to explore the contribution of each of these pathways to successful cytokinesis.

5.2 Results

To determine if aurora A kinase (AAK) plays a post-metaphase role in *Drosophila* S2 cell division, AAK was knocked down by RNA interference (RNAi), and microtubule (MT) intensity in the spindle midzone during late anaphase was quantified (Fig. 5.1A–C). Consistent with previous reports in other cell types (Lioutas and Vernos, 2013; Reboutier et al., 2013), a 34% decrease in MT midzone population was observed in AAK RNAi-depleted cells compared to control cells. Similar to the AAK-depleted conditions, cells treated with a 125 nM concentration of the inhibitor, MLN8237—which specifically inhibits AAK in *Drosophila* S2 cells (Ye et al., 2015), resulting in a loss of phosphorylated AAK (pAAK) from centrosomes (Fig. 5.2A)—exhibited a 40% decrease in midzone MT intensity compared to DMSO-treated cells (Fig. 5.2B-F). The observed decrease in midzone MT density in late anaphase following AAK depletion or chemical inhibition may be a result of inhibiting aurora B kinase (ABK) as it relocalizes to the overlapping central spindle MTs after anaphase. To examine if the observed results were due to mislocalizing or inhibiting ABK, levels of active phosphorylated ABK (pABK) at midzones were quantified in control and AAK-inhibited conditions. When normalized to the control levels, pABK did not exhibit a significant change at the midzone in either AAK knockdown (Fig. 5.1D) or MLN8237-treated cells (Fig. 5.2D) compared to the control conditions. Thus, while the MT intensities were significantly decreased relative to controls in the absence of AAK activity, the total level of midzone pABK was unaffected by either chemical inhibition of AAK or its depletion. It is noteworthy that while the

total amount of pABK did not change, when normalized to the midzone tubulin signal, the amount of midzone pABK per MT increased significantly compared to the controls in both AAK-depleted and MLN8237-treated cells (Fig. 4.1E and 4.2E).

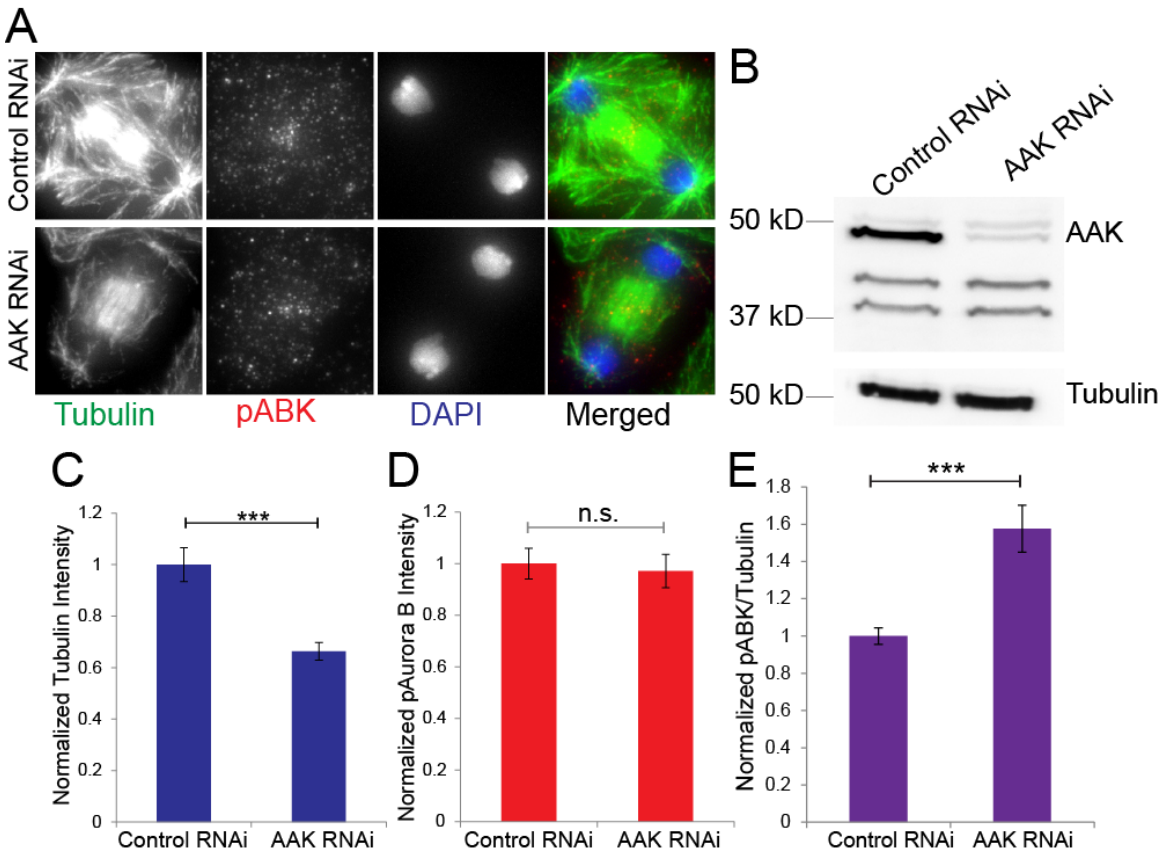

Figure 5.1. Aurora A kinase is required for robust midzone microtubules.
(A) Representative images of control RNAi and AAK RNAi cells, showing a decrease in microtubule (MT) intensity in AAK-depleted cells. (B) AAK can be efficiently depleted from S2 cells, as assayed by Western blot analysis of control RNAi and AAK RNAi cells. Tubulin was used as the loading control. (C) Quantification of midzone MT intensity normalized to control RNAi. Midzone MT density is significantly decreased in late anaphase and/or telophase cells that lack AAK activity. Quantifications are from two independent experiments. Control RNAi, *n* = 62 cells; AAK RNAi, *n* = 70 cells. (D) AAK depletion does not change the total amount of midzone-associated pABK. Quantifications are from two independent experiments. Control RNAi, *n* = 62 cells; AAK RNAi, *n* = 70 cells. (E) AAK depletion leads to more pABK per MT in the central spindle. Quantifications are from two independent experiments. Control RNAi, *n* = 62 cells; AAK RNAi, *n* = 70 cells. Error bars are SEM. Scale bars = 5 *μ*m. Two-tailed Student's *t* tests are reported: not significant (n.s.), $P > 0.05$; ***$P < 0.0005$

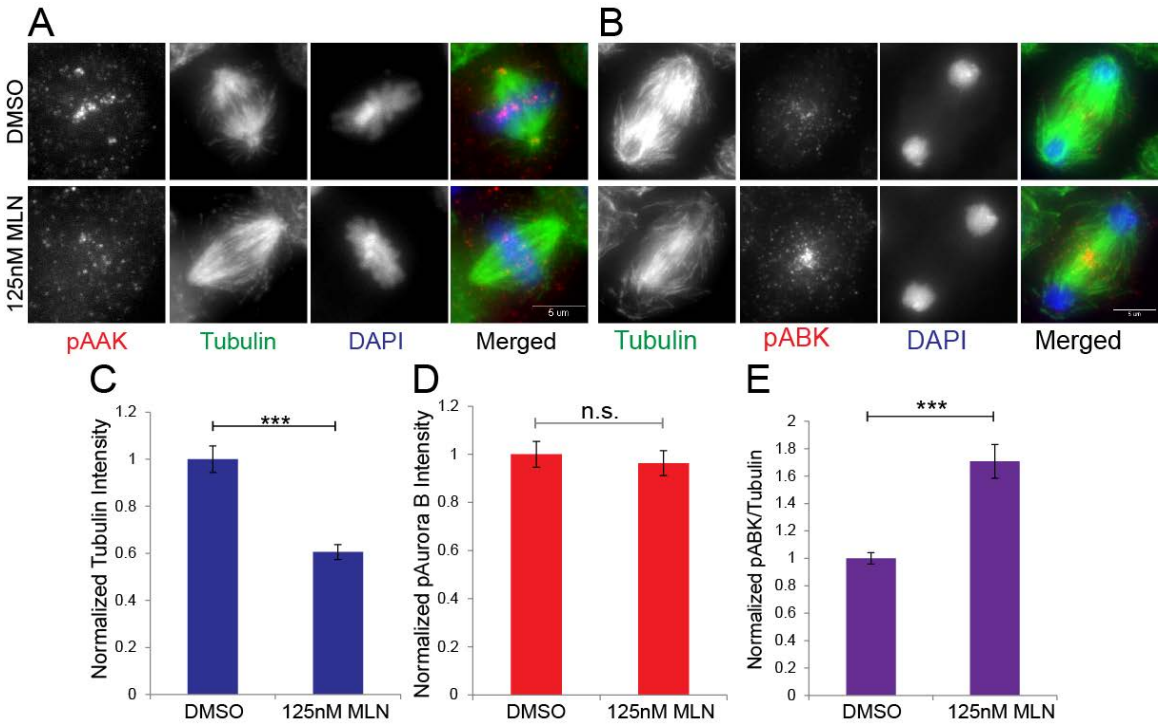

Figure 5.2. AAK inhibition with 125nM MLN8237 phenocopies AAK knockdown.

(A) Representative images of DMSO-treated and 125 nM MLN8237-treated cells, showing a decrease in midzone MT intensity in the AAK-inhibited cell compared to the control cells. (B) Representative images of cells treated with DMSO (top row) or 125 nM MLN8237 (bottom row), stained with anti-pAAK. Cells treated with MLN8237 do not have pAAK staining at centrosomes. We previously demonstrated (Ye et al., 2015) that the apparent centromere staining with the anti-pAAK antibody is due to cross-reactivity with pABK. (C) Cells treated with 125 nM MLN8237 phenocopy AAK-depleted cells, exhibiting decreased MT density in the spindle midzone. Quantifications are from two independent experiments. DMSO, *n* = 77 cells; 125 nM MLN8237, *n* = 77 cells. (D) 125 nM MLN8237 does not decrease total pABK localization to the midzone. Quantifications are from two independent experiments. DMSO, *n* = 77 cells; 125 nM MLN8237, *n* = 77 cells. (E) Cells treated with 125 nM MLN phenocopy cells depleted of AAK, having more pABK per MT. Quantifications are from 2 independent experiments. DMSO, n = 77 cells. 125 nM MLN8237, *n* = 77 cells. Error bars are SEM. Scale bars = 5 *μ*m. Two-tailed Student's *t* tests are reported: not significant (n.s.), $P > 0.05$; ***$P < 0.0005$.

The midzone aurora kinase activity gradient was next investigated. A FRET-based aurora phosphorylation sensor (Fuller et al., 2008; Ye et al., 2015) was generated and targeted to the MTs by fusing it to the MT-associated protein Tau (full-length protein). Expression of the Tau-FRET reporter did not obviously bundle MTs or alter interphase MT dynamics relative to cells in the same imaging chamber that were not expressing the reporter (Table 5.1).

Table 5. 1. Microtubule dynamics are unaffected by expression of Tau FRET reporter.

	No FRET Expression	**FLTau FRET**
Growth Velocity (μm/min)	4.57	4.21
Shrink Velocity (μm/min)	5.56	5.34
Rescue Frequency (s^{-1})	0.014	0.014
Catastrophy Frequency (s^{-1})	0.057	0.06

The sensor is designed such that the FRET ratio decreases when it is phosphorylated by aurora kinases (Fig. 5.3). Cells treated with 125 nM MLN8237, which specifically inhibits AAK activity and has the same effects as AAK knockdown (Fig. 5.1 and 5.2), exhibited a 5% higher FRET emission ratio (Fig. 5.4A and 5.4B). This indicates that substrates are less phosphorylated by the midzone aurora kinase activity gradient when AAK activity is inhibited in S2 cells—despite having normal levels (or even higher levels per MT) of midzone pABK. This finding is consistent with previous work that identified transforming acidic coiled-coil containing protein 3 (TACC3) and p150Glued as midzone AAK substrates in human cells that were less phosphorylated and mislocalized,

respectively, following AAK inhibition (Lioutas and Vernos, 2013; Reboutier et al., 2013). Importantly, the behavior of a non-phosphorylatable FRET sensor was unaffected by MLN8237 (Fig. 5.4C). We posit that the measured decrease in kinase activity must be due to inhibition of AAK, because pABK levels are actually higher per MT in this condition (Fig. 5.1E and 5.2E). Thus, we conclude that AAK amplifies a midzone aurora kinase activity gradient.

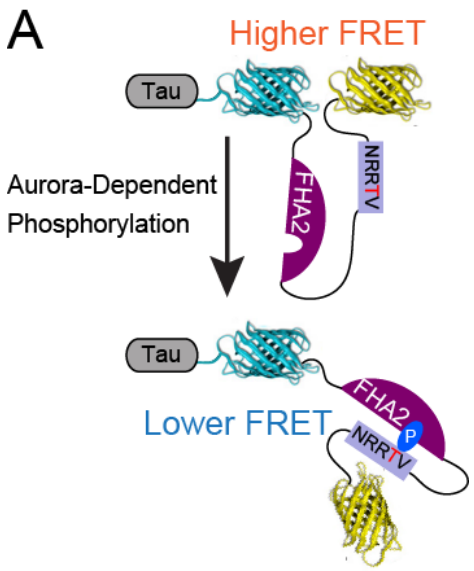

Figure 5.3. Schematic of the microtubule localized FRET based aurora phosphorylation sensor.
Schematic of the MT-targeted FRET-based phosphorylation sensor, highlighting the Threonine (T) residue that would be phosphorylated by aurora kinases. Phosphorylation causes a conformational change to this sensor leading to a decrease in FRET ratio .

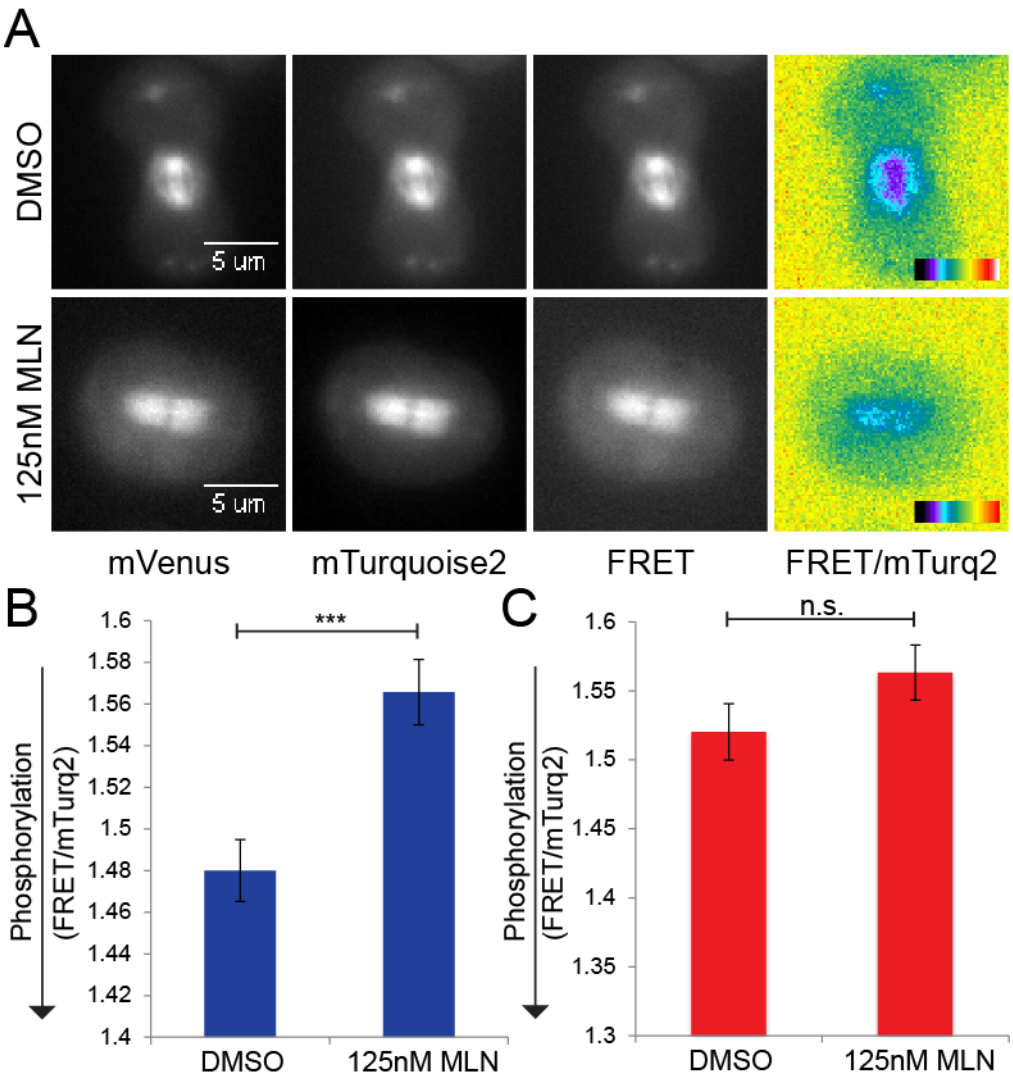

Figure 5.4. Midzone microtubules are less phosphorylated in the AAK defective cells.

(A) Representative images of the FRET reporter experiment quantified in (C). The FRET emission ratio images "FRET/mTurq2" are pseudo-colored with the color wedge spanning ratio values of 1.4–2.4. (C) Cells treated with 125 nM (nM) MLN8237, which specifically inhibits AAK activity, lowers the FRET emission ratio of the sensor at the spindle midzone, indicating that it is less phosphorylated than in DMSO treatments. Quantifications are from three independent experiments. DMSO, *n* = 106 cells; 125 nM MLN8237, *n* = 107 cells. (D) The FRET emission ratio of a non-phosphorylatable version of the sensor, in which the Threonine is mutated to Alanine, is not different between cells treated with DMSO and 125 nM MLN8237. DMSO, *n* = 36 cells; 125 nM MLN8237, *n* = 37 cells. Error bars are SEM. Scale bars = 5 μm. Two-tailed Student's t tests are reported: not significant (n.s.), P > 0.05; ***P < 0.0005.

Where is AAK functionally relevant post-anaphase, during midzone assembly and cytokinesis? While we and others (Berdnik and Knoblich, 2002; Giet et al., 2002; Ye et al., 2015) have described the localization pattern of AAK through *Drosophila* cell division, we more closely examined AAK relative to MTs by imaging cells co-expressing mCherry-tagged AAK and GFP-α-tubulin. Aurora A kinase was highly enriched at centrosomes throughout mitosis and localized to spindle MTs to varying degrees, depending on the level of overexpression, with a tendency to be enriched near spindle poles in low to moderately expressing cells. In cells with the highest levels of AAK overexpression, a slight enrichment of AAK was sometimes observed in the vicinity of kinetochores/centromeres, although not to the extent previously seen in mouse oocytes overexpressing AAK (Chmatal et al., 2015). Aurora A kinase remained enriched at centrosomes throughout anaphase and during cytokinesis, although—even in high-expressing cells—AAK only faintly associated with MTs but was not enriched on midzone MTs (Fig. 5.5A). Aurora B kinase, on the other hand, is highly enriched on midzone MTs, and, when visualized by total internal reflection fluorescence (TIRF) microscopy (Vale et al., 2009), ABK also exhibits MT tip-tracking behavior at onset of anaphase. We next employed TIRF imaging of cells co-expressing mCherry-tagged AAK and GFP-α-tubulin, to determine if AAK exhibited behavior similar to that of ABK (Fig. 5.5B). While AAK was evident at a centrosome that entered the TIRF field during anaphase, it neither tip-tracked nor became enriched on midzone or astral MTs in the cortical region. Thus, we posit that the

midzone-derived aurora kinase activity gradient is amplified largely by a soluble rather than MT-associated pool of AAK.

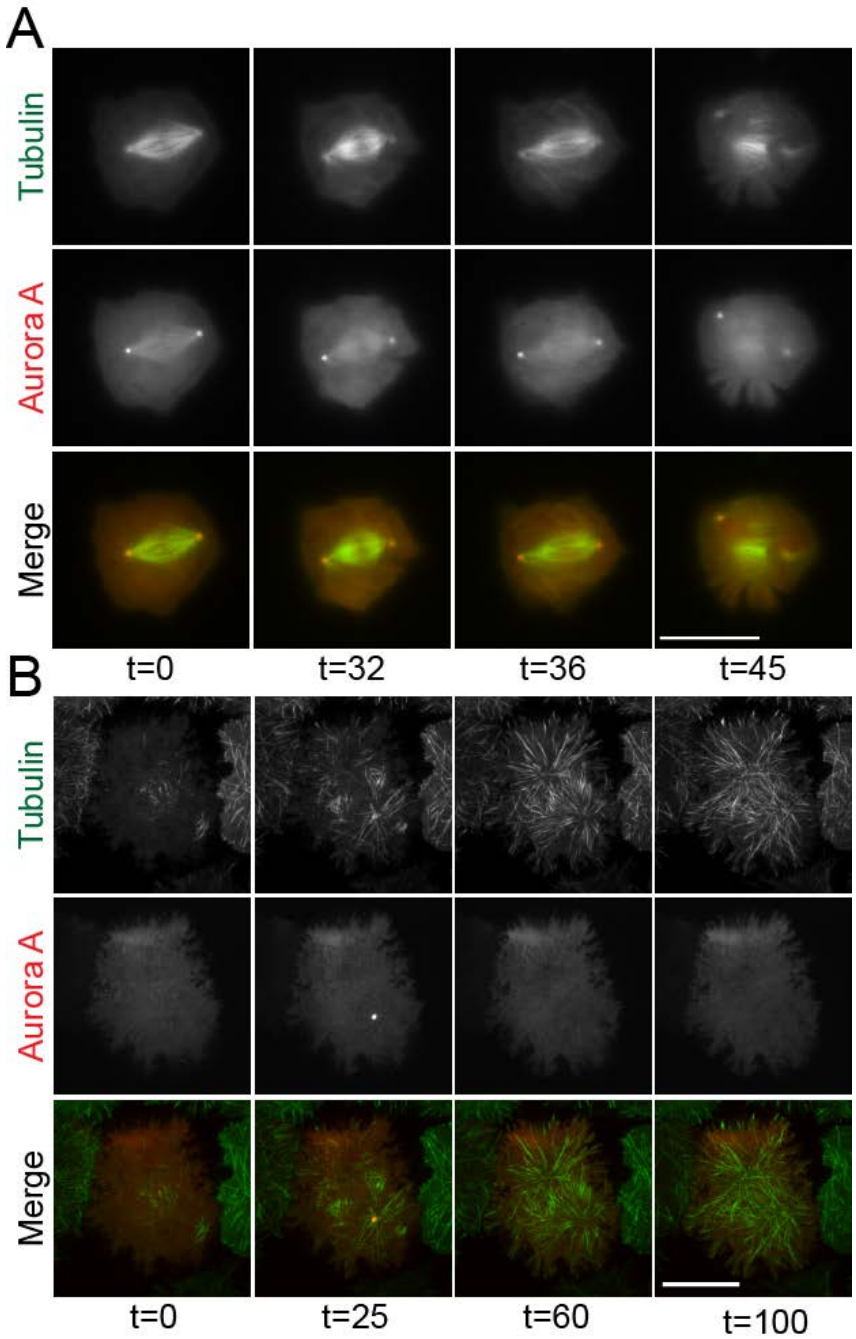

Figure 5.5. Aurora A kinase localizes to the centrosomes.
(A) Still frames from wide-field, time-lapse imaging of a high-expressing AAK-mCherry cell, progressing from metaphase through cytokinesis onset. In the merged images tubulin is green and AAK is red. (B) Still frames from two-color TIRF imaging of an AAK-mCherry cell progressing from metaphase through cytokinesis onset. In the merged images, tubulin is green and AAK is red. Scale bar are 20μm.

Our data indicate that AAK amplifies a midzone phosphorylation gradient to promote robust midzone assembly in *Drosophila* S2 cells. To examine whether the observed defects in midzone assembly impacted furrow formation or assembly of the actin-myosin contractile ring during cytokinesis, myosin dynamics were visualized in living cells expressing GFP-tagged myosin regulatory light chain (MRLC; spaghetti squash in *Drosophila)* and mCherry-α-tubulin by TIRF microscopy. In this image-based assay, cells are allowed to adhere to Concanavalin A, which prevents successful completion of cytokinesis but allows for impressive visualization of myosin at the cortex after anaphase onset (Vale et al., 2009). In accord with previous TIRF imaging of this cell line (Vale et al., 2009), MRLC was lost from the equator and became enriched at the site of the cleavage furrow following anaphase onset. There was no significant difference between DMSO- and MLN8237-treated cells in myosin dynamics at the polar relative to the equatorial regions (Fig. 5.6A and 5.6B). We next employed correlative TIRF-spinning disk confocal imaging on MLN-treated cells to better observe MRLC organization. A field of cells that contained a metaphase cell was imaged by TIRF microscopy for 25 min to capture the metaphase cell progress through anaphase, enrich MRLC in at the equator, and assemble a contractile ring. At that point, the field was imaged by confocal spinning disk microscopy (Fig. 5.7), 0.2-*μ*m confocal z-sections were acquired, and 3D reconstructions were generated for each of the three cells in the field of view (Fig. 5.7). The cell that progressed from metaphase to anaphase had formed a cleavage furrow and assembled a clear ring of MRLC that deformed the upper

part of the midzone (Fig.5.7A). A neighboring cell possessed a midbody, and a small ring of MRLC could be seen around the midbody (Fig. 5.7B). Since the cells had been treated with MLN for several hours at this point, this cell very likely had progressed through cytokinesis in the absence of AAK activity. An interphase cell with MRLC highly enriched at the cortex, contacting the coverslip, was also present in the field of view (Fig. 5.7C). Taken together, the data indicate that loss of AAK activity does not dramatically alter MRLC dynamics or organization during cytokinesis.

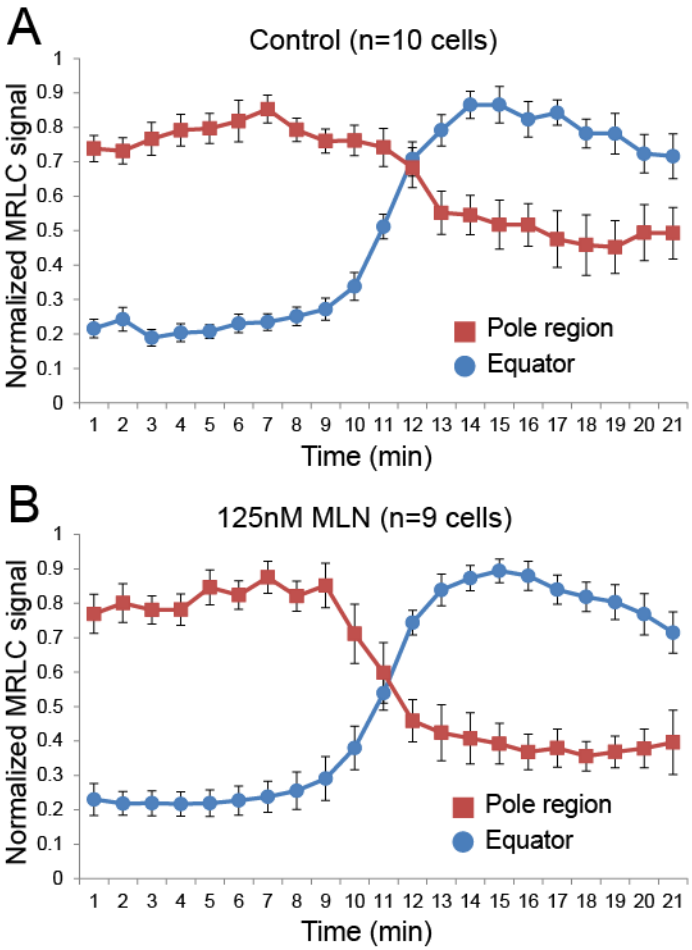

Figure 5.6. MRLC relocolizes to the region of cytokinesis independent of AAK.
(A) MRLC is depleted from the pole region and accumulates at the cell equator during the metaphase to anaphase transition. The half change of myosin intensity at the equator happens, on average, 1 min before the loss of half of the myosin at the pole region. Quantifications are from 10 DMSO-treated cells. (B) Cells treated with 125 nM MLN8237 do not exhibit significant changes in myosin dynamics during cell division relative to control cells, with the exception of one cell that failed cytokinesis. Quantifications are from nine cells. Error bars are SEM.

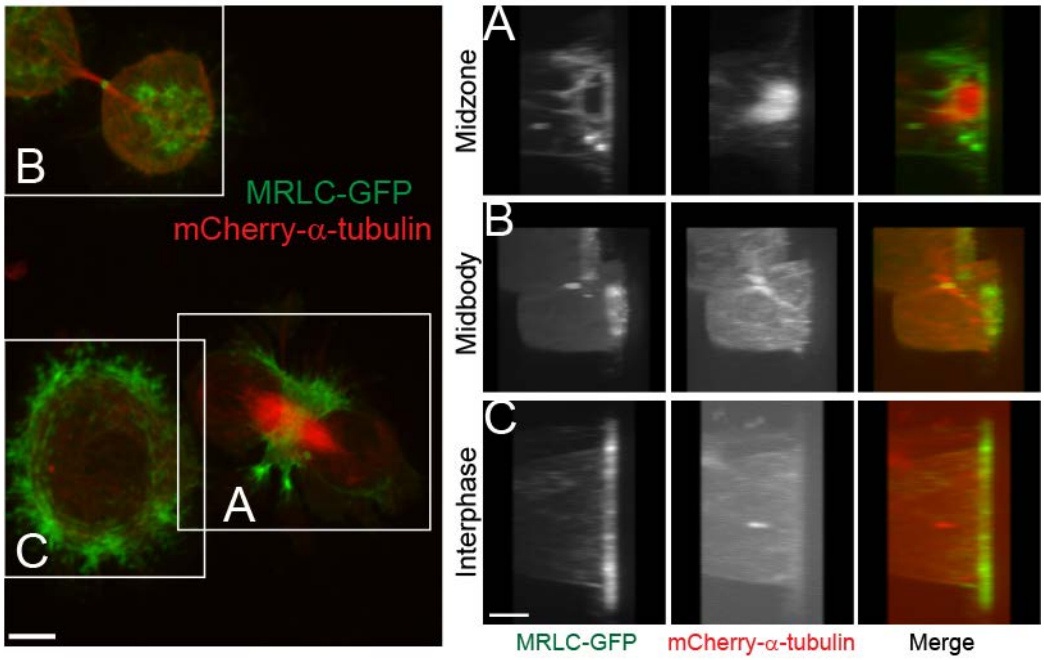

Figure 5.7. 3D reconstitution of MRLC in mitosis.
(A) Maximum-intensity projection of a spinning disk confocal image containing three cells at different stages of the cell cycle. MRLC is green, and tubulin is red. The z-stacks were used to reconstruct 3D images of the regions highlighted in the while boxes. (B) 3D reconstruction of a cell in late anaphase, after MRLC has already accumulated at the cleavage furrow. MRLC at the cell equator is forming a ring around the spindle. (C) 3D reconstruction of cells with a midbody between them. The MRLC has already constricted, but remains a ring around the midbody. (D) 3D reconstruction of an interphase cell. In the merged images MRLC is green, and tubulin is red. Scale bars = 20 μm.

It is widely accepted that aurora B kinase activity is required for cytokinesis. In support of this theory, numerous key cytokinesis regulators have been shown to be ABK targets (Adams et al., 2001; Echard et al., 2004; Eggert et al., 2004; Guse et al., 2005; Nunes Bastos et al., 2013; Smurnyy et al., 2010). Similar to the phenotype associated with compromising critical cytokinesis regulators in *Drosophila,* such as Pavarotti (*Dm* MKLP1) (Adams et al., 1998), large cells are prevalent following treatment with the *Drosophila* ABK-specific inhibitor Binucleine-2 (Bin2) (Eggert et al., 2004). However, as previously described (Moutinho-Pereira et al., 2013), we have observed that Bin2-treated cells fail to fully condense their chromosomes or assemble bipolar spindles. In addition, the spindle assembly checkpoint is severely compromised, leading to rapid mitotic exit in the absence of any semblance of normal mitotic timing or organization. Furthermore, while failure in cytokinesis following depletion of *bona fide* regulators such as Pavarotti results in cells with two comparably sized nuclei, Bin2-treated cells rarely exhibit the typical binucleate phenotype. Rather, these cells have a single, large nucleus or large nuclei with numerous smaller nuclei. Similar to previous observations (Afonso et al., 2014), the addition of Bin2 in early anaphase led to rapid mitotic exit and the formation of a single, large nucleus (Fig 5.8). The fact that this Bin2-treated anaphase cell did not complete cytokinesis was likely due to the consequences of rapid mitotic exit, as well as the positioning of the nucleus in the midzone position. Thus, the pleiotropic effects of globally inhibiting ABK render defects of cytokinesis difficult to interpret. To better isolate the contribution of midzone ABK (mABK), the

Drosophila mitotic kinesin-like protein 2 (MKLP2) homologue, Subito, which localizes chromosomal passenger complex (CPC) to the midzone in numerous model systems, including *Drosophila* (Cesario et al., 2006; Gruneberg et al., 2004; Nguyen et al., 2014), was depleted by RNAi. Subito depletion resulted in a substantial reduction in midzone levels of pABK (Fig. 5.9 A and B). Mislocalizing mABK by Subito depletion did not result in a significant increase in the number of binucleated cells compared to control conditions (Fig. 5.9C). While AAK contributes to the midzone phosphorylation gradient, the frequency of binucleated cells was not increased in MLN-treated cells relative to DMSO controls (Fig. 5.9C). We reasoned that if AAK amplifies the midzone activity gradient to promote cytokinesis, then inhibition of AAK in the absence of mABK would result in a higher frequency of cytokinesis failure. Indeed, MLN-treated cells that were depleted of mABK resulted in a ~4-fold increase in binucleate cells compared to controls (Fig. 5.9C). The additive effect of losing both AAK and mABK activities suggests that the two kinases work together to increase the fidelity of cytokinesis. In the double inhibited cells, the midzone aurora kinase activity gradient is compromised and, while a 4-fold increase in cytokinesis failure is not desirable, most cells manage to complete cytokinesis. Thus, redundant pathways must compensate for the loss of the midzone aurora phosphorylation gradient.

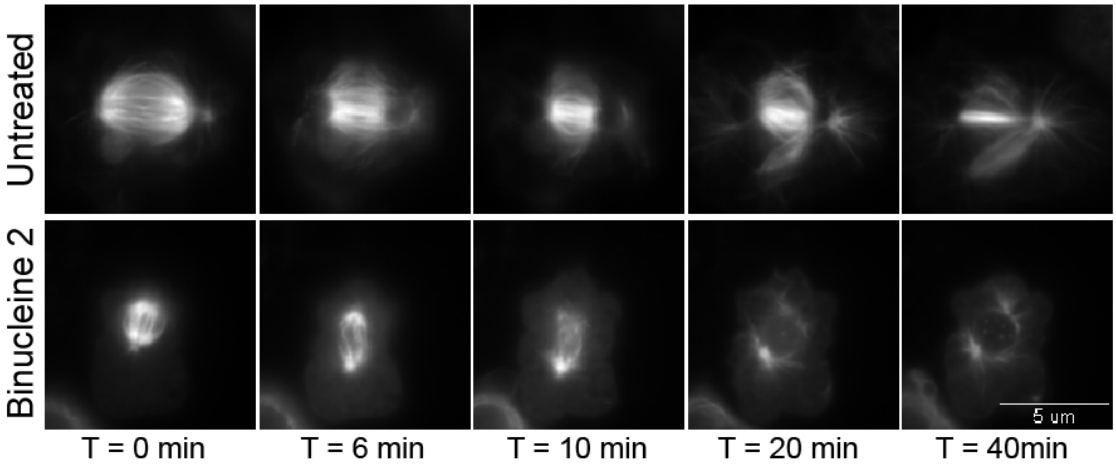

Figure 5.8. Aurora B kinase is required for cytokinesis.
Still frames from wide-field, time-lapse imaging of untreated (top row) and 40 μM binucleine-2-treated S2 cells (bottom row). Scale bar = 5μm. T = 0 represents anaphase onset.

Previous work has shown that a kinetochore-based PP1-Sds22 phosphatase gradient mediates the polar relaxation signal (Kunda et al., 2012; Rodrigues et al., 2015). To inhibit the relaxation gradient and examine its functional redundancy with the equatorial stimulation signal from aurora kinases, Sds22 was depleted from cells alone and in combination with treatments that disrupt the midzone aurora kinase activity gradient. As previously reported (Rodrigues et al., 2015), depletion of Sds22 did not lead to a measurable increase in cytokinesis failure (Fig. 5.9D). Interestingly, cells lacking Sds22, and in which AAK was also inhibited, were no more prone to fail cytokinesis than control cells, while Sds22 depletion combined with loss of the midzone aurora kinase activity gradient were indistinguishable from Subito-depleted cells treated with 125 nM MLN8237 (Fig. 5.9D). Thus, Sds22-dependent polar relaxation is dispensable for proper cytokinesis, even in the absence of the aurora-mediated equatorial stimulation signal. Astral microtubules (MTs), presumably derived from centrosomes, have

been thought to contribute to both polar relaxation (Murthy and Wadsworth, 2008) and equatorial stimulation (Rappaport, 1961). Centrosomin (CNN) was depleted in order to examine the contribution of centrosome-derived astral MTs to cytokinesis and their redundancy with the midzone aurora phosphorylation gradient. In CNN RNAi cells treated with either dimethyl sulfoxide (DMSO) or MLN8237, the percentage of binucleated cells was not different from control cells (Fig. 5.9E). As was the case for Sds22 depletion, CNN depletion in combination with Subito RNAi and 125 nM MLN8237 exhibited the same phenotype as cells lacking mABK and AAK activity (Fig. 5.9C-E). This suggested that centrosomal MTs do not make a major contribution to cytokinesis in *Drosophila* S2 cells, even when the midzone aurora kinase activity gradient is compromised.

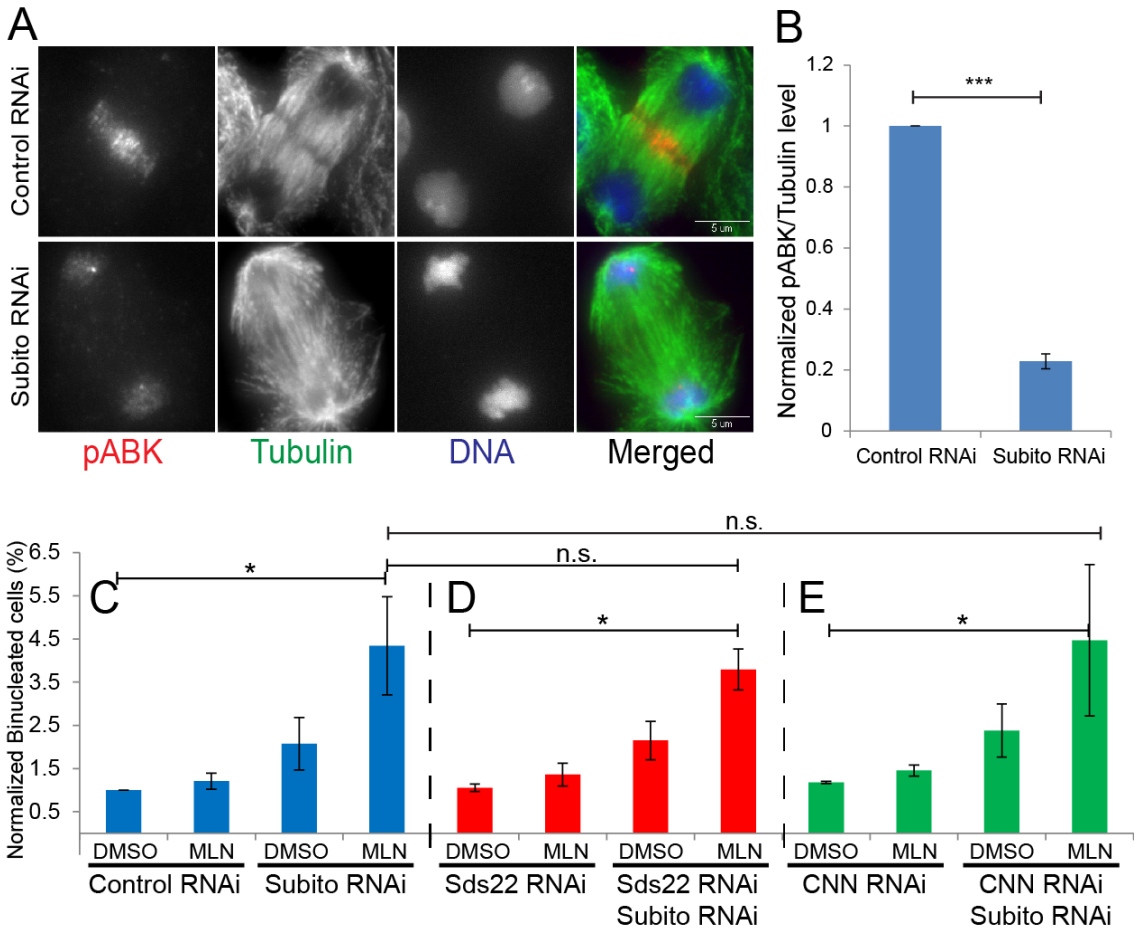
A
Control RNAi
Subito RNAi
pABK
Tubulin
DNA
Merged
B
Normalized pABK/Tubulin level
1.2
1
0.8
0.6
0.4
0.2
0
***
Control RNAi
Subito RNAi
Normalized Binucleated cells (%)
6.5
5.5
4.5
3.5
2.5
1.5
0.5
C
D
E
*
n.s.
n.s.
*
*
DMSO
MLN
Control RNAi
Subito RNAi
Sds22 RNAi
Sds22 RNAi Subito RNAi
CNN RNAi
CNN RNAi Subito RNAi

Figure 5.9. AAK and midzone ABK work redundantly to ensure proper cytokinesis.

(A) Representative images showing that subito depletion prevents relocalization of phosphorylated ABK (pABK) from the centromeres to the central spindle during the metaphase to anaphase transition. pABK staining remains at the centromeres in Subito-depleted cells. In the merged images, pABK is red, tubulin is green, and DAPI is blue. (B) Quantification of pABK levels at the spindle midzone in control and Subito RNAi at late anaphase. Quantification are from six independent experiments. Control RNAi, n = 130 cells; Subito RNAi, n = 119 cells. (C) Quantification of binucleated cells (normalized to the baseline levels of control cells) in those that were AAK-inhibited, and those that were Subito-depleted, with and without 125 nM MLN8237. AAK inhibition alone does lead to cytokinesis failure. Removal of midzone ABK (mABK) leads to a slight, but not statistically significant, increase in binucleated cells. Subito RNAi, in combination with 125 nM MLN8237 treatment, does lead to a statistically significant increase in binucleated cells. Quantifications are from five independent experiments. Control RNAi + DMSO, n = 2134 cells; control RNAi + 125 nM MLN8237, n = 2068 cells; subito RNAi + DMSO, n = 1500 cells; subito RNAi + 125 nM MLN8237, n = 1837 cells. (D) Depletion of the Sds22-mediated phosphatase gradient that is required for polar relaxation does not lead to an increase in binucleated cells. Cells depleted of the midzone aurora gradient in addition to the phosphatase gradient exhibit the same phenotype as the Subito RNAi + MLN condition. Quantifications are from three independent experiments. Control+sds22 RNAi + DMSO, n = 1305 cells; control+sds22 RNAi + 125 nM MLN8237, n = 1313 cells; subito+sds22 RNAi + DMSO, n = 1247 cells; subito+sds22 RNAi + 125 nM MLN8237, n = 1305 cells. (E) Depletion of centrosomin (CNN) does not increase the percentage of binucleated cells, and exhibits the same phenotype as the Subito RNAi + MLN condition when combined with this treatment. Quantifications are from two independent experiments. Control+CNN RNAi + DMSO, n = 823 cells; control+CNN RNAi + 125 nM MLN8237, n = 894 cells; subito+CNN RNAi + DMSO, n = 958 cells; subito+CNN RNAi + 125 nM MLN8237, n = 931 cells. All data points were normalized to the control or single RNAi + DMSO condition. Error bars are SEM. Scale bars = 5 μm. Two-tailed Student's t-tests are reported: not significant (n.s.), $P < 0.05$; *$P < 0.05$; ***$P < 0.0005$.

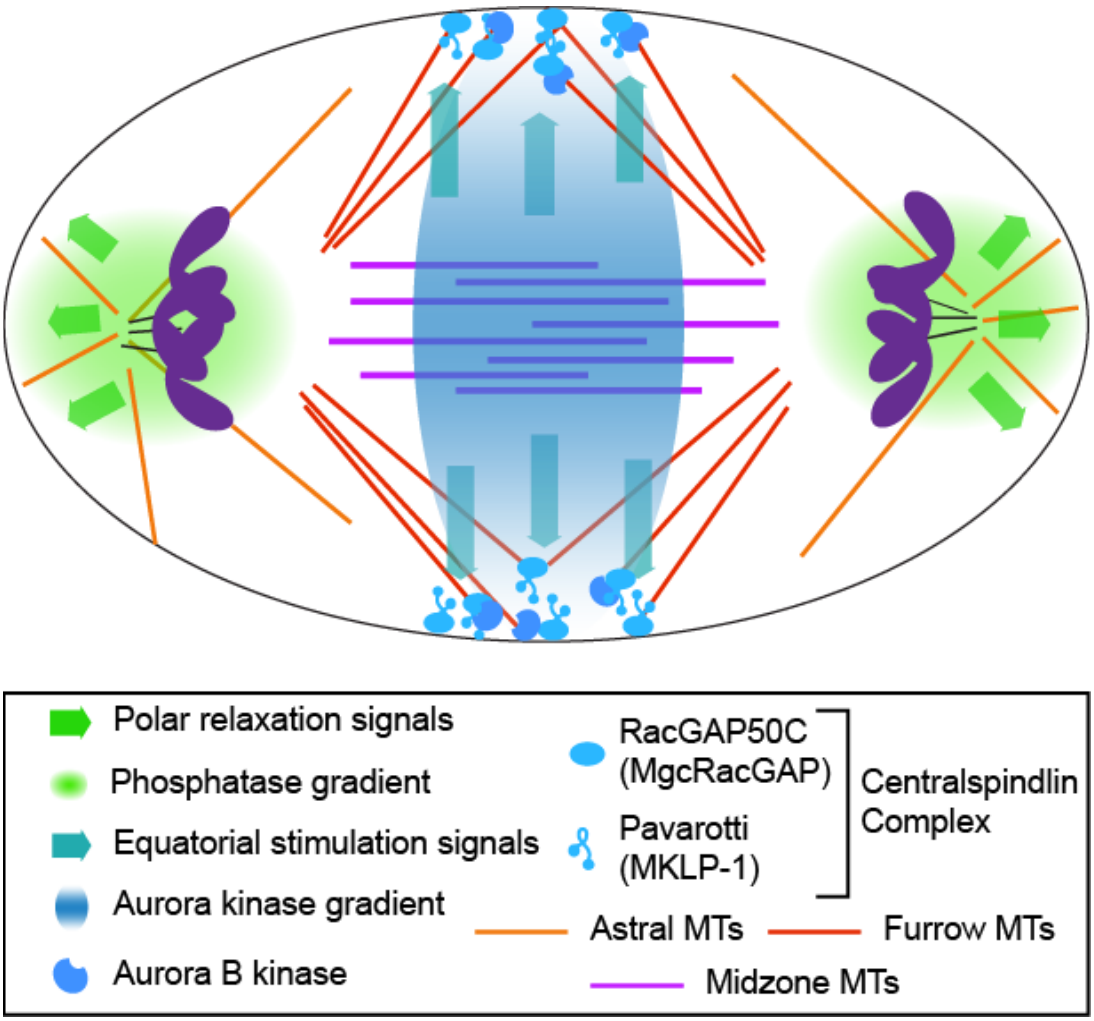

Figure 5.10. A model highlighting three pathways that regulate positioning of the cleavage furrow.
It has been proposed that three redundant pathways regulate the positioning an formation of the cleavage furrow: (1) Midzone MTs and (2) astral MTs send a stimulatory signal to the equatorial cell cortex, to promote cortical contraction, while a (3) a phosphate gradient induces polar cortex relaxation.

5.3 Discussion

The aurora family of kinases regulate many mitotic pathways, and their critical functions in early mitosis make it difficult to study their involvement in late anaphase and cytokinesis. Lioutas and Vernos (Lioutas and Vernos, 2013) and Reboutier *et al*. (Reboutier et al., 2013) have reported the importance of aurora A kinase (AAK) in the formation of a central spindle by regulating microtubule (MT) growth through phosphorylation of TACC3 and p150Glued, respectively. Here, we report that AAK activity also contributes to robust midzone MT assembly and to phosphorylation of midzone substrates in *Drosophila* S2 cells. Interestingly, total midzone levels of phosphorylated aurora B kinase (pABK) were normal in AAK-inhibited cells and actually higher when normalized to MTs despite having less robust midzones. Thus, there may be a regulatory mechanism that ensures adequate levels of chromosomal passenger complex (CPC) enrichment at overlapping midzone MTs that buffer against variations in MT density.

The experiments conducted in this study have allowed us to dissect the contributions of equatorial stimulation and polar relaxation pathways (Fig. 5.10). While depletion of MKLP2 and Subito leads to loss of mABK in human and *Drosophila* cells, respectively, their depletion leads to a significantly higher incidence of cytokinesis failure in human cells (Kitagawa et al., 2014; Kitagawa et al., 2013; Zhu et al., 2005). Since MKLP2-depleted cells fail during the late stages of cytokinesis (Zhu et al., 2005), this discrepancy may be due to differences in abscission mechanisms between human and *Drosophila*.

Interestingly, the fact that the cleavage furrow ingresses between segregating chromosomes in MKLP2-depleted human cells suggests that, as in *Drosophila* S2 cells, midzone ABK (mABK) is likely also dispensable for spatially positioning the cleavage furrow in human cells. In *Drosophila*, both midzone-derived and astral stimulation signals likely contribute to equatorial stimulation, while recent work (Rodrigues *et al.,* 2015) that polar relaxation is mediated by a phosphatase gradient emanating from kinetochores. We have shown that a midzone-based aurora kinase activity gradient that requires both mABK and a predominantly soluble pool of AAK contributes to the fidelity of cytokinesis. However, redundant and/or dominant pathways must exist, since a majority of cells lacking the midzone aurora activity gradient successfully complete cytokinesis. Polar relaxation signals from the phosphatase gradient or by centrosomal MTs are neither dominant—since single depletions of Sds22 or CNN do not lead to cytokinesis defects—nor redundant to the midzone aurora kinase activity gradient; the effects of depleting CNN or Sds22 combined with loss of the aurora phosphorylation gradient was identical to removing the aurora activity gradient alone. We infer from these data that the dominant pathway for spatially defining furrow formation in *Drosophila* S2 cells is the astral stimulation pathway.

Interestingly, astral stimulation, in this case, does not require centrosome-derived MTs, because CNN depletion has no effect on cytokinesis. We acknowledge that the concept of “astral” MTs without centrosomes seems counter-intuitive; however, we propose that, in *Drosophila* S2 cells, what is historically referred to as the astral stimulation pathway is actually mediated by a

population of critically important “furrow MTs” that do not require centrosomes to assemble. Furthermore, since inhibiting Pavarotti (*Dm* MKLP1) in *Drosophila* cells leads to complete failure in cytokinesis (Adams et al., 1998; Echard et al., 2004; Eggert et al., 2004; Goshima and Vale, 2003) it is likely that Pavarotti, as part of the Centralspindlin complex with RacGAP50C (*Dm* MgcRacGAP) (Glotzer, 2005) and other regulatory components, at the ends of furrow MTs are the central determinants of where the cleavage furrow forms. Pavarotti has been observed to tip-track on MTs at onset of anaphase. It eventually concentrates on the ends of MTs in the vicinity of the furrow, where it bundles and stabilizes intersecting MTs in the equatorial region (Vale et al., 2009). Both Pavarotti and ABK also accumulate as a band at the equatorial cortex, distinct from their localization to cortical MTs (Hu et al., 2008; Hu et al., 2011; Minestrini et al., 2003; Vale et al., 2009). Like Pavarotti, ABK, which has been reported to phosphorylate and regulate MKLP1 (Guse et al., 2005), accumulates on MT plus-ends at anaphase onset, and inhibition of ABK blocked the equatorial accumulation—but not the tip-localizing behavior—of Pavarotti (Vale et al., 2009). We envision that a midzone-derived aurora kinase activity gradient contributes to cytokinesis *via* crosstalk with a more dominant astral stimulation and/or furrow MT pathway through multiple, non-mutually exclusive mechanisms: 1) phosphorylating tip-tracking regulatory complexes, 2) rendering cortical components competent for equatorial accumulation of cytokinesis regulators such as RhoA, RhoGEF, ABK, and Pavarotti, and 3) stabilization of

furrow MTs, for example, through inhibition of catastrophe factors (Gadea and Ruderman, 2006; Kelly et al., 2007; Sampath et al., 2004).

In conclusion, we favor a model in which furrow positioning in *Drosophila* S2 cells is driven largely by equatorial stimulation that is comprised of 1) a midzone-derived stimulation signal to which an aurora kinase activity gradient contributes, and 2) what has traditionally been referred to as an “astral” stimulation signal, which is mediated by a non-centrosomal population of stable furrow MTs in the vicinity of the equatorial cortex (Canman et al., 2003; Field et al., 2015; Foe and von Dassow, 2008).

5.4 Materials and Methods

5.4.1 Drosophila S2 cell culture

All cell lines were grown in Schneider's medium (Life Technologies, Carlsbad, CA), supplemented with 10% heat-inactivated fetal bovine serum (FBS) and 0.5× antibiotic/antimycotic cocktail (Sigma-Aldrich, St. Louis, MO), and maintained at 25 °C. All cell lines were generated by transfecting the plasmid with Effectene Transfection Reagent system (Qiagen, Hilden, Germany), following the manufacturer's protocol. Expression of the proteins was checked by fluorescence microscopy. To select the cell expressing the constructs, cells were split in the presence of Blasticidin S HCl (Thermo Fisher Scientific, Waltham, MA) and/or Hygromycin (Sigma-Aldrich). (Spaghetti squash (*Dm* MRLC)-GFP, a mCherry-α-tubulin cell line, was a generous gift from Eric Griffis.)

5.4.2 DNA constructs

A soluble, Förster resonance energy transfer (FRET)-based aurora phosphorylation sensor was previously generated (Ye et al., 2015). To target this sensor to MTs, Tau (CG45110) was amplified from complementary DNA (cDNA) with flanking SpeI sites and inserted into the soluble reporter construct *via* Gibson assembly (Gibson et al., 2009). The Tau sequence was inserted downstream of the centromere protein C (CENP-C) promoter to drive expression of the reporter.

5.4.3 RNA interference (RNAi) experiments

DNA templates for subito (CG12298), aurora A kinase (CG3068), Sds22 (CG5851), and centrosomin (CNN) (CG4832) were produced to contain ~500 base pairs (bps) of complementary sequence flanked by T7 promoter sequence. Double-stranded RNAs (dsRNAs) were synthesized from the DNA templates overnight at 37 °C, using the T7 RiboMax Express Large Scale RNA Production System (Promega Corp., Madison, WI), following the manufacturer's protocol. For RNAi experiments, media was aspirated off semi-adhered cell at 25% confluency and replaced with 1 ml of serum-free Schneider's medium containing 20 μg of dsRNA. After 1 hour, 1 ml of fresh Schneider's media plus FBS was added to the wells and incubated for 2 days at 24 °C. See Table 1 for primer sequences.

5.4.4 Immunofluorescence

Drosophila S2 cells were allowed to adhere to acid-washed Concanavalin A (Sigma-Aldrich)-coated coverslips, then treated with 5 μM MG132 and 125 nM MLN8237 (MLN) (Selleck Chemicals, Houston, TX) or dimethyl sulfoxide (DMSO) as control for 1 h before being quickly rinsed with BRB80 buffer, and then fixed with 10% paraformaldehyde for 10 minutes. Cells were then permeabilized with phosphate-buffered saline (PBS) containing 1% Triton X-100 for 8 min, rinsed 3 times with PBS plus 0.1% Triton X-100, and blocked with boiled donkey serum for 60 min. All primary antibodies were diluted in boiled donkey serum. Anti-Phospho-aurora A/B/C and Phospho-aurora A (Cell Signaling Technology, Danvers, MA) was used at a concentration of 1:1000, and anti-tubulin antibody

(DM1α; Sigma-Aldrich) at 1:1000. All secondary antibodies (Jackson ImmunoResearch Laboratories, Inc., West Grove, PA) were diluted in boiled donkey serum at 1:200. After secondary treatment, coverslips were washed 2 times with PBS plus 0.1% Triton X-100, followed by incubation with 4',6'-diamidino-2-phenylindole (DAPI) at a concentration of 1:1000 for 5 min, and 2 additional washes. Coverslips were sealed in mounting media containing 20 mM Tris, pH 8.0, 0.5% N-propyl gallate, and 90% glycerol.

Three- or four-color Z-series consisting of ~30 planes at 0.2-μm intervals were acquired for green fluorescent protein (GFP), Rhodamine, Cy5 (where appropriate), and DAPI channels. Fluorescence intensities were obtained by drawing larger and small regions manually around the maximum-intensity projection of the Z-series images. To obtain the ratio intensities, regions were drawn manually on the tubulin channel and transferred to a phosphorylated ABK (pABK) channel. The following equations were used: background signal = (integrated fluorescence intensity of big area – integrated fluorescence intensity of small area)/(big area – small area). Total intensity = integrated fluorescence intensity of small area – (background signal × small area).

5.4.5 Förster resonance energy transfer (FRET)

Cells were treated with 125 nM MLN8237 (MLN) or DMSO as control, diluted 1:1000, in a tissue culture dish for 1 h. Cells were allowed to adhere to acid-washed, Concanavalin A (Sigma-Aldrich)-coated coverslip (Corning, Inc., Corning, NY) for exactly 1 h, then assembled in a rose chamber containing Schneider's medium with 125 nM MLN or DMSO, and subjected to imaging at 25

°C. Cells were image for a maximum of 1 h on an eclipse Ti-E inverted microscope (Nikon, Tokyo, Japan) equipped with an iXON EMCCD camera (Andor Technology, Belfast, U.K.), using a 100 × 1.4 NA Plan Apo violet-corrected series differential interference contrast objective (Nikon). Metamorph software (Molecular Devices, Sunnyvale, CA) was used to control the imaging system.

Mitotic cells were found in the red fluorescent protein (RFP) channel, and images of the best focal plane were acquired in RFP, CFP, and YFP, and FRET (CFP excitation and YFP emission) channels with equal exposure times. The ratios of the fluorescence intensities of FRET to the mTurqoise2 fluorescence intensity (CFP spectral channel) were obtained by drawing larger and smaller regions in Metamorph around the central spindle in the FRET images, then transferred to the CFP image. The background signal equations (see previous section) were used.

5.4.6 Western blots

A total of 10*u*g of protein was loaded into a 10% SDS-PAGE gel, run out, and transferred to a nitrocellulose membrane on the Trans-Blot Turbo transfer system (Bio-Rad Laboratories, Inc., Hercules, CA), using the manufacturer's preprogrammed 7-min "MIXED MW" protocol. All antibodies were diluted in Tris-buffered saline (TBS) with 0.1% Tween and 5% milk. The membrane was first incubated with anti-aurora A serum (gift of Marcin Przewloka and David Glover) at a 1:500 dilution, followed by DM1α at 1:500 dilution. Rabbit and mouse horseradish peroxidase (HRP) secondary antibodies (Jackson ImmunoResearch

Laboratories, Inc.), diluted at 1:500, were used in conjunction with their respective primaries and imaged with a GBox system controlled by GeneSnap software (Syngene, Cambridge, U.K.).

5.4.7 Total internal reflection fluorescence (TIRF) microscopic and spinning disk confocal imaging

Cells were allowed to adhere to Concanavalin A-treated coverslips, and mounted into a rose chamber. Cells were imaged on a TIRF-Spinning Disk system assembled on an Eclipse Ti-E inverted microscope (Nikon), equipped with a Borealis (Andor Technology, Ltd., Belfast, U.K.) retrofitted CSU-10 (Yokogawa Electric Corp., Tokyo, Japan) spinning disk head and two ORCA-Flash4.0 LT Digital CMOS (Hamamatsu Corp., Bridgewater, NJ), using a 100× 1.49 NA Apo differential interference contrast objective (Nikon). Metamorph software was used to control the imaging system. Dual TIRF (myosin regulatory light chain-green fluorescent protein; MRLC-GFP) and widefield (mCherry-α-tubulin) images were acquired at 1-min intervals. To quantify the myosin dynamic, three 10-pixel^2 boxes were placed in the pole region or the equator and averaged for each cell. To compare myosin accumulation at the equator and depletion at the pole, half-maximum change at the equator was normalized to be time 0 for each cell, and ten before-and-after time points are reported. For correlative TIRF-spinning disk confocal imaging, cells were followed by time-lapse TIRF imaging; once the cell had assembled a contractile ring (based on MRLC imaging) the system was switched to spinning disk mode and 0.2-μm confocal z-sections were taken. All quantifications and 3D-reconstructions were done using Metamorph software.

Microtubule dynamics in interphase cells were manually tracked using the MTrackJ plug-in (Meijering et al., 2012) in ImageJ (Schneider et al., 2012). The catastrophe and rescue frequencies are determined by the number of catastrophe events divided by the total amount of time of time spent polymerizing and the number of rescue events divided by the total amount of time spent depolymerizing, respectively.

CHAPTER 6

FUTURE DIRECTIONS

In this chapter I am describing some failed experiments and what are other approaches that can be taken to potentially answer the same questions. I am also highlighting some interesting findings that can be further explored by future students.

6.1 Dissecting the two modes of PEF generation by NOD

Drosophila NOD is a chromokinesin that binds to the chromosomes through the C-terminal domain, which contain two distinct chromatin binding domains, and has an N-terminal motor domain. When overexpressed in *Drosophila* S2 cells, NOD stabilizes syntelic attachments by generating excess polar ejection force (PEF). However, the molecular mechanism remained a mystery for many decades due to difficulties in reconstituting *in vitro* motility, thus NOD has been classified as an orphan non-motile kinesin. To the contrary to what has been established in the field, I've shown that NOD possesses plus-end directed motility. Additionally, I've shown that NOD also binds to EB1, suggesting that it can also track polymerizing microtubules. Careful analysis of dynamic microtubules, both in interphase and mitotic cells, showed that NOD is able to hang on to depolymerizing MTs, which is not the case with EB1.

To further characterize the molecular mechanism of NOD PEF generation, I've shown that NOD walks on MTs and interacts with EB1 *in vitro* motility experiments and pull down assays, respectively. Many lines of evidence was used to demonstrate that NOD possess motility: TIRF imaging of live cells, cell

extracts expressing fluorescent NOD motor domain, and NOD motors purified from Drosophila cells. It is important to note that NOD purification from *Drosophila* cells allows for optimal conditions to reconstitute motility as other interacting proteins are co-purified in the process and contains any post-translational modifications. I have tried using bacterial purified proteins, but like previous efforts, I was not successful in reconstituting motility. It is possible that NOD may require binding partners to promote MT binding and/or motility. In an effort to identify other factor, I purified NOD324, which does not binds to MT as a control, and NOD485 using a STREP® tag, and looked for unique bands in a coomasie stained SDS-PAGE gel (Fig 6.1). Two bands were subjected to mass spectrometry analysis, but unfortunately we did not identify any potential proteins. In the future, a better approach would be analyzing the entire elution from the purification instead of specific bands so we're not biasing a certain size protein.

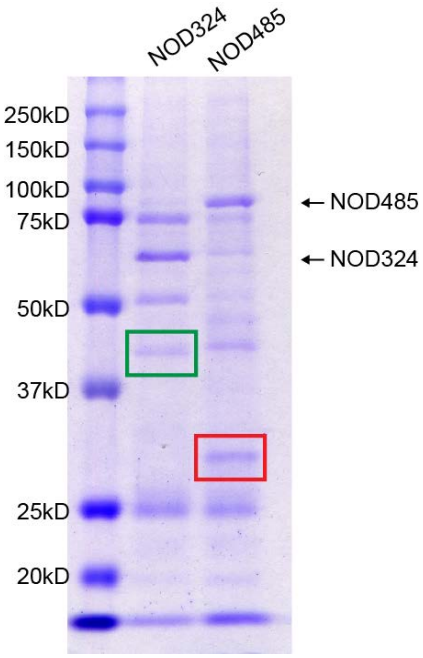

Figure 6.1 Coomasie SDS-PAGE gel of NOD324 and NOD485 purifications.
NOD324 and NOD485 purifications were run on a SDS-PAGE gel to identify unique bands. One unique band from each sample (highlighted in boxes) were sent for mass spectrometry analysis.

Many lines of evidence have submerged suggesting that NOD binds to plus-ends of MTs. We first observed EB1 co-localizing to chromatin stretches, then we saw NOD485CC molecules co-localize with EB1 both in interphase and mitotic cells (Fig 6.2). It is a challenge to make conclusions using live cell imaging because NOD walks at approximately the same rate as MT polymerization. To directly shown that NOD tip-track through EB1 interaction, I first tried pulldown assays from *Drosophila* S2 cells using a STREP® tag. Although the first experiment gave us excellent results, I have not been able to replicate it (Fig 6.3). In the subsequent experiments, I was not able to detect NOD485 specific binding of EB1, but rather, the amount of binding was very similar to the background EB1 binding to the beads in WT cells.

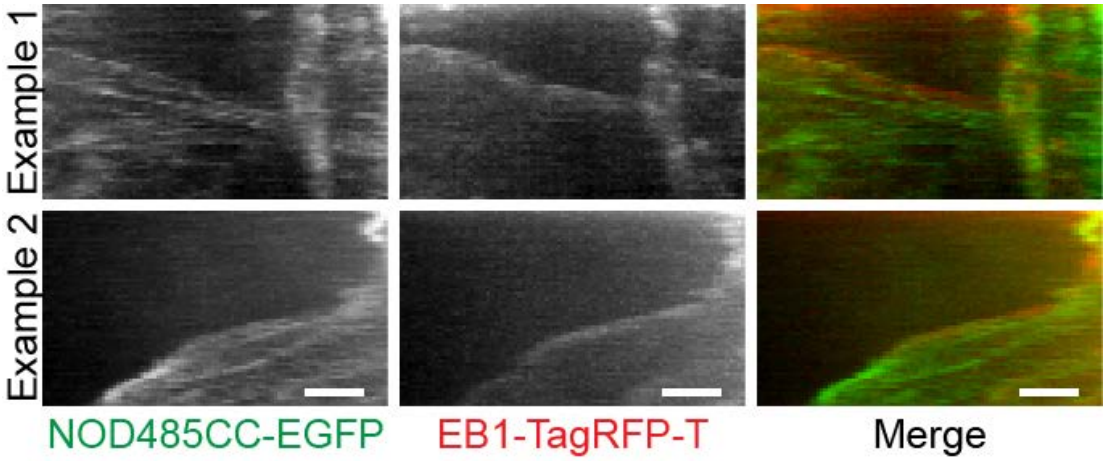

Figure 6.2 Example kymographs of NOD485CC tip-tracking in cells.
Kymographs showing NOD485CC molecules co-localizing with EB1 at the tips of polymerizing MTs. Note that in addition to binding to the tips, tracks of NOD molecules walking is also visible in these kymographs.

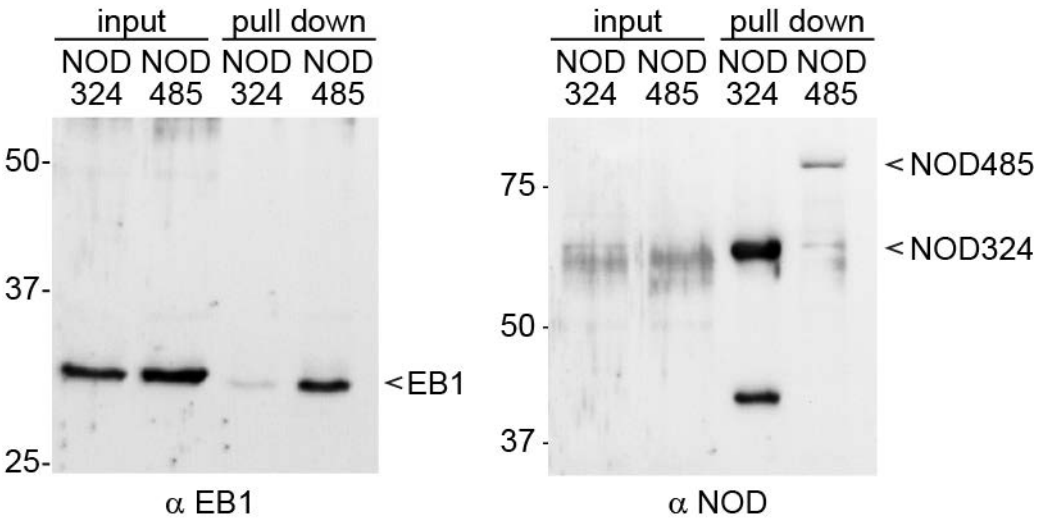

Figure 6.3 NOD pulldown assay.
NOD proteins with a STREP-® tag is pulled out of cell extracts using MagStrep "type 3" XT beads (IBA). Western blot analysis revealed that, even though more NOD324 is present, less EB1 is present, suggesting that EB1 in specifically binding to NOD485, to a region downstream of the motor domain.

NOD has a putative EB1 interacting SxIP motif, TVIP, within the motor domain, so it has been difficult to dissect the two functions using truncated proteins. I made a couple of NOD mutants and tested them in the PEF assays (Cane et al., 2013) with no success. However, I think it is worth to revisit the S94N mutant, which has a slower ATPase rate, in single molecule assays to more carefully characterize its motility. With the intentions to abolish the tip-tracking ability of NOD, I also made SxIP mutant (TVIP→TVNN), In the pulldown assays I did not see a decrease in EB1 binding to NOD. However, this can be interpreted that either NOD has multiple redundant EB1 interacting motifs, or the putative SxIP is not an EB1 binding domain. I favor the latter because NOD has a couple of the new emerging unconventional EB1 binding "PT" motif downstream of the motor domain. We showed using SPOT peptide arrays that these "PT" motifs are sufficient to bind to EB1. I have also shown the binding affinity of NOD "PT"

motif-1 to GST-EB1 using microscale thermophoresis. It has been proposed that SxIP motif and PT motifs partially share binding pocked, thus it will be interesting to perform competition assay to further explore this point.

NOD is a processive motor, posing a challenge to distinguish tip-tracking and motor functions in cells and *in vitro.* In order to reconstitute NOD tip-tracking it is necessary to generate a non-motile mutant. Previous work have found that the S94N mutant has a decreased ATPase rate, but not defective. Thus, it is warranted to take a closer look at this mutant in cells using TIRF microscopy and/or *in vitro* TIRF assays. Lastly, to directly show that NOD is generating PEF by walking and tip-tracking, it is important to generate a mutant with both activities abolished and use it in the PEF assay.

6.2 Cleavage furrow formation and positioning

Upon anaphase onset the CPC relocalizes to the spindle midzone, which initially thought to be critical for delaying the formation of the nuclear envelope around lagging chromosomes and the positioning of the cleavage furrow. However, keeping in mind that ABK has a very short working distance that is able to detect changes within hundreds of nanometer, how is it able to send a signal from the central spindle to the cortex, which is microns away? Our initial hypothesis was that AAK, which has a much larger working distance, is amplifying a kinase gradient at the cell equator. Further analysis revealed that, although both kinases contributes to the positioning of the cleavage, the number of binucleated cells in AAK and ABK depleted cells is very mild. Since there are three possible redundant pathways in regulating the position of the cleavage furrow, I attempted

to eliminate each individually, and in combination, but to my surprise, no condition gave me cytokinesis failure phenotype. Upon more careful observation, a population of non-centrosome derived MTs are stabilized near the cortex at the location of cytokinesis. Thus I posit that these special MTs are delivering important factors to the cortex to regulate and activate the actomyosin network during cytokinesis. To understand how the cell determines the position of the cleavage furrow and activates the actomyosin network, it is important to explore what proteins are being delivered to the cortex and how they are being transported along a MT. Lastly, the cell has a lot of dynamic MTs making contact with the cell cortex at any given time, but only a small population of them are near the cell equator, which leads to the main question: how does the cell define which MTs to use to send the cytokinesis factors on so they will be at the cell equator?

BIBLIOGRAPHY

Adams, R.R., H. Maiato, W.C. Earnshaw, and M. Carmena. 2001. Essential roles of Drosophila inner centromere protein (INCENP) and aurora B in histone H3 phosphorylation, metaphase chromosome alignment, kinetochore disjunction, and chromosome segregation. *J Cell Biol*. 153:865-880.

Adams, R.R., A.A. Tavares, A. Salzberg, H.J. Bellen, and D.M. Glover. 1998. pavarotti encodes a kinesin-like protein required to organize the central spindle and contractile ring for cytokinesis. *Genes Dev*. 12:1483-1494.

Adams, R.R., S.P. Wheatley, A.M. Gouldsworthy, S.E. Kandels-Lewis, M. Carmena, C. Smythe, D.L. Gerloff, and W.C. Earnshaw. 2000. INCENP binds the Aurora-related kinase AIRK2 and is required to target it to chromosomes, the central spindle and cleavage furrow. *Curr Biol*. 10:1075-1078.

Afonso, O., I. Matos, A.J. Pereira, P. Aguiar, M.A. Lampson, and H. Maiato. 2014. Feedback control of chromosome separation by a midzone Aurora B gradient. *Science*. 345:332-336.

Afshar, K., N.R. Barton, R.S. Hawley, and L.S. Goldstein. 1995a. DNA binding and meiotic chromosomal localization of the Drosophila nod kinesin-like protein. *Cell*. 81:129-138.

Afshar, K., J. Scholey, and R.S. Hawley. 1995b. Identification of the chromosome localization domain of the Drosophila nod kinesin-like protein. *J Cell Biol*. 131:833-843.

Akiyoshi, B., C.R. Nelson, J.A. Ranish, and S. Biggins. 2009. Analysis of Ipl1-mediated phosphorylation of the Ndc80 kinetochore protein in Saccharomyces cerevisiae. *Genetics*. 183:1591-1595.

Akiyoshi, B., K.K. Sarangapani, A.F. Powers, C.R. Nelson, S.L. Reichow, H. Arellano-Santoyo, T. Gonen, J.A. Ranish, C.L. Asbury, and S. Biggins. 2010. Tension directly stabilizes reconstituted kinetochore-microtubule attachments. *Nature*. 468:576-579.

Al-Bassam, J., Y. Cui, D. Klopfenstein, B.O. Carragher, R.D. Vale, and R.A. Milligan. 2003. Distinct conformations of the kinesin Unc104 neck regulate a monomer to dimer motor transition. *J Cell Biol*. 163:743-753.

Alexander, S.P., and C.L. Rieder. 1991. Chromosome motion during attachment to the vertebrate spindle: initial saltatory-like behavior of chromosomes and quantitative analysis of force production by nascent kinetochore fibers. *J Cell Biol*. 113:805-815.

Alsop, G.B., and D. Zhang. 2003. Microtubules are the only structural constituent of the spindle apparatus required for induction of cell cleavage. *J Cell Biol*. 162:383-390.

Alushin, G.M., V. Musinipally, D. Matson, J. Tooley, P.T. Stukenberg, and E. Nogales. 2012. Multimodal microtubule binding by the Ndc80 kinetochore complex. *Nat Struct Mol Biol*. 19:1161-1167.

Alushin, G.M., V.H. Ramey, S. Pasqualato, D.A. Ball, N. Grigorieff, A. Musacchio, and E. Nogales. 2010. The Ndc80 kinetochore complex forms oligomeric arrays along microtubules. *Nature*. 467:805-810.

Anthis, N.J., and G.M. Clore. 2013. Sequence-specific determination of protein and peptide concentrations by absorbance at 205 nm. *Protein Sci*. 22:851-858.

Antonio, C., I. Ferby, H. Wilhelm, M. Jones, E. Karsenti, A.R. Nebreda, and I. Vernos. 2000. Xkid, a chromokinesin required for chromosome alignment on the metaphase plate. *Cell*. 102:425-435.

Bakhoum, S.F., L. Kabeche, J.P. Murnane, B.I. Zaki, and D.A. Compton. 2014. DNA-damage response during mitosis induces whole-chromosome missegregation. *Cancer Discov*. 4:1281-1289.

Barisic, M., P. Aguiar, S. Geley, and H. Maiato. 2014. Kinetochore motors drive congression of peripheral polar chromosomes by overcoming random arm-ejection forces. *Nat Cell Biol*. 16:1249-1256.

Barisic, M., and H. Maiato. 2015. Dynein prevents erroneous kinetochore-microtubule attachments in mitosis. *Cell Cycle*. 14:3356-3361.

Berdnik, D., and J.A. Knoblich. 2002. Drosophila Aurora-A is required for centrosome maturation and actin-dependent asymmetric protein localization during mitosis. *Curr Biol*. 12:640-647.

Bieling, P., I. Kronja, and T. Surrey. 2010. Microtubule motility on reconstituted meiotic chromatin. *Curr Biol*. 20:763-769.

Bringmann, H., G. Skiniotis, A. Spilker, S. Kandels-Lewis, I. Vernos, and T. Surrey. 2004. A kinesin-like motor inhibits microtubule dynamic instability. *Science*. 303:1519-1522.

Brouhard, G.J., and A.J. Hunt. 2005. Microtubule movements on the arms of mitotic chromosomes: polar ejection forces quantified in vitro. *Proc Natl Acad Sci U S A*. 102:13903-13908.

Buchan, D.W., F. Minneci, T.C. Nugent, K. Bryson, and D.T. Jones. 2013. Scalable web services for the PSIPRED Protein Analysis Workbench. *Nucleic Acids Res*. 41:W349-357.

Cai, D., K.J. Verhey, and E. Meyhofer. 2007. Tracking single Kinesin molecules in the cytoplasm of mammalian cells. *Biophys J*. 92:4137-4144.

Cai, S., C.B. O'Connell, A. Khodjakov, and C.E. Walczak. 2009. Chromosome congression in the absence of kinetochore fibres. *Nat Cell Biol*. 11:832-838.

Caldas, G.V., K.F. DeLuca, and J.G. DeLuca. 2013. KNL1 facilitates phosphorylation of outer kinetochore proteins by promoting Aurora B kinase activity. *J Cell Biol*. 203:957-969.

Campbell, C.S., and A. Desai. 2013. Tension sensing by Aurora B kinase is independent of survivin-based centromere localization. *Nature*. 497:118-121.

Cane, S., A.A. Ye, S.J. Luks-Morgan, and T.J. Maresca. 2013. Elevated polar ejection forces stabilize kinetochore-microtubule attachments. *J Cell Biol*. 200:203-218.

Canman, J.C., L.A. Cameron, P.S. Maddox, A. Straight, J.S. Tirnauer, T.J. Mitchison, G. Fang, T.M. Kapoor, and E.D. Salmon. 2003. Determining the position of the cell division plane. *Nature*. 424:1074-1078.

Carmena, M., and W.C. Earnshaw. 2003. The cellular geography of aurora kinases. *Nat Rev Mol Cell Biol*. 4:842-854.

Carmena, M., S. Ruchaud, and W.C. Earnshaw. 2009. Making the Auroras glow: regulation of Aurora A and B kinase function by interacting proteins. *Curr Opin Cell Biol*. 21:796-805.

Carpenter, A.T. 1973. A meiotic mutant defective in distributive disjunction in Drosophila melanogaster. *Genetics*. 73:393-428.

Carroll, C.W., K.J. Milks, and A.F. Straight. 2010. Dual recognition of CENP-A nucleosomes is required for centromere assembly. *J Cell Biol*. 189:1143-1155.

Cassimeris, L., C.L. Rieder, and E.D. Salmon. 1994. Microtubule assembly and kinetochore directional instability in vertebrate monopolar spindles: implications for the mechanism of chromosome congression. *J Cell Sci*. 107 (Pt 1):285-297.

Cesario, J.M., J.K. Jang, B. Redding, N. Shah, T. Rahman, and K.S. McKim. 2006. Kinesin 6 family member Subito participates in mitotic spindle assembly and interacts with mitotic regulators. *J Cell Sci*. 119:4770-4780.

Chacon, J.M., S. Mukherjee, B.M. Schuster, D.J. Clarke, and M.K. Gardner. 2014. Pericentromere tension is self-regulated by spindle structure in metaphase. *J Cell Biol*. 205:313-324.

Chan, Y.W., A.A. Jeyaprakash, E.A. Nigg, and A. Santamaria. 2012. Aurora B controls kinetochore-microtubule attachments by inhibiting Ska complex-KMN network interaction. *J Cell Biol*. 196:563-571.

Cheeseman, I.M., S. Anderson, M. Jwa, E.M. Green, J. Kang, J.R. Yates, 3rd, C.S. Chan, D.G. Drubin, and G. Barnes. 2002. Phospho-regulation of kinetochore-microtubule attachments by the Aurora kinase Ipl1p. *Cell*. 111:163-172.

Cheeseman, I.M., J.S. Chappie, E.M. Wilson-Kubalek, and A. Desai. 2006. The conserved KMN network constitutes the core microtubule-binding site of the kinetochore. *Cell*. 127:983-997.

Chmatal, L., K. Yang, R.M. Schultz, and M.A. Lampson. 2015. Spatial Regulation of Kinetochore Microtubule Attachments by Destabilization at Spindle Poles in Meiosis I. *Curr Biol*. 25:1835-1841.

Ciferri, C., S. Pasqualato, E. Screpanti, G. Varetti, S. Santaguida, G. Dos Reis, A. Maiolica, J. Polka, J.G. De Luca, P. De Wulf, M. Salek, J. Rappsilber, C.A. Moores, E.D. Salmon, and A. Musacchio. 2008. Implications for kinetochore-microtubule attachment from the structure of an engineered Ndc80 complex. *Cell*. 133:427-439.

Cimini, D., B. Moree, J.C. Canman, and E.D. Salmon. 2003. Merotelic kinetochore orientation occurs frequently during early mitosis in mammalian tissue cells and error correction is achieved by two different mechanisms. *J Cell Sci*. 116:4213-4225.

Cimini, D., X. Wan, C.B. Hirel, and E.D. Salmon. 2006. Aurora kinase promotes turnover of kinetochore microtubules to reduce chromosome segregation errors. *Curr Biol*. 16:1711-1718.

Cochran, J.C., C.V. Sindelar, N.K. Mulko, K.A. Collins, S.E. Kong, R.S. Hawley, and F.J. Kull. 2009. ATPase cycle of the nonmotile kinesin NOD allows microtubule end tracking and drives chromosome movement. *Cell*. 136:110-122.

Conduit, P.T., A. Wainman, and J.W. Raff. 2015. Centrosome function and assembly in animal cells. *Nat Rev Mol Cell Biol*. 16:611-624.

Coue, M., V.A. Lombillo, and J.R. McIntosh. 1991. Microtubule depolymerization promotes particle and chromosome movement in vitro. *J Cell Biol*. 112:1165-1175.

Critchley, D.R. 2009. Biochemical and structural properties of the integrin-associated cytoskeletal protein talin. *Annu Rev Biophys*. 38:235-254.

Cui, W., and R.S. Hawley. 2005. The HhH2/NDD domain of the Drosophila Nod chromokinesin-like protein is required for binding to chromosomes in the oocyte nucleus. *Genetics*. 171:1823-1835.

Cui, W., L.R. Sproul, S.M. Gustafson, H.J. Matthies, S.P. Gilbert, and R.S. Hawley. 2005. Drosophila Nod protein binds preferentially to the plus ends of microtubules and promotes microtubule polymerization in vitro. *Mol Biol Cell*. 16:5400-5409.

D'Avino, P.P., M.S. Savoian, and D.M. Glover. 2005. Cleavage furrow formation and ingression during animal cytokinesis: a microtubule legacy. *J Cell Sci*. 118:1549-1558.

Davies, T., N. Kodera, G.S. Kaminski Schierle, E. Rees, M. Erdelyi, C.F. Kaminski, T. Ando, and M. Mishima. 2015. CYK4 promotes antiparallel microtubule bundling by optimizing MKLP1 neck conformation. *PLoS Biol*. 13:e1002121.

del Rio, A., R. Perez-Jimenez, R. Liu, P. Roca-Cusachs, J.M. Fernandez, and M.P. Sheetz. 2009. Stretching single talin rod molecules activates vinculin binding. *Science*. 323:638-641.

DeLuca, J.G., W.E. Gall, C. Ciferri, D. Cimini, A. Musacchio, and E.D. Salmon. 2006. Kinetochore microtubule dynamics and attachment stability are regulated by Hec1. *Cell*. 127:969-982.

DeLuca, K.F., S.M. Lens, and J.G. DeLuca. 2011. Temporal changes in Hec1 phosphorylation control kinetochore-microtubule attachment stability during mitosis. *J Cell Sci*. 124:622-634.

Desai, A., S. Verma, T.J. Mitchison, and C.E. Walczak. 1999. Kin I kinesins are microtubule-destabilizing enzymes. *Cell*. 96:69-78.

Dogterom, M., and B. Yurke. 1997. Measurement of the force-velocity relation for growing microtubules. *Science*. 278:856-860.

Duncan, J.E., and L.S. Goldstein. 2006. The genetics of axonal transport and axonal transport disorders. *PLoS Genet*. 2:e124.

Echard, A., G.R. Hickson, E. Foley, and P.H. O'Farrell. 2004. Terminal cytokinesis events uncovered after an RNAi screen. *Curr Biol*. 14:1685-1693.

Eggert, U.S., A.A. Kiger, C. Richter, Z.E. Perlman, N. Perrimon, T.J. Mitchison, and C.M. Field. 2004. Parallel chemical genetic and genome-wide RNAi screens identify cytokinesis inhibitors and targets. *PLoS Biol*. 2:e379.

Emanuele, M.J., W. Lan, M. Jwa, S.A. Miller, C.S. Chan, and P.T. Stukenberg. 2008. Aurora B kinase and protein phosphatase 1 have opposing roles in modulating kinetochore assembly. *J Cell Biol*. 181:241-254.

Eyers, P.A., E. Erikson, L.G. Chen, and J.L. Maller. 2003. A novel mechanism for activation of the protein kinase Aurora A. *Curr Biol*. 13:691-697.

Ferraro-Gideon, J., R. Sheykhani, Q. Zhu, M.L. Duquette, M.W. Berns, and A. Forer. 2013. Measurements of forces produced by the mitotic spindle using optical tweezers. *Mol Biol Cell*. 24:1375-1386.

Field, C.M., A.C. Groen, P.A. Nguyen, and T.J. Mitchison. 2015. Spindle-to-cortex communication in cleaving, polyspermic Xenopus eggs. *Mol Biol Cell*. 26:3628-3640.

Foe, V.E., and G. von Dassow. 2008. Stable and dynamic microtubules coordinately shape the myosin activation zone during cytokinetic furrow formation. *J Cell Biol*. 183:457-470.

Friedman, D.S., and R.D. Vale. 1999. Single-molecule analysis of kinesin motility reveals regulation by the cargo-binding tail domain. *Nat Cell Biol*. 1:293-297.

Fuller, B.G., M.A. Lampson, E.A. Foley, S. Rosasco-Nitcher, K.V. Le, P. Tobelmann, D.L. Brautigan, P.T. Stukenberg, and T.M. Kapoor. 2008. Midzone activation of aurora B in anaphase produces an intracellular phosphorylation gradient. *Nature*. 453:1132-1136.

Funabiki, H., and A.W. Murray. 2000. The Xenopus chromokinesin Xkid is essential for metaphase chromosome alignment and must be degraded to allow anaphase chromosome movement. *Cell*. 102:411-424.

Gadea, B.B., and J.V. Ruderman. 2006. Aurora B is required for mitotic chromatin-induced phosphorylation of Op18/Stathmin. *Proc Natl Acad Sci U S A*. 103:4493-4498.

Gennerich, A., A.P. Carter, S.L. Reck-Peterson, and R.D. Vale. 2007. Force-induced bidirectional stepping of cytoplasmic dynein. *Cell*. 131:952-965.

Gibson, D.G., L. Young, R.Y. Chuang, J.C. Venter, C.A. Hutchison, 3rd, and H.O. Smith. 2009. Enzymatic assembly of DNA molecules up to several hundred kilobases. *Nat Methods*. 6:343-345.

Giet, R., D. McLean, S. Descamps, M.J. Lee, J.W. Raff, C. Prigent, and D.M. Glover. 2002. Drosophila Aurora A kinase is required to localize D-TACC to centrosomes and to regulate astral microtubules. *J Cell Biol*. 156:437-451.

Glotzer, M. 2004. Cleavage furrow positioning. *The Journal of Cell Biology*. 164:347-351.

Glotzer, M. 2005. The molecular requirements for cytokinesis. *Science*. 307:1735-1739.

Glover, D.M., M.H. Leibowitz, D.A. McLean, and H. Parry. 1995. Mutations in aurora prevent centrosome separation leading to the formation of monopolar spindles. *Cell*. 81:95-105.

Godek, K.M., L. Kabeche, and D.A. Compton. 2015. Regulation of kinetochore-microtubule attachments through homeostatic control during mitosis. *Nat Rev Mol Cell Biol*. 16:57-64.

Goshima, G. 2011. Identification of a TPX2-like microtubule-associated protein in Drosophila. *PLoS One*. 6:e28120.

Goshima, G., and R.D. Vale. 2003. The roles of microtubule-based motor proteins in mitosis: comprehensive RNAi analysis in the Drosophila S2 cell line. *J Cell Biol*. 162:1003-1016.

Grashoff, C., B.D. Hoffman, M.D. Brenner, R. Zhou, M. Parsons, M.T. Yang, M.A. McLean, S.G. Sligar, C.S. Chen, T. Ha, and M.A. Schwartz. 2010. Measuring mechanical tension across vinculin reveals regulation of focal adhesion dynamics. *Nature*. 466:263-266.

Greenan, G., C.P. Brangwynne, S. Jaensch, J. Gharakhani, F. Julicher, and A.A. Hyman. 2010. Centrosome size sets mitotic spindle length in Caenorhabditis elegans embryos. *Curr Biol*. 20:353-358.

Grishchuk, E.L., A.K. Efremov, V.A. Volkov, I.S. Spiridonov, N. Gudimchuk, S. Westermann, D. Drubin, G. Barnes, J.R. McIntosh, and F.I. Ataullakhanov. 2008. The Dam1 ring binds microtubules strongly enough to be a processive as well as energy-efficient coupler for chromosome motion. *Proc Natl Acad Sci U S A*. 105:15423-15428.

Grishchuk, E.L., and J.R. McIntosh. 2006. Microtubule depolymerization can drive poleward chromosome motion in fission yeast. *EMBO J*. 25:4888-4896.

Grishchuk, E.L., M.I. Molodtsov, F.I. Ataullakhanov, and J.R. McIntosh. 2005. Force production by disassembling microtubules. *Nature*. 438:384-388.

Gruneberg, U., R. Neef, R. Honda, E.A. Nigg, and F.A. Barr. 2004. Relocation of Aurora B from centromeres to the central spindle at the metaphase to anaphase transition requires MKlp2. *J Cell Biol*. 166:167-172.

Gudimchuk, N., B. Vitre, Y. Kim, A. Kiyatkin, D.W. Cleveland, F.I. Ataullakhanov, and E.L. Grishchuk. 2013a. Kinetochore kinesin CENP-E is a processive bi-directional tracker of dynamic microtubule tips. *Nat Cell Biol*. 15:1079-1088.

Gudimchuk, N., B. Vitre, Y. Kim, A. Kiyatkin, D.W. Cleveland, F.I. Ataullakhanov, and E.L. Grishchuk. 2013b. Kinetochore kinesin CENP-E is a processive bi-directional tracker of dynamic microtubule tips. *Nat Cell Biol*. 15:1079-1088.

Guimaraes, G.J., Y. Dong, B.F. McEwen, and J.G. Deluca. 2008. Kinetochore-microtubule attachment relies on the disordered N-terminal tail domain of Hec1. *Curr Biol*. 18:1778-1784.

Guse, A., M. Mishima, and M. Glotzer. 2005. Phosphorylation of ZEN-4/MKLP1 by aurora B regulates completion of cytokinesis. *Curr Biol*. 15:778-786.

Hannak, E., M. Kirkham, A.A. Hyman, and K. Oegema. 2001. Aurora-A kinase is required for centrosome maturation in Caenorhabditis elegans. *J Cell Biol*. 155:1109-1116.

Hochegger, H., N. Hegarat, and J.B. Pereira-Leal. 2013. Aurora at the pole and equator: overlapping functions of Aurora kinases in the mitotic spindle. *Open Biol*. 3:120185.

Hu, C.K., M. Coughlin, C.M. Field, and T.J. Mitchison. 2008. Cell polarization during monopolar cytokinesis. *J Cell Biol*. 181:195-202.

Hu, C.K., M. Coughlin, C.M. Field, and T.J. Mitchison. 2011. KIF4 regulates midzone length during cytokinesis. *Curr Biol*. 21:815-824.

Jiang, K., G. Toedt, S. Montenegro Gouveia, N.E. Davey, S. Hua, B. van der Vaart, I. Grigoriev, J. Larsen, L.B. Pedersen, K. Bezstarosti, M. Lince-Faria, J. Demmers, M.O. Steinmetz, T.J. Gibson, and A. Akhmanova. 2012a. A Proteome-wide screen for mammalian SxIP motif-containing microtubule plus-end tracking proteins. *Curr Biol*. 22:1800-1807.

Jiang, K., G. Toedt, S. Montenegro Gouveia, Norman E. Davey, S. Hua, B. van der Vaart, I. Grigoriev, J. Larsen, Lotte B. Pedersen, K. Bezstarosti, M. Lince-Faria, J. Demmers, Michel O. Steinmetz, Toby J. Gibson, and A. Akhmanova. 2012b. A Proteome-wide Screen for Mammalian SxIP Motif-Containing Microtubule Plus-End Tracking Proteins. *Current Biology*. 22:1800-1807.

Joglekar, A.P., D.C. Bouck, J.N. Molk, K.S. Bloom, and E.D. Salmon. 2006. Molecular architecture of a kinetochore-microtubule attachment site. *Nat Cell Biol*. 8:581-585.

Kajtez, J., A. Solomatina, M. Novak, B. Polak, K. Vukusic, J. Rudiger, G. Cojoc, A. Milas, I. Sumanovac Sestak, P. Risteski, F. Tavano, A.H. Klemm, E. Roscioli, J. Welburn, D. Cimini, M. Gluncic, N. Pavin, and I.M. Tolic. 2016. Overlap microtubules link sister k-fibres and balance the forces on bi-oriented kinetochores. *Nat Commun*. 7:10298.

Kalab, P., A. Pralle, E.Y. Isacoff, R. Heald, and K. Weis. 2006. Analysis of a RanGTP-regulated gradient in mitotic somatic cells. *Nature*. 440:697-701.

Kalab, P., K. Weis, and R. Heald. 2002. Visualization of a Ran-GTP gradient in interphase and mitotic Xenopus egg extracts. *Science*. 295:2452-2456.

Kalantzaki, M., E. Kitamura, T. Zhang, A. Mino, B. Novak, and T.U. Tanaka. 2015. Kinetochore-microtubule error correction is driven by differentially regulated interaction modes. *Nat Cell Biol*. 17:421-433.

Kapoor, T.M., M.A. Lampson, P. Hergert, L. Cameron, D. Cimini, E.D. Salmon, B.F. McEwen, and A. Khodjakov. 2006. Chromosomes can congress to the metaphase plate before biorientation. *Science*. 311:388-391.

Ke, K., J. Cheng, and A.J. Hunt. 2009. The distribution of polar ejection forces determines the amplitude of chromosome directional instability. *Curr Biol*. 19:807-815.

Kelly, A.E., and H. Funabiki. 2009. Correcting aberrant kinetochore microtubule attachments: an Aurora B-centric view. *Curr Opin Cell Biol*. 21:51-58.

Kelly, A.E., S.C. Sampath, T.A. Maniar, E.M. Woo, B.T. Chait, and H. Funabiki. 2007. Chromosomal enrichment and activation of the aurora B pathway are coupled to spatially regulate spindle assembly. *Dev Cell*. 12:31-43.

Kettenbach, A.N., D.K. Schweppe, B.K. Faherty, D. Pechenick, A.A. Pletnev, and S.A. Gerber. 2011. Quantitative phosphoproteomics identifies substrates and functional modules of Aurora and Polo-like kinase activities in mitotic cells. *Sci Signal*. 4:rs5.

Khodjakov, A., and C.L. Rieder. 1996. Kinetochores moving away from their associated pole do not exert a significant pushing force on the chromosome. *J Cell Biol*. 135:315-327.

Kim, Y., A.J. Holland, W. Lan, and D.W. Cleveland. 2010. Aurora kinases and protein phosphatase 1 mediate chromosome congression through regulation of CENP-E. *Cell*. 142:444-455.

Kitagawa, M., S.Y. Fung, U.F. Hameed, H. Goto, M. Inagaki, and S.H. Lee. 2014. Cdk1 coordinates timely activation of MKlp2 kinesin with relocation of the chromosome passenger complex for cytokinesis. *Cell Rep*. 7:166-179.

Kitagawa, M., S.Y. Fung, N. Onishi, H. Saya, and S.H. Lee. 2013. Targeting Aurora B to the equatorial cortex by MKlp2 is required for cytokinesis. *PLoS One*. 8:e64826.

Kitajima, T.S., M. Ohsugi, and J. Ellenberg. 2011. Complete kinetochore tracking reveals error-prone homologous chromosome biorientation in mammalian oocytes. *Cell*. 146:568-581.

Kline, S.L., I.M. Cheeseman, T. Hori, T. Fukagawa, and A. Desai. 2006. The human Mis12 complex is required for kinetochore assembly and proper chromosome segregation. *J Cell Biol*. 173:9-17.

Klopfenstein, D.R., M. Tomishige, N. Stuurman, and R.D. Vale. 2002. Role of phosphatidylinositol(4,5)bisphosphate organization in membrane transport by the Unc104 kinesin motor. *Cell*. 109:347-358.

Klopfenstein, D.R., and R.D. Vale. 2004. The lipid binding pleckstrin homology domain in UNC-104 kinesin is necessary for synaptic vesicle transport in Caenorhabditis elegans. *Mol Biol Cell*. 15:3729-3739.

Koshland, D.E., T.J. Mitchison, and M.W. Kirschner. 1988. Polewards chromosome movement driven by microtubule depolymerization in vitro. *Nature*. 331:499-504.

Kufer, T.A., H.H. Sillje, R. Korner, O.J. Gruss, P. Meraldi, and E.A. Nigg. 2002. Human TPX2 is required for targeting Aurora-A kinase to the spindle. *J Cell Biol*. 158:617-623.

Kumar, A., C. Manatschal, A. Rai, I. Grigoriev, M.S. Degen, R. Jaussi, I. Kretzschmar, A.E. Prota, R. Volkmer, R.A. Kammerer, A. Akhmanova, and M.O. Steinmetz. 2017a. Short Linear Sequence Motif LxxPTPh Targets Diverse Proteins to Growing Microtubule Ends. *Structure*. 25:924-932.e924.

Kumar, A., C. Manatschal, A. Rai, I. Grigoriev, M.S. Degen, R. Jaussi, I. Kretzschmar, A.E. Prota, R. Volkmer, R.A. Kammerer, A. Akhmanova, and M.O. Steinmetz. 2017b. Short Linear Sequence Motif LxxPTPh Targets Diverse Proteins to Growing Microtubule Ends. *Structure*. 25:924-932 e924.

Kunda, P., N.T. Rodrigues, E. Moeendarbary, T. Liu, A. Ivetic, G. Charras, and B. Baum. 2012. PP1-mediated moesin dephosphorylation couples polar relaxation to mitotic exit. *Curr Biol*. 22:231-236.

Lampson, M.A., and I.M. Cheeseman. 2011. Sensing centromere tension: Aurora B and the regulation of kinetochore function. *Trends Cell Biol*. 21:133-140.

Lampson, M.A., K. Renduchitala, A. Khodjakov, and T.M. Kapoor. 2004. Correcting improper chromosome-spindle attachments during cell division. *Nat Cell Biol*. 6:232-237.

Lawrimore, J., K.S. Bloom, and E.D. Salmon. 2011. Point centromeres contain more than a single centromere-specific Cse4 (CENP-A) nucleosome. *J Cell Biol*. 195:573-582.

Leśniewska, K., E. Warbrick, and H. Ohkura. 2014. Peptide aptamers define distinct EB1- and EB3-binding motifs and interfere with microtubule dynamics. *Molecular Biology of the Cell*. 25:1025-1036.

Levesque, A.A., and D.A. Compton. 2001. The chromokinesin Kid is necessary for chromosome arm orientation and oscillation, but not congression, on mitotic spindles. *J Cell Biol*. 154:1135-1146.

Li, S., Z. Deng, J. Fu, C. Xu, G. Xin, Z. Wu, J. Luo, G. Wang, S. Zhang, B. Zhang, F. Zou, Q. Jiang, and C. Zhang. 2015. Spatial compartmentalization specializes function of Aurora-A and Aurora-B. *J Biol Chem*.

Li, X., and R.B. Nicklas. 1995. Mitotic forces control a cell-cycle checkpoint. *Nature*. 373:630-632.

Lioutas, A., and I. Vernos. 2013. Aurora A kinase and its substrate TACC3 are required for central spindle assembly. *EMBO Rep*. 14:829-836.

Liu, D., G. Vader, M.J. Vromans, M.A. Lampson, and S.M. Lens. 2009. Sensing chromosome bi-orientation by spatial separation of aurora B kinase from kinetochore substrates. *Science*. 323:1350-1353.

Liu, J.-J. 2017. Regulation of dynein-dynactin-driven vesicular transport. *Traffic*. 18:336-347.

Lupas, A., M. Van Dyke, and J. Stock. 1991. Predicting coiled coils from protein sequences. *Science*. 252:1162-1164.

Maiato, H., P.J. Hergert, S. Moutinho-Pereira, Y. Dong, K.J. Vandenbeldt, C.L. Rieder, and B.F. McEwen. 2006. The ultrastructure of the kinetochore and kinetochore fiber in Drosophila somatic cells. *Chromosoma*. 115:469-480.

Mallik, R., B.C. Carter, S.A. Lex, S.J. King, and S.P. Gross. 2004. Cytoplasmic dynein functions as a gear in response to load. *Nature*. 427:649-652.

Manatschal, C., A.M. Farcas, M.S. Degen, M. Bayer, A. Kumar, C. Landgraf, R. Volkmer, Y. Barral, and M.O. Steinmetz. 2016. Molecular basis of Kar9-Bim1 complex function during mating and spindle positioning. *Mol Biol Cell*.

Manfredi, M.G., J.A. Ecsedy, K.A. Meetze, S.K. Balani, O. Burenkova, W. Chen, K.M. Galvin, K.M. Hoar, J.J. Huck, P.J. LeRoy, E.T. Ray, T.B. Sells, B. Stringer, S.G. Stroud, T.J. Vos, G.S. Weatherhead, D.R. Wysong, M. Zhang, J.B. Bolen, and C.F. Claiborne. 2007. Antitumor activity of MLN8054, an orally active small-molecule inhibitor of Aurora A kinase. *Proc Natl Acad Sci U S A*. 104:4106-4111.

Mann, B.J., S.K. Balchand, and P. Wadsworth. 2017. Regulation of Kif15 localization and motility by the C-terminus of TPX2 and microtubule dynamics. *Mol Biol Cell*. 28:65-75.

Maresca, T.J., and E.D. Salmon. 2009. Intrakinetochore stretch is associated with changes in kinetochore phosphorylation and spindle assembly checkpoint activity. *J Cell Biol*. 184:373-381.

Maresca, T.J., and E.D. Salmon. 2010. Welcome to a new kind of tension: translating kinetochore mechanics into a wait-anaphase signal. *J Cell Sci*. 123:825-835.

Marshall, W.F., J.F. Marko, D.A. Agard, and J.W. Sedat. 2001. Chromosome elasticity and mitotic polar ejection force measured in living Drosophila embryos by four-dimensional microscopy-based motion analysis. *Curr Biol*. 11:569-578.

Matos, I., A.J. Pereira, M. Lince-Faria, L.A. Cameron, E.D. Salmon, and H. Maiato. 2009. Synchronizing chromosome segregation by flux-dependent force equalization at kinetochores. *J Cell Biol*. 186:11-26.

Matsuo, Y., S.P. Maurer, M. Yukawa, S. Zakian, M.R. Singleton, T. Surrey, and T. Toda. 2016. An unconventional interaction between Dis1/TOG and Mal3/EB1 in fission yeast promotes the fidelity of chromosome segregation. *J Cell Sci*. 129:4592-4606.

Matthies, H.J., R.J. Baskin, and R.S. Hawley. 2001. Orphan kinesin NOD lacks motile properties but does possess a microtubule-stimulated ATPase activity. *Mol Biol Cell*. 12:4000-4012.

Maurer, Sebastian P., Franck J. Fourniol, G. Bohner, Carolyn A. Moores, and T. Surrey. 2012. EBs Recognize a Nucleotide-Dependent Structural Cap at Growing Microtubule Ends. *Cell*. 149:371-382.

McIntosh, J.R., E.L. Grishchuk, M.K. Morphew, A.K. Efremov, K. Zhudenkov, V.A. Volkov, I.M. Cheeseman, A. Desai, D.N. Mastronarde, and F.I. Ataullakhanov. 2008. Fibrils connect microtubule tips with kinetochores: a mechanism to couple tubulin dynamics to chromosome motion. *Cell*. 135:322-333.

McIntosh, J.R., V. Volkov, F.I. Ataullakhanov, and E.L. Grishchuk. 2010. Tubulin depolymerization may be an ancient biological motor. *J Cell Sci*. 123:3425-3434.

Meijering, E., O. Dzyubachyk, and I. Smal. 2012. Methods for cell and particle tracking. *Methods Enzymol*. 504:183-200.

Milks, K.J., B. Moree, and A.F. Straight. 2009. Dissection of CENP-C-directed centromere and kinetochore assembly. *Mol Biol Cell*. 20:4246-4255.

Miller, S.A., M.L. Johnson, and P.T. Stukenberg. 2008. Kinetochore attachments require an interaction between unstructured tails on microtubules and Ndc80(Hec1). *Curr Biol*. 18:1785-1791.

Minestrini, G., A.S. Harley, and D.M. Glover. 2003. Localization of Pavarotti-KLP in living Drosophila embryos suggests roles in reorganizing the cortical cytoskeleton during the mitotic cycle. *Mol Biol Cell*. 14:4028-4038.

Mishima, M. 2016. Centralspindlin in Rappaport's cleavage signaling. *Semin Cell Dev Biol*. 53:45-56.

Moutinho-Pereira, S., N. Stuurman, O. Afonso, M. Hornsveld, P. Aguiar, G. Goshima, R.D. Vale, and H. Maiato. 2013. Genes involved in centrosome-independent mitotic spindle assembly in Drosophila S2 cells. *Proc Natl Acad Sci U S A*. 110:19808-19813.

Murthy, K., and P. Wadsworth. 2008. Dual role for microtubules in regulating cortical contractility during cytokinesis. *J Cell Sci*. 121:2350-2359.

Nguyen, P.A., A.C. Groen, M. Loose, K. Ishihara, M. Wuhr, C.M. Field, and T.J. Mitchison. 2014. Spatial organization of cytokinesis signaling reconstituted in a cell-free system. *Science*. 346:244-247.

Nicklas, R.B. 1965. CHROMOSOME VELOCITY DURING MITOSIS AS A FUNCTION OF CHROMOSOME SIZE AND POSITION. *J Cell Biol*. 25:SUPPL:119-135.

Nicklas, R.B. 1983. Measurements of the force produced by the mitotic spindle in anaphase. *J Cell Biol*. 97:542-548.

Nicklas, R.B. 1988. The forces that move chromosomes in mitosis. *Annu Rev Biophys Biophys Chem*. 17:431-449.

Nicklas, R.B., and C.A. Koch. 1969. Chromosome micromanipulation. 3. Spindle fiber tension and the reorientation of mal-oriented chromosomes. *J Cell Biol*. 43:40-50.

Nunes Bastos, R., S.R. Gandhi, R.D. Baron, U. Gruneberg, E.A. Nigg, and F.A. Barr. 2013. Aurora B suppresses microtubule dynamics and limits central spindle size by locally activating KIF4A. *J Cell Biol*. 202:605-621.

Odell, G.M., and V.E. Foe. 2008. An agent-based model contrasts opposite effects of dynamic and stable microtubules on cleavage furrow positioning. *J Cell Biol*. 183:471-483.

Petrovic, A., J. Keller, Y. Liu, K. Overlack, J. John, Y.N. Dimitrova, S. Jenni, S. van Gerwen, P. Stege, S. Wohlgemuth, P. Rombaut, F. Herzog, S.C. Harrison, I.R. Vetter, and A. Musacchio. Structure of the MIS12 Complex and Molecular Basis of Its Interaction with CENP-C at Human Kinetochores. *Cell*. 167:1028-1040.e1015.

Pollard, J.R., and M. Mortimore. 2009. Discovery and development of aurora kinase inhibitors as anticancer agents. *J Med Chem*. 52:2629-2651.

Przewloka, M.R., Z. Venkei, V.M. Bolanos-Garcia, J. Debski, M. Dadlez, and D.M. Glover. 2011a. CENP-C is a structural platform for kinetochore assembly. *Curr Biol*. 21:399-405.

Przewloka, M.R., V. Zsolt, V.M. Bolanos-Garcia, J. Debski, M. Dadlez, and D.M. Glover. 2011b. CENP-C is a structural platform for kinetochore assembly. *Current Biology*.

Putkey, F.R., T. Cramer, M.K. Morphew, A.D. Silk, R.S. Johnson, J.R. McIntosh, and D.W. Cleveland. 2002. Unstable kinetochore-microtubule capture and chromosomal instability following deletion of CENP-E. *Dev Cell*. 3:351-365.

Rago, F., and I.M. Cheeseman. 2013. Review series: The functions and consequences of force at kinetochores. *J Cell Biol*. 200:557-565.

Rappaport, R. 1961. Experiments concerning the cleavage stimulus in sand dollar eggs. *J Exp Zool*. 148:81-89.

Rappaport, R. 1971. Cytokinesis in animal cells. *Int Rev Cytol*. 31:169-213.

Reboutier, D., M.B. Troadec, J.Y. Cremet, L. Chauvin, V. Guen, P. Salaun, and C. Prigent. 2013. Aurora A is involved in central spindle assembly through phosphorylation of Ser 19 in P150Glued. *J Cell Biol*. 201:65-79.

Rieder, C.L., E.A. Davison, L.C. Jensen, L. Cassimeris, and E.D. Salmon. 1986. Oscillatory movements of monooriented chromosomes and their position relative to the spindle pole result from the ejection properties of the aster and half-spindle. *J Cell Biol*. 103:581-591.

Rieder, C.L., and E.D. Salmon. 1994. Motile kinetochores and polar ejection forces dictate chromosome position on the vertebrate mitotic spindle. *J Cell Biol*. 124:223-233.

Rodrigues, N.T., S. Lekomtsev, S. Jananji, J. Kriston-Vizi, G.R. Hickson, and B. Baum. 2015. Kinetochore-localized PP1-Sds22 couples chromosome segregation to polar relaxation. *Nature*. 524:489-492.

Sampath, S.C., R. Ohi, O. Leismann, A. Salic, A. Pozniakovski, and H. Funabiki. 2004. The chromosomal passenger complex is required for chromatin-induced microtubule stabilization and spindle assembly. *Cell*. 118:187-202.

Sarangapani, K.K., B. Akiyoshi, N.M. Duggan, S. Biggins, and C.L. Asbury. 2013. Phosphoregulation promotes release of kinetochores from dynamic microtubules via multiple mechanisms. *Proc Natl Acad Sci U S A*. 110:7282-7287.

Schaar, B.T., G.K. Chan, P. Maddox, E.D. Salmon, and T.J. Yen. 1997. CENP-E function at kinetochores is essential for chromosome alignment. *J Cell Biol*. 139:1373-1382.

Schittenhelm, R.B., F. Althoff, S. Heidmann, and C.F. Lehner. 2010. Detrimental incorporation of excess Cenp-A/Cid and Cenp-C into Drosophila centromeres is prevented by limiting amounts of the bridging factor Cal1. *J Cell Sci*. 123:3768-3779.

Schneider, C.A., W.S. Rasband, and K.W. Eliceiri. 2012. NIH Image to ImageJ: 25 years of image analysis. *Nat Methods*. 9:671-675.

Schuyler, S.C., and D. Pellman. 2001. Microtubule "plus-end-tracking proteins": The end is just the beginning. *Cell*. 105:421-424.

Screpanti, E., A. De Antoni, G.M. Alushin, A. Petrovic, T. Melis, E. Nogales, and A. Musacchio. 2011. Direct binding of Cenp-C to the Mis12 complex joins the inner and outer kinetochore. *Current Biology*.

Scrofani, J., T. Sardon, S. Meunier, and I. Vernos. 2015. Microtubule nucleation in mitosis by a RanGTP-dependent protein complex. *Curr Biol*. 25:131-140.

Shah, J.V., E. Botvinick, Z. Bonday, F. Furnari, M. Berns, and D.W. Cleveland. 2004. Dynamics of centromere and kinetochore proteins; implications for checkpoint signaling and silencing. *Curr Biol*. 14:942-952.

Shiroguchi, K., M. Ohsugi, M. Edamatsu, T. Yamamoto, and Y.Y. Toyoshima. 2003. The second microtubule-binding site of monomeric kid enhances the microtubule affinity. *J Biol Chem*. 278:22460-22465.

Smurnyy, Y., A.V. Toms, G.R. Hickson, M.J. Eck, and U.S. Eggert. 2010. Binucleine 2, an isoform-specific inhibitor of Drosophila Aurora B kinase, provides insights into the mechanism of cytokinesis. *ACS Chem Biol*. 5:1015-1020.

Steinmetz, M.O., and A. Akhmanova. 2008. Capturing protein tails by CAP-Gly domains. *Trends Biochem Sci*. 33:535-545.

Stenoien, D.L., S. Sen, M.A. Mancini, and B.R. Brinkley. 2003. Dynamic association of a tumor amplified kinase, Aurora-A, with the centrosome and mitotic spindle. *Cell Motil Cytoskeleton*. 55:134-146.

Stumpff, J., M. Wagenbach, A. Franck, C.L. Asbury, and L. Wordeman. 2012. Kif18A and chromokinesins confine centromere movements via microtubule growth suppression and spatial control of kinetochore tension. *Dev Cell*. 22:1017-1029.

Suzuki, A., B.L. Badger, J. Haase, T. Ohashi, H.P. Erickson, E.D. Salmon, and K. Bloom. 2016. How the kinetochore couples microtubule force and centromere stretch to move chromosomes. *Nat Cell Biol*. 18:382-392.

Suzuki, A., B.L. Badger, X. Wan, J.G. DeLuca, and E.D. Salmon. 2014. The architecture of CCAN proteins creates a structural integrity to resist spindle forces and achieve proper Intrakinetochore stretch. *Dev Cell*. 30:717-730.

Takagi, J., T. Itabashi, K. Suzuki, and S. Ishiwata. 2013. Chromosome position at the spindle equator is regulated by chromokinesin and a bipolar microtubule array. *Sci Rep*. 3:2808.

Tan, L., and T.M. Kapoor. 2011. Examining the dynamics of chromosomal passenger complex (CPC)-dependent phosphorylation during cell division. *Proc Natl Acad Sci U S A*. 108:16675-16680.

Tanaka, K., E. Kitamura, Y. Kitamura, and T.U. Tanaka. 2007. Molecular mechanisms of microtubule-dependent kinetochore transport toward spindle poles. *J Cell Biol*. 178:269-281.

Tanaka, T.U., N. Rachidi, C. Janke, G. Pereira, M. Galova, E. Schiebel, M.J. Stark, and K. Nasmyth. 2002. Evidence that the Ipl1-Sli15 (Aurora kinase-INCENP) complex promotes chromosome bi-orientation by altering kinetochore-spindle pole connections. *Cell*. 108:317-329.

Terada, Y. 2001. Role of chromosomal passenger complex in chromosome segregation and cytokinesis. *Cell Struct Funct*. 26:653-657.

Theurkauf, W.E., and R.S. Hawley. 1992. Meiotic spindle assembly in Drosophila females: behavior of nonexchange chromosomes and the effects of mutations in the nod kinesin-like protein. *J Cell Biol*. 116:1167-1180.

Thompson, S.L., and D.A. Compton. 2011. Chromosome missegregation in human cells arises through specific types of kinetochore-microtubule attachment errors. *Proc Natl Acad Sci U S A*. 108:17974-17978.

Toba, S., T.M. Watanabe, L. Yamaguchi-Okimoto, Y.Y. Toyoshima, and H. Higuchi. 2006. Overlapping hand-over-hand mechanism of single molecular motility of cytoplasmic dynein. *Proc Natl Acad Sci U S A*. 103:5741-5745.

Tokai-Nishizumi, N., M. Ohsugi, E. Suzuki, and T. Yamamoto. 2005. The chromokinesin Kid is required for maintenance of proper metaphase spindle size. *Mol Biol Cell*. 16:5455-5463.

Tomishige, M., D.R. Klopfenstein, and R.D. Vale. 2002. Conversion of Unc104/KIF1A kinesin into a processive motor after dimerization. *Science*. 297:2263-2267.

Tsai, M.Y., C. Wiese, K. Cao, O. Martin, P. Donovan, J. Ruderman, C. Prigent, and Y. Zheng. 2003. A Ran signalling pathway mediated by the mitotic kinase Aurora A in spindle assembly. *Nat Cell Biol*. 5:242-248.

Tseng, B.S., L. Tan, T.M. Kapoor, and H. Funabiki. 2010. Dual detection of chromosomes and microtubules by the chromosomal passenger complex drives spindle assembly. *Dev Cell*. 18:903-912.

Uchida, K.S., K. Takagaki, K. Kumada, Y. Hirayama, T. Noda, and T. Hirota. 2009. Kinetochore stretching inactivates the spindle assembly checkpoint. *J Cell Biol*. 184:383-390.

Vale, R.D., and L.S.B. Goldstein. One motor, many tails: An expanding repertoire of force-generating enzymes. *Cell*. 60:883-885.

Vale, R.D., and R.A. Milligan. 2000. The way things move: looking under the hood of molecular motor proteins. *Science*. 288:88-95.

Vale, R.D., J.A. Spudich, and E.R. Griffis. 2009. Dynamics of myosin, microtubules, and Kinesin-6 at the cortex during cytokinesis in Drosophila S2 cells. *J Cell Biol*. 186:727-738.

VandenBeldt, K.J., R.M. Barnard, P.J. Hergert, X. Meng, H. Maiato, and B.F. McEwen. 2006. Kinetochores use a novel mechanism for coordinating the dynamics of individual microtubules. *Curr Biol*. 16:1217-1223.

Violin, J.D., J. Zhang, R.Y. Tsien, and A.C. Newton. 2003. A genetically encoded fluorescent reporter reveals oscillatory phosphorylation by protein kinase C. *J Cell Biol*. 161:899-909.

Volkov, V.A., A.V. Zaytsev, N. Gudimchuk, P.M. Grissom, A.L. Gintsburg, F.I. Ataullakhanov, J.R. McIntosh, and E.L. Grishchuk. 2013. Long tethers provide high-force coupling of the Dam1 ring to shortening microtubules. *Proc Natl Acad Sci U S A*. 110:7708-7713.

Wan, X., R.P. O'Quinn, H.L. Pierce, A.P. Joglekar, W.E. Gall, J.G. DeLuca, C.W. Carroll, S.T. Liu, T.J. Yen, B.F. McEwen, P.T. Stukenberg, A. Desai, and E.D. Salmon. 2009. Protein architecture of the human kinetochore microtubule attachment site. *Cell*. 137:672-684.

Wandke, C., M. Barisic, R. Sigl, V. Rauch, F. Wolf, A.C. Amaro, C.H. Tan, A.J. Pereira, U. Kutay, H. Maiato, P. Meraldi, and S. Geley. 2012. Human chromokinesins promote chromosome congression and spindle microtubule dynamics during mitosis. *J Cell Biol*. 198:847-863.

Wang, Q., A.H. Crevenna, I. Kunze, and N. Mizuno. 2014. Structural basis for the extended CAP-Gly domains of p150(glued) binding to microtubules and the implication for tubulin dynamics. *Proc Natl Acad Sci U S A*. 111:11347-11352.

Wei, R.R., J. Al-Bassam, and S.C. Harrison. 2007. The Ndc80/HEC1 complex is a contact point for kinetochore-microtubule attachment. *Nat Struct Mol Biol*. 14:54-59.

Weisbrich, A., S. Honnappa, R. Jaussi, O. Okhrimenko, D. Frey, I. Jelesarov, A. Akhmanova, and M.O. Steinmetz. 2007. Structure-function relationship of CAP-Gly domains. *Nat Struct Mol Biol*. 14:959-967.

Welburn, J.P., M. Vleugel, D. Liu, J.R. Yates, 3rd, M.A. Lampson, T. Fukagawa, and I.M. Cheeseman. 2010. Aurora B phosphorylates spatially distinct targets to differentially regulate the kinetochore-microtubule interface. *Mol Cell*. 38:383-392.

Welburn, J.P.I. 2013. The molecular basis for kinesin functional specificity during mitosis. *Cytoskeleton*. 70:476-493.

Wollman, R., E.N. Cytrynbaum, J.T. Jones, T. Meyer, J.M. Scholey, and A. Mogilner. 2005. Efficient chromosome capture requires a bias in the 'search-and-capture' process during mitotic-spindle assembly. *Curr Biol*. 15:828-832.

Wood, K.W., L. Lad, L. Luo, X. Qian, S.D. Knight, N. Nevins, K. Brejc, D. Sutton, A.G. Gilmartin, P.R. Chua, R. Desai, S.P. Schauer, D.E. McNulty, R.S. Annan, L.D. Belmont, C. Garcia, Y. Lee, M.A. Diamond, L.F. Faucette, M. Giardiniere, S. Zhang, C.M. Sun, J.D. Vidal, S. Lichtsteiner, W.D. Cornwell, J.D. Greshock, R.F. Wooster, J.T. Finer, R.A. Copeland, P.S. Huang, D.J. Morgans, Jr., D. Dhanak, G. Bergnes, R. Sakowicz, and J.R. Jackson. 2010. Antitumor activity of an allosteric inhibitor of centromere-associated protein-E. *Proc Natl Acad Sci U S A*. 107:5839-5844.

Wood, K.W., R. Sakowicz, L.S. Goldstein, and D.W. Cleveland. 1997. CENP-E is a plus end-directed kinetochore motor required for metaphase chromosome alignment. *Cell*. 91:357-366.

Yajima, J., M. Edamatsu, J. Watai-Nishii, N. Tokai-Nishizumi, T. Yamamoto, and Y.Y. Toyoshima. 2003. The human chromokinesin Kid is a plus end-directed microtubule-based motor. *EMBO J*. 22:1067-1074.

Yang, C.H., J. Tomkiel, H. Saitoh, D.H. Johnson, and W.C. Earnshaw. 1996. Identification of overlapping DNA-binding and centromere-targeting domains in the human kinetochore protein CENP-C. *Mol Cell Biol*. 16:3576-3586.

Yang, Z., U.S. Tulu, P. Wadsworth, and C.L. Rieder. 2007. Kinetochore dynein is required for chromosome motion and congression independent of the spindle checkpoint. *Curr Biol*. 17:973-980.

Yardimci, H., M. van Duffelen, Y. Mao, S.S. Rosenfeld, and P.R. Selvin. 2008. The mitotic kinesin CENP-E is a processive transport motor. *Proc Natl Acad Sci U S A*. 105:6016-6021.

Ye, A.A., S. Cane, and T.J. Maresca. 2016a. Chromosome biorientation produces hundreds of piconewtons at a metazoan kinetochore. *Nat Commun*. 7:13221.

Ye, A.A., J. Deretic, C.M. Hoel, A.W. Hinman, D. Cimini, J.P. Welburn, and T.J. Maresca. 2015. Aurora A Kinase Contributes to a Pole-Based Error Correction Pathway. *Curr Biol*. 25:1842-1851.

Ye, A.A., J. Torabi, and T.J. Maresca. 2016b. Aurora A Kinase Amplifies a Midzone Phosphorylation Gradient to Promote High-Fidelity Cytokinesis. *Biol Bull*. 231:61-72.

Yucel, J.K., J.D. Marszalek, J.R. McIntosh, L.S. Goldstein, D.W. Cleveland, and A.V. Philp. 2000. CENP-meta, an essential kinetochore kinesin required for the maintenance of metaphase chromosome alignment in Drosophila. *J Cell Biol*. 150:1-11.

Yusko, E.C., and C.L. Asbury. 2014. Force is a signal that cells cannot ignore. *Mol Biol Cell*. 25:3717-3725.

Zhang, P., and R.S. Hawley. 1990. The genetic analysis of distributive segregation in Drosophila melanogaster. II. Further genetic analysis of the nod locus. *Genetics*. 125:115-127.

Zhang, P., B.A. Knowles, L.S. Goldstein, and R.S. Hawley. 1990. A kinesin-like protein required for distributive chromosome segregation in Drosophila. *Cell*. 62:1053-1062.

Zhu, C., J. Zhao, M. Bibikova, J.D. Leverson, E. Bossy-Wetzel, J.B. Fan, R.T. Abraham, and W. Jiang. 2005. Functional analysis of human microtubule-based motor proteins, the kinesins and dyneins, in mitosis/cytokinesis using RNA interference. *Mol Biol Cell*. 16:3187-3199.